Master thesis and internship[BR]- Master's thesis : The Impacts of Aspect Ratio Variations in Preliminary Design of a Mid-Range Jet Transport Aircraft[BR]- Internship

Auteur : Müller, Florian
Promoteur(s) : Dimitriadis, Grigorios
Faculté : Faculté des Sciences appliquées
Diplôme : Master en ingénieur civil en aérospatiale, à finalité spécialisée en "aerospace engineering"
Année académique : 2023-2024
URI/URL : http://hdl.handle.net/2268.2/20407

The Impacts of Aspect Ratio Variations in Preliminary Design of a Mid-Range Jet Transport Aircraft

Master's Thesis conducted for obtaining the Master's degree of Science in Aerospace Engineering

Academic supervisor:
Grigorios DIMITRIADIS

Company supervisor:
Markus RITTER

Author:
Florian MÜLLER

Jury:
Thomas ANDRIANNE
Ludovic NOELS

University of Liège
Faculty of Applied Sciences
Academic year 2023 - 2024

Abstract

Reducing drag is an essential challenge in aeronautics. The lower the drag, the better the fuel efficiency of the aircraft. Indeed, the thrust generated by the engines is the force that balance the drag and can be reduced by reducing the drag. The aircraft drag comes from the fuselage, wing, tail and engine, however, the largest part of the drag comes from the wing. The total drag of the wing is the sum of the profile drag, composed on frictional and pressure drag, and the induced drag. The frictional drag is related to the surface area exposed to the flow and the pressure drag is related to the cross sectional area of the body. The induced drag is the 3 dimensional drag due to vortices at the wing tip. This last represents a large part of the total wing drag and can be reduced in two different ways: increase the Oswald factor, which means get as close as possible to an elliptical lift distribution, or increase the wing aspect ratio (AR), which is the ratio between the square of the span and the wing surface.

In this work, the second option is chosen and the studied aircraft is a mid-range jet transport aircraft concept developed by the German Aerospace Center DLR which has a baseline aspect ratio of 15.6. Three methods of aspect ratio increase are developed and the results obtained by each method are analysed and compared. cpacs-MONA, the computational framework developed by DLR, is used to generate the structural and aerodynamic finite element models thanks to ModGen and evaluate the aerodynamic, structural and aeroelastic characteristics of the aircraft thanks to MSC Nastran. Some methods to check the reliability of the results are used and a method based on Fourier series is implemented to compute the Oswald factor e and evaluate the more accurately the induced drag. One of the results of this AR investigation is that for an AR that increases from 15.6 to 16.8, the induced drag decrease from 5 to 10 %, depending on the chosen method.

Resumé

La réduction de la traînée est un défi essentiel en aéronautique. Plus la traînée est faible, moins l'avion consommera de carburant. En effet, la poussée générée par les moteurs est la force qui équilibre la traînée et peut être réduite en réduisant la traînée. La traînée de l'avion provient du fuselage, de l'aile, de l'empenage et du moteur, mais la plus grande partie de la traînée provient de l'aile. La traînée totale de l'aile est la somme de la traînée de profil, composée de la traînée de friction et de pression, et de la traînée induite. La traînée de friction est liée à la surface exposée à l'écoulement et la traînée de pression est liée à la section transversale de l'aile, c'est à dire le profile de l'aile. La traînée induite est la traînée 3D due aux tourbillons au bout de l'aile. Cette dernière représente une grande partie de la traînée totale et peut être réduite de deux manières différentes : en augmentant le facteur de Oswald, ce qui signifie se rapprocher le plus possible d'une distribution de portance elliptique, ou en augmentant l'allongement d'aile (aspect ratio ou AR), qui est le rapport entre le carré de la l'envergure de l'aile et sa surface.

Dans ce travail, la deuxième option est choisie et l'avion étudié est un concept d'avion de transport à réaction de moyenne portée développé par le Centre Aérospatial Allemand DLR qui a un AR de 15,6. Trois méthodes d'augmentation du AR sont développées et comparées. L'outil de calcul de structure aéroélastique, cpacs-MONA, développé par DLR, est utilisé pour générer les modèles éléments finis structurels et aérodynamiques grâce à ModGen et évaluer les caractéristiques aérodynamiques, structurelles et aéroélastiques de l'avion grâce à MSC Nastran. Certaines méthodes pour vérifier la fiabilité des résultats sont utilisées et une méthode basée sur les séries de Fourier est implémentée pour calculer le facteur d'Oswald e et évaluer plus précisément la traînée induite. Un des résultats de cette enquête sur l'AR est que pour un AR qui augmente de 15,6 à 16,8, la traînée induite diminue de 5 à 10 %, selon la méthode choisie.

Acknowledgements

First of all, I would like to thank my supervisor, Markus Ritter, who let me the opportunity to work on an important project and who welcomed me at the DLR. I thank him for his involvement in my work, his valuable advice as well as for the time he invested on it.

In a broader sense, I am grateful for the whole DLR team and especially for Matthias Schulze, Vega Handojo and Markus Zimmer who helped me during my internship. Indeed, they were able to answer my questions during these past months and also challenge my work.

I would also like to thank Professor Dimitriadis for his availability and advice throughout this work. His suggestions are very interesting and appreciable.

Finally, I would like to thank my family, my friends and my girlfriend for their support and help during this project and throughout my five years at the University of Liège. This allows me to be the person I am today.

Contents

List of Figures

List of Tables

Glossary

List of Acronyms

Acronyms	Description
AC	Aerodynamic center
AOA	Angle of attack
CG	Center of gravity
DLM	Doublet-lattice method
FEM	Finite element model
GLA	Gust load alleviation
HTP	Horizontal tail plane
MAC	Mean aerodynamic chord
MDO	Multidisciplinary design optimisation
MLA	Maneuver load alleviation
PSD	Power spectral density
RMS	Root mean square
UP	Ultra performance
VLM	Vortex-lattice method
VTP	Vertical tail plane

List of Mass Cases and Design Speeds

Acronyms	Description
MFOeF	Notation for the maximum fuel mass case (no payload and maximum fuel)
MOOee	Notation for the empty mass case (no payload, no fuel)
MTOAa	Notation for the maximum take-off weight case (maximum payload, 56 % fuel)
MZOAe	Notation for the zero fuel mass case (maximum payload, no fuel)
MC	Design cruise Mach number
MMO	Design maximum operational Mach number
VA	Design maneuver velocity
Va	Stall velocity for a load factor of 2.5
VB	Design gust velocity
VC	Design cruise velocity
VD	Design dive velocity

List of Symbols

Variable	Description	Unit
α	Angle of attack	$^\circ$
$\Delta\alpha_g$	Incremental gust angle of attack	-
β	Slip angle	$^\circ$
η_{CS}	Control surface deflection	$^\circ$
ε	Convergence criterion	-
Γ	Circulation	$\mathrm{m^2/s}$
γ	Transient decay rate coefficient	-
μ_g	Aircraft density parameter for gust	$\mathrm{1/m}$
ν	Poisson's ratio	-
ω	Eigenfrequency	$\mathrm{rad/s}$
ρ	Fluid or material density	$\mathrm{kg/m^3}$
ρ_0	Air density at sea level	$\mathrm{kg/m^3}$
σ_c	Compressive stress	GPa
σ_t	Tensile stress	GPa
τ	Shear stress	GPa
AR	Aspect ratio of the wing	-
B_{hh}	Modal damping matrix	$\mathrm{kg/s}$
$\bar{c}$	Mean aerodynamic chord (MAC) or reference length	m
$C_{D,i}$	Induced drag coefficient	-
C_{L_α}	Lift coefficient derivative	$\mathrm{1/rad}$
C_{L_W}	Wing lift coefficient	-
$C_{L,max}$	Maximum lift coefficient of the aircraft	-
$C_{L,min}$	Minimum lift coefficient of the aircraft	-
C_m	Pitching moment coefficient	-
c_p	Pressure coefficient	-
E	Young modulus	GPa
e	Oswald factor	-
G	Shear modulus	GPa
g	Gravity acceleration	$\mathrm{m/s^2}$
K_n	Stability margin	$\%$
K_g	Pratt gust alleviation factor	-
k	Reduced frequency	-
K_{aa}	Structural stiffness matrix	$\mathrm{kg/s^2}$
K_{hh}	Modal stiffness matrix	$\mathrm{kg/s^2}$
M_{aa}	Structural mass matrix	kg
M_{hh}	Modal mass matrix	kg
M_x	Bending moment	$\mathrm{N{\cdot}m}$
M_y	Torsional moment	$\mathrm{N{\cdot}m}$
n_g	Gust load factor	-
n_z	Load factor	-

p	Angular velocity in roll direction	rad/s
$\dot{p}$	Angular acceleration in roll direction	rad/s^2
p	Static pressure	Pa
p_∞	Free stream pressure	Pa
P_a	Applied loads vector	N
q	Angular velocity in pitch direction	rad/s
$\dot{q}$	Angular acceleration in pitch direction	rad/s^2
$\bar{q}$	Dynamic pressure	-
Q_{hh}	Aerodynamic matrix	-
Q_{hh}^I	Modal aerodynamic damping matrix	kg/s
Q_{hh}^R	Modal aerodynamic stiffness matrix	kg/s^2
r	Angular velocity in yaw direction	rad/s
$\dot{r}$	Angular acceleration in yaw direction	rad/s^2
S	Wing surface	m^2
s	Dimensionless time	-
t	Time	s
$\frac{U}{U_0}$	Gust intensity	-
u_a	Nodal displacement vector	m
$\bar{u}_h$	Modal amplitude vector	-
$\ddot{u}_a$	Nodal acceleration vector	m/s^2
V	Velocity	m/s
V_∞	Airspeed	m/s
W	Aircraft weight	N
$w_{g,EAS}$	Gust equivalent airspeed	m/s
x_{AC}	x coordinate of the aerodynamic center	m
x_{CG}	x coordinate of the center of gravity	m

Introduction

Background and Motivation

In the current era, pollution is one of the most important subjects in the world. One crucial challenge is the reduction of the fuel consumption in the transportation sector. The car industry has already achieved huge progresses in electrification while rail industry use electricity for decades, even centuries. The most meaningful way to travel very long distances in short time is the aircraft. In 2019, the global airline industry counted 38.9 million of flights [1] which represent 95 billion gallons (360 million cubic meters) of fuel and 920 million tons of CO_2 emissions [2]. Each kilogram of fuel saved allows to reduce CO_2 emissions by 3 kilograms [3]. It is very important for the Earth to reduce all these numbers, however, it is not that easy. In fact, aircraft industry is already extremely advanced in terms of technologies and the smallest gain in efficiency or performance requires a massive effort. There are multiple ways to reduce aircraft fuel consumption: lighter materials, more efficient engines, structural optimisation, higher aspect ratio. The last allows to reduce induced drag and thus total drag. By this drag reduction, thrust can be lower, and fuel consumption can decrease. This thesis will follow this last option, the wing aspect ratio increase.

State of the Art

At the beginning of the aviation, in 1900, the Wright brothers designed the wings of their first gliders based on aeronautical data reported by Lilienthal, the German aeronautical pioneer [4]. However, they found completely different results for the lift than the Lilienthal glider model. Their gliders had aspect ratios around 3.4 while the aspect ratio of the one studied by Lilienthal was 6.5. Thanks to tests carried out in wind tunnels, they were able to understand the importance that the aspect ratio had on the lift and drag. They concluded from their tests that increasing the aspect ratio made it possible to increase lift and reduce drag. They also discover that the shape of the airfoil was very important in the wing design because thin airfoil reduce drag in comparison with thick airfoil. However, the understanding of the airfoil thickness was incomplete. Thin airfoils lead to stall at much lower angles of attack than thick airfoils. Moreover, thin airfoils have a leading edge separation while thick airfoils have a trailing edge separation [5]. Thick airfoils also have structural and aerodynamic advantages. The first planes were made up of several wing because the engines were not very powerful and the speed was low, so the lift was reduced. Large aspect ratios and thick airfoils were prominent in efficient wing designs in the 1930s which contribute to the development of monoplane, i.e a single wing. Another turning point was in the 1950s, with the development of jet airplanes that were flying close to or beyond the speed of sound. These flying condition required thinner wings to reduce the effects of shock waves that increase drag and reduce lift. To reduce the supersonic wave drag, supercritical airfoils have been developed and swept wings have been used. Today, the wing and airfoil improvement is still on working in order to increase lift-to-drag ratio and reduce fuel consumption.

It is very important to optimise the aircraft wing shape, mass, characteristics in general in order to increase the fuel efficiency and increase the flight range. The multidisciplinary design optimisation (MDO) of aircraft wing is used more and more and gives very interesting results. The MDO consists to

solve a design problem by using optimisation methods in different disciplines. Benaouali and Kachel [6] developed together a fully automated MDO of the aircraft wing using commercial software integration for the geometric modeling, for the structural finite element modeling and sizing and for the aerodynamic meshing. Their studied case was an A320 class aircraft and the result was an 8.9% increase of the Breguet range - range of an aircraft as a function of its aerodynamic efficiency, propulsion efficiency, and fuel consumption - by considering shape and structural design variables. This range is defined by the following equation [7]:

$$R = \frac{V}{SFC} \frac{L}{D} \ln \left(\frac{W_i}{W_f} \right),$$

with V the true airspeed, SFC the specific fuel consumption, L and D the lift and drag of the aircraft, W_i and W_f the initial and final weights of the aircraft.

Another study regarding the aspect ratio variation of a wing including a nonlinear beam model has been conducted by Calderon et al. [8] in 2019. They compared linear and non linear results of the wing mass, lift-to-drag ratio and Breguet range for aspect ratio between 10 and 24 as shown in Figure 1. The method used for aspect ratio variation was to keep the sweep, surface area, taper and dihedral constant.
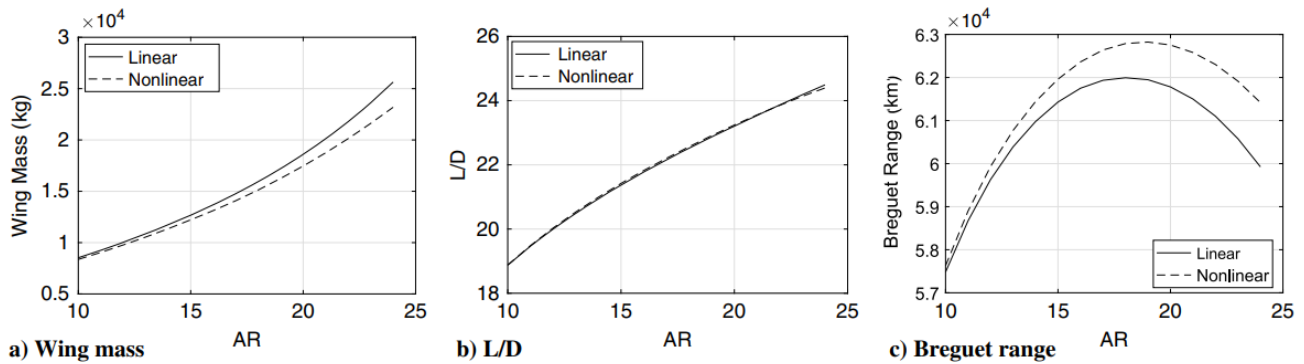
Figure 1: Representations of a) Wing mass, b) L/D, and c) Breguet Range for AR = 10:2:24 for the linear and nonlinear analysis [8].

They obtained pertinent results. The wing mass increases exponentially with the aspect ratio. They found an "optimal solution" regarding the Breguet range at an aspect ratio of 18 for the linear solution and 19 for the non-linear solution. This optimal solution is only valid for this study and depend on the studied aircraft and wing.

Objectives of the Thesis

The objective of this thesis is to determine the optimal aspect ratio of a medium range jet transport aircraft wing that maximises efficiency, and thus reduces the fuel consumption. This work is divided into four chapters.

The first chapter gives a general description of cpacs-MONA, the structural optimisation tool developed by DLR. This tool generates a finite element structural model of an aircraft with ModGen and simulates it with MSC Nastran. Also aeroelastic characteristics of the aircraft, such as flutter, as well as steady and unsteady loads can be computed with the finite element model. The generation of structural and aerodynamic models is discussed and the setup for the aeroelastic and optimisation models is developed. The whole cpacs-MONA iterative process is detailed step by step.

The second chapter describes the DLR-F25 baseline configuration, its key features, such as the mission description, wing planform, geometry and the engine capabilities. The mass and load cases as well as the design speeds used in the simulation process are defined. The aerodynamic and structural models used by Nastran for the maneuver loads, gust loads and flutter calculations are explained. MSC Nastran uses the optimisation model described in terms of design variables, responses and constraints. The DLR-F25 baseline configuration is simulated by cpacs-MONA and the aircraft characteristics, such as the lift distribution of the wing, the longitudinal stability and the elastic deformation of the wing are analysed. Steady and quasi-steady maneuver loads, gust loads and flutter are also computed.

The third chapter describes in detail the extensions of cpacs-MONA used for the aspect ratio investigation of the DLR-F25. This conceptual aircraft is designed by the German Aerospace Center (DLR) which is the Federal Republic of Germany's research centre for aeronautics and space. The modification of the aspect ratio - for most investigations it was increased - is implemented through three different methods. Some initial issues regarding the definition of the internal structure and the aerodynamic grid are solved. A numerical method, based on a Fourier series, to approximate the lift distribution and the Oswald factor has been developed. A lot of effort is put into automating the whole simulation process, from the geometry modification to the post processing.

The last chapter shows and describes the impact of the aspect ratio variation on the structural, aerodynamic and aeroelastic characteristics. The aspect ratio limits as well as the different approaches for gust loads computations are discussed. The results from quasi-steady Pratt gust and Nastran solution sequence SOL 146 for the computation of 1-cos gust loads are compared. The different results obtained for different mass cases and aspect ratio variation methods are discussed and interpreted in order to figure out which method and which aspect ratio gives the best results in term of induced drag reduction.

Chapter 1

The cpacs-MONA Framework for Preliminary Aircraft Design

In this chapter, the main tool - cpacs-MONA - used in this work will be presented and its features will be explained. ModGen will be used to generate the parametric model and MSC Nastran will be the maneuver loads, gust loads and flutter simulation tool. Finally, the structural optimisation loops will be detailed.

1.1 General Description

At first, in the aeronautical field, aeroelasticity can be defined as the study of the interaction of structural, inertial, and aerodynamic forces in the aircraft [9] and can be visually represented with the Collar's aeroelastic triangle shown in Figure 1.1.
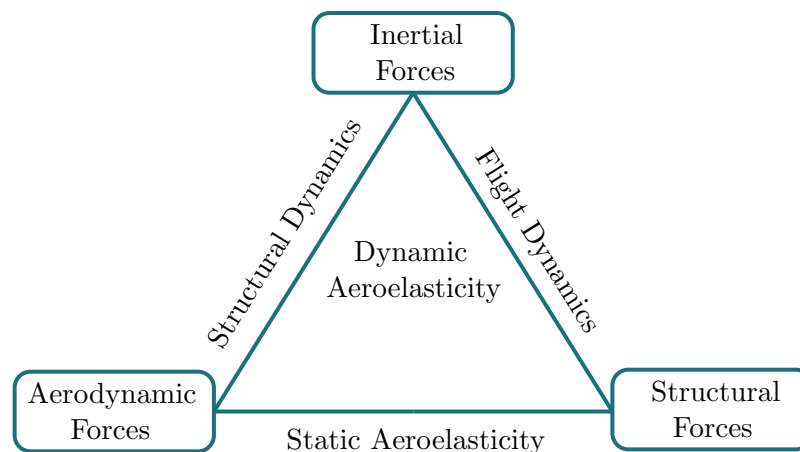
Figure 1.1: Collar's aeroelastic triangle

cpacs-MONA is a computational framework developed by the DLR Institute of Aeroelasticity that designs highly parameterised aeroelastic structures in order to evaluate the aeroelastic behaviour of different aircraft configurations [10]. This process is divided into three main steps as shown in Figure 1.2: the set-up of the parametric model, the loads analysis, and finally the structural optimisation.
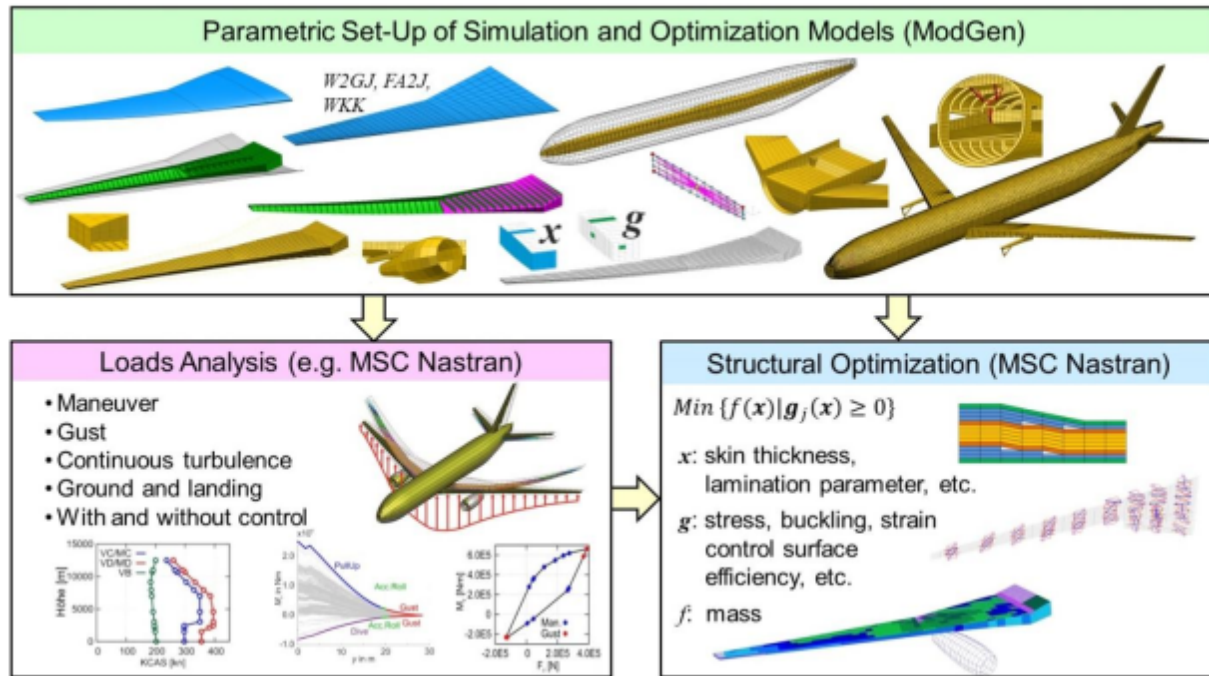
Figure 1.2: Visualisation of the three main steps of the MONA process [10].

The MONA process uses two main programs to carry out the simulations. The first one, ModGen is an acronym of Model Generator, is developed by the DLR Institute of Aeroelasticity as well. Its aim is to set-up the structural as well as the aerodynamic finite element models for the loads analysis and the structural optimisation. The second one is the well known MSC Nastran software used for the finite element analysis. It is able to simulate maneuver and gust loads which are very important in aircraft design. It can also compute flutter and structural optimisation. The structural optimisation is based on design variables, responses and constraints. The thickness of skins, spars and ribs are the design variables while the stress and strain are responses. The design function of the structural optimisation is the mass of the aircraft or the mass of individual components which are optimised, such as the wingbox or the horizontal and vertical tailplanes. The name MONA comes from the contraction of ModGen and Nastran and, cpacs stands for Common Parametric Aircraft Configuration Schema [11].

cpacs-MONA only uses a single xml file to run simulations. This file, called CPACS dataset, contains the description of the whole aircraft and its systems: from the outer geometry (wings, fuselage, engine) and internal structure (ribs, spars, stringers) to the flight conditions, mass cases, aircraft loads and aerodynamic data. This file contains a lot of information and will be modified to change the geometry of the wing as well as its internal structure. Aircraft components like wing, engine, fuselage are built separately with ModGen, finally, the individual components are assembled to the entire simulation model. Within Nastran, the static aeroelastic and structural optimisation analysis are also executed in parallel. The cpacs-MONA procedure is described in Figure 1.3. This iterative process requires convergence criteria which are the mass of the aircraft (or particular components) and loads at selected monitoring points.
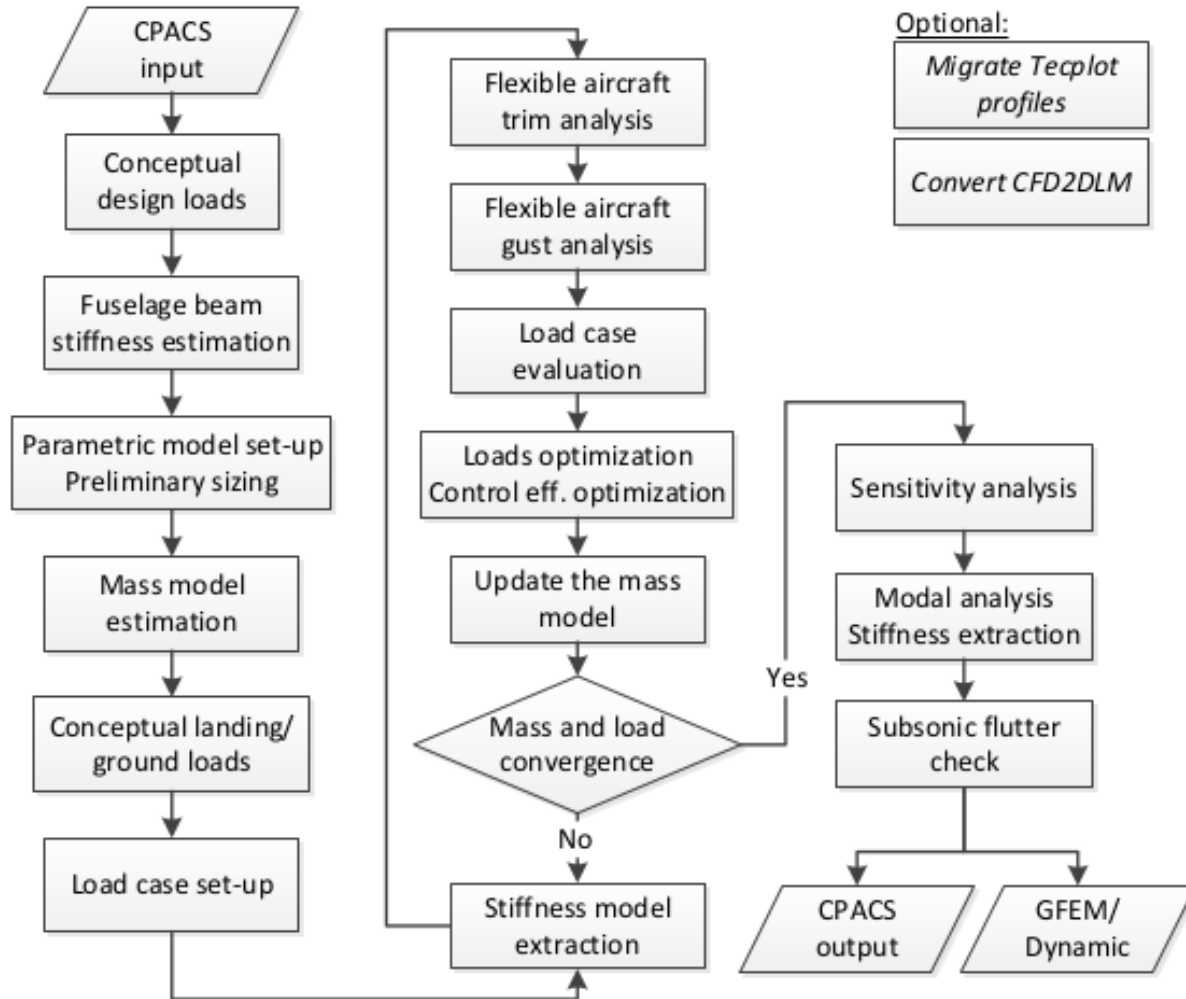
Figure 1.3: Process flow of cpacs-MONA [10].

1.2 Parametric Model Generation with ModGen

The parametric model set-up is created by ModGen, a Fortran77 program to generate finite element models (FEMs) to be used by MSC Nastran for aerodynamic, structural, and aeroelastic analysis of a complete aircraft. The FE-models generated by ModGen are close to the reality as show in Figure 1.4 which represents an example of the wing structure generated by ModGen. The shell elements as well as the bar elements are generated and allow to show the capabilities of ModGen.

SHELL-Elements
- skin
- spar webs
- ribs

BAR-Elements
- spar caps
- spar stiffener
- rib stiffener
- stringer
- pylon
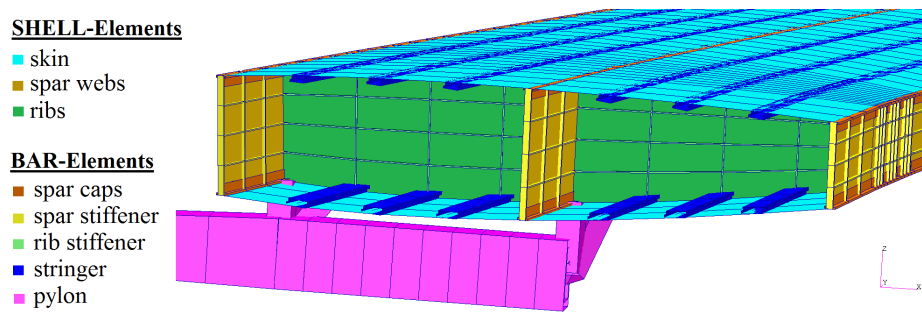
Figure 1.4: Example of a wing structure generated by ModGen [12].

ModGen is used to perform a preliminary dimensioning, also called the Preliminary Cross-section Sizing (PCS), of the wing-like structures (wing and tailplanes) by using the forces and moments applied to the aircraft structure. The PCS is used at two points of the cpacs-MONA process: in the first model setup steps with the initial loads and a second time with the loads generated by the trim analysis of the flexible aircraft. This second pre-sizing is used by MSC Nastran for the structural optimisation.

1.3 Setup of the MSC Nastran Aeroelastic and Optimisation Models

The MSC Nastran aeroelastic analysis is used to compute the aeroelastic flutter [13], defined as a dynamic instability of an elastic structure in a fluid flow that leads to self-excited structural oscillations. Flutter appears when the net damping - sum of the structural positive damping and aerodynamic negative damping - becomes negative. Flutter is a high velocity phenomenon because it appears when the structural damping is not able to balance anymore the aerodynamic damping which decreases with velocity.

Nastran is able to compute aeroelastic flutter by using three different methods: the K-method, KE-method and PK-method. For the K-method, artificial damping is injected into the system, in the form of structural damping term, to push it to the flutter point. The main disadvantage of this method is that the results are difficult to interpret [14]. The KE-method is a variant of the K-method with three differences: the viscous damping is ignored, the complex modes are not output and the flutter is sorted using extrapolation. It is computationally inexpensive but limited in input and output. The PK-method uses an iterative process and is performed by using doublet lattice aerodynamics. The imaginary part of the stiffness matrix is neglected which means that no modal damping is used.

For the cpacs-MONA process, the aeroelastic flutter is computed by MSC Nastran using the PK-method. This very popular method has been developed in the 80's and has become the industry standard to evaluate flutter [9]. The fundamental equation for the modal flutter analysis is:

$$\left[M_{hh} \cdot p^2 + \left(B_{hh} - \frac{1}{4}\rho \cdot \bar{c} \cdot V \cdot Q_{hh}^I/k \right) \cdot p + \left(K_{hh} - \frac{1}{2} \cdot \rho \cdot V^2 \cdot Q_{hh}^R \right) \right] \cdot \{\bar{u}_h\} = 0, \qquad (1.1)$$

with M_{hh} the modal mass matrix, usually diagonal, p the eigenvalue, B_{hh} the modal damping matrix, ρ the fluid density, $\bar{c}$ the reference length, V the velocity, Q_{hh}^I the modal aerodynamic damping matrix, k the reduced frequency, K_{hh} the modal stiffness matrix, Q_{hh}^R the modal aerodynamic stiffness matrix and $\bar{u}_h$ the modal amplitude vector. Q_{hh}^R and Q_{hh}^I are, respectively, the real and imaginary parts of the aerodynamic force matrix $Q_{hh}(M, k)$ that is a function of the Mach number and the reduced frequency.

The aerodynamic force matrix is computed by MSC Nastran with the Doublet-Lattice method (DLM). The DLM is a method to linearise the aerodynamic potential theory. The lifting surfaces are assumed to be parallel to the flow. That is a simplification of the reality where the bending deformation exists. This

method is an extension of the Vortex-Lattice method (VLM) applied to unsteady flow. The Equation 1.1 can be rewritten in the state-space form:

$$[A - p \cdot I] \cdot \{\bar{u}_h\},$$

where the real matrix A is expressed as follows:

$$A = \begin{bmatrix} 0 & I \\ -M_{hh}^{-1} \cdot \left[K_{hh} - \frac{1}{2} \cdot \rho \cdot \bar{c} \cdot V^2 \cdot Q_{hh}^R\right] & -M_{hh} \cdot p^{-1} \cdot \left[B_{hh} - \frac{1}{4} \cdot \rho \cdot \bar{c} \cdot V \cdot Q_{hh}^I/k\right] \end{bmatrix}, \qquad (1.2)$$

and $\bar{u}_h$ includes both modal displacements and velocities. The eigenvalues of matrix A are real or complex conjugate pairs, and the convergence/divergence depends on the real roots. The eigenvalue is written by:

$$p_{rs}^{(j)} = \omega_{rs}^{(j)} \cdot (\gamma_{rs}^{(j)} \pm i),$$

where ω is the eigenfrequency and γ is the transient decay rate coefficient. The structural damping coefficient $g = 2\gamma_{ss}^{(c)}$, with the exponent (c) for the converged value. The indices r and s are respectively the oscillatory mode number and the number of oscillatory modes. The exponent (j) is the iteration number. The next estimate of the reduced frequency is as follows:

$$k_s^{(j)} = \omega_{ss}^{(j)} \cdot \left(\frac{\bar{c}}{2 \cdot V}\right)$$

The first reduced frequency of the first oscillatory root is initiated as:

$$k_1^{(0)} = \omega_{11}^{(0)} \cdot \left(\frac{\bar{c}}{2 \cdot V}\right)$$

The convergence of the oscillatory root occurs when:

$$|k_1^{(j)} - k_1^{(j-1)}| \begin{cases} < \varepsilon & \text{for} \quad k_1^{(j-1)} < 1.0 \\ < \varepsilon \cdot k_1^{(j-1)} & \text{for} \quad k_1^{(j-1)} \geq 1.0 \end{cases},$$

The convergence criterion ε has a default value of 0.001. The iterative process continues until the convergence of every oscillatory root occurs:

$$|k_s^{(j)} - k_s^{(j-1)}| \begin{cases} < \varepsilon & \text{for} \quad k_s^{(j-1)} < 1.0 \\ < \varepsilon \cdot k_s^{(j-1)} & \text{for} \quad k_s^{(j-1)} \geq 1.0 \end{cases}$$

The main advantage of this flutter calculation method is that the results are directly produced for a given velocity while both other methods use an iterative process to determine the reduced frequency of flutter.

The structural dimensions of the wing-like components are estimated using 3 steps:

- At first, the structural properties, such as skin, spar and rib thickness are computed according to the cutting loads of the design load cases. The cross-section area of the stringer and spar caps are also computed with the cut loads. The pre-sizing method, called preliminary cross section sizing, is executed when the simulation models are set up. This pre-sizing allows to evaluate the loads and then, the pre-sizing is performed a second time with these new loads. It allows to have a better starting for the third iteration.

- Then, Nastran solution 200 [15] is used for the proper dimensioning of the structure that has to resist to the loads. This task is the structural optimisation based on mathematical optimisation and is expressed as follows:

$$Min f(x) | g(x) \leq 0; xl \leq x \leq xu,$$

with f the objective function, x the vector of n design variables, and g the vector of design constraints. These three parameters are called the optimisation model. The objective function is defined as the mass of the wingbox and the design variables are the skin, spar and rib thickness. In the first optimisation step, the design constraints are defined by various stress values.

- A second structural optimisation defines the resulting thickness obtained with the design constraints as the lower bound of the design variables. For this bound, only the aileron efficiency is a constraint and the minimum structural mass of the wingbox is still the design objective.

Only stress constraints are used for the optimisation because it is more complex for the optimiser to converge with different types of constraint.

1.4 Calculation of Maneuver and Gust Loads

The maneuver loads are computed by MSC Nastran with the static aeroelastic solution sequence (SOL144), designed to perform quasi-steady aeroelastic analyses. This solution is able to compute the stability and control derivatives for the rigid aircraft but also for the restrained and unrestrained elastic aircraft. The equations of motion solved in SOL144 are expressed as follows:

$$[K_{aa} - \bar{q} Q_{aa}]\{u_a\} + [M_{aa}]\{\ddot{u}_a\} = \bar{q}[Q_{ax}]\{u_x\} + P_a,$$

where K_{aa} is the structural stiffness matrix, $\bar{q}$ the dynamic pressure, Q_{aa} and Q_{ax} the aerodynamic stiffness matrices, u_a the nodal displacement vector, $\ddot{u}_a$ the nodal acceleration vector, M_{aa} the structural mass matrix, u_x the control and rigid body motion variables and P_a the applied loads.

The control and rigid body motion variable u_x can contain the angle of attack (α), the slip angle (β), the angular velocities (p, q, r), the translational accelerations $(\ddot{y}, \ddot{z})$, the angular accelerations $(\dot{p}, \dot{q}, \dot{r})$ and the control surface deflections (η_{CS}). If the number of equations is equal to the number of unknowns, the solution is explicit.

The gust loads are computed by MSC Nastran with the dynamic aeroelastic solution sequence (SOL144), designed for the dynamic aeroelastic analyses in the frequency domain. As for the flutter analyses, the DLM is used to compute the aerodynamic loads. The equations of motion of the SOL 146 are expressed:

$$[-M_{hh}\omega^2 + iB_{hh}\omega + K_{hh} - \bar{q}Q_{hh}(M,k)]\{u_h\} = \{P_h(\omega)\},$$

with all the parameters already defined in Chapter 1.3.

1.5 Structural Optimisation Loops and Convergence Criteria

The structural optimisation loop starts with the extraction of the stiffness model and the loads analysis of the flexible aircraft with Nastran solution 144. The gust loads are computed using Nastran solution 146. The load cases are selected, evaluated and used as the inputs of the loads and control efficiency optimiser. These optimisation processes are explained in Chapter 1.3 and used to update the mass model and compute the resulting structural mass of the wingbox. The loads analysis is done again using the structural properties computed by the optimiser, the design loads are estimated and the structural optimisation is performed again. This process of loads analysis, design load estimation and structural optimisation is repeated until the convergence of the structural mass and the maximum bending moment of the wing-like components.

The structural mass and maximum bending moment of the aircraft are used as the convergence criteria of the loop. They are both initiated at 0.1 and are simply calculated by:

$$\varepsilon = \frac{x^i - x^{i-1}}{x^{i-1}}, \tag{1.3}$$

where x can be the load or the mass.

Chapter 2

The DLR F25 configuration (Baseline)

The baseline aircraft as well as its mission will be described in this chapter. The mass and load cases used to perform simulations will be defined and the generated models (structural and aerodynamic) will be shown and described. Then, the results obtained with the baseline configuration as well as the aerodynamic and structural characteristics, the aircraft stability, the gust loads and flutter characteristics will be analysed.

2.1 Key Features

The DLR-F25 is a high aspect ratio wing transport aircraft concept mainly developed by DLR. The objectives of this aircraft are the efficiency increasing and CO_2 reduction through a Ultra Performance (UP) wing concept. The aim of the UP wing is to reduce the fuel burn by 30% compared to the reference aircraft, the Airbus A321neo [16]. This aircraft is designed to have a range of 4600 km when it takes off with the maximum payload and fuel. Its range is 7600 km when it takes of with the maximum fuel and with no payload. This aircraft can transport a maximum payload of 25 tons. Its conceptual design cruise Mach number and flight altitude are 0.78 and 10360 m, respectively. For these flight conditions at the maximum take-off weight, the design lift coefficient is 0.61. However, the cruise conditions computed in the preliminary design stage and used for the loads analysis are different. The cruise Mach number and flight altitude are 0.82 and 8000 m, respectively. The lift coefficient for these flight conditions is 0.47. Four selected views of the DLR-F25 are shown in Figure 2.1.
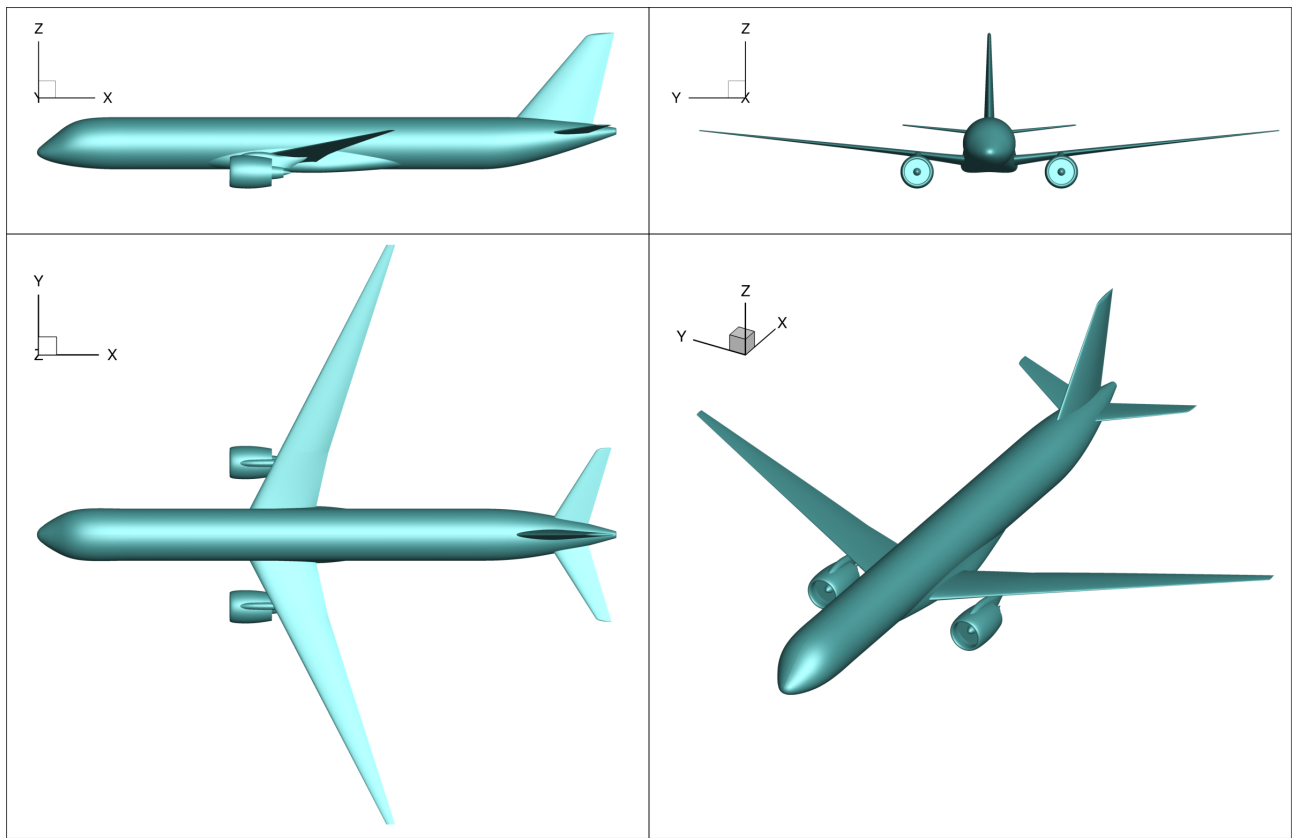
Figure 2.1: Four views of the DLR-F25 baseline configuration, derived from the CPACS dataset.

The wing planform as well as the horizontal and vertical tail planes are shown in Figures 2.2 and 2.3. As it can be seen, the wing is very narrow in comparison with similar aircraft like the Airbus A320.
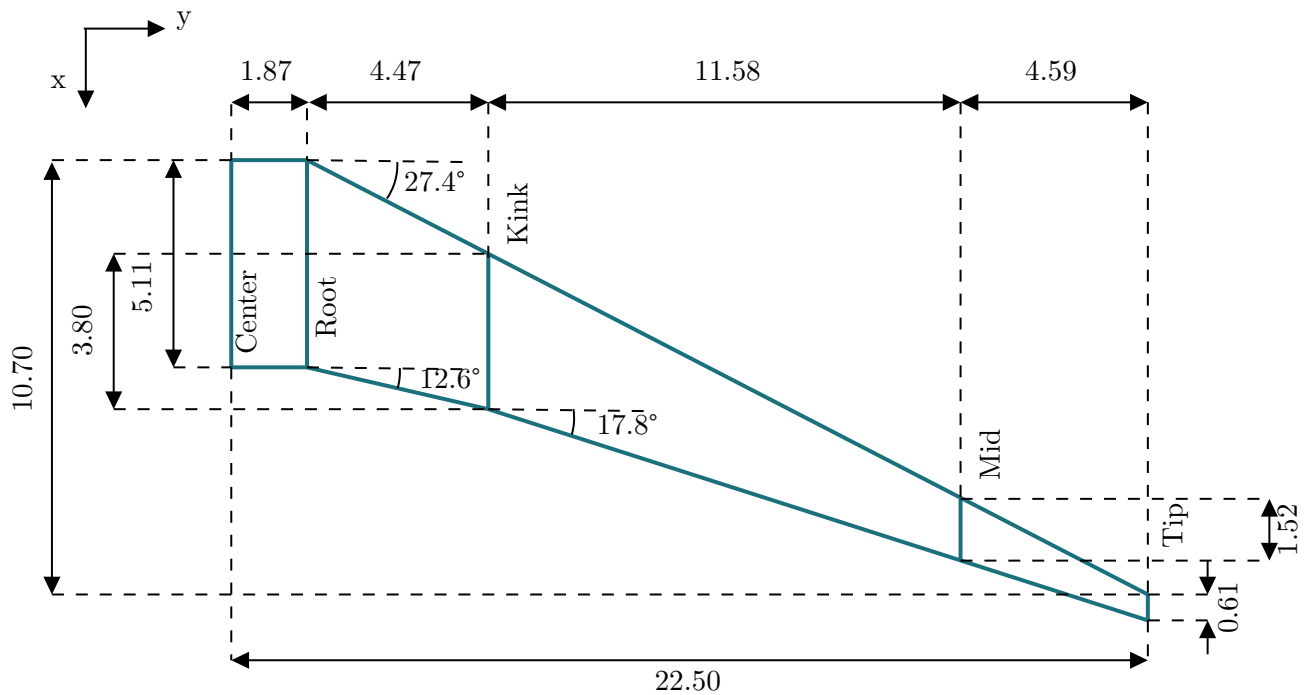
Figure 2.2: Wing baseline geometry, dimensions in meter.
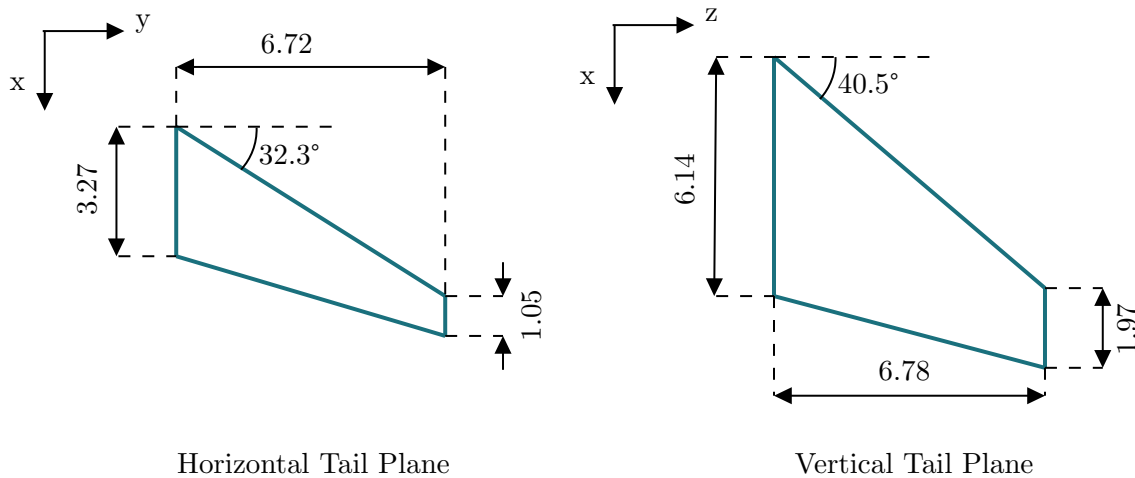
Figure 2.3: Horizontal and vertical tail plane geometry, dimensions in meter.

For the wing aspect ratio increasing methods, the horizontal and vertical tail planes will stay unchanged. The key characteristics of the DLR-F25 wing and tail planes are presented in Tables 2.1 and 2.2.

Parameter	Unit	Wing	HTP	VTP
Reference Area	[m^2]	130.1	29.0	27.5
Span	[m]	45	13.4	6.8
Aspect Ratio	[-]	15.6	6.22	1.67
Taper Ratio	[-]	0.12	0.32	0.32
MAC	[m]	3.54	2.35	4.41
Lever Arm	[m]	-	20.8	19.7
Volume Coefficient	[-]	-	1.30	0.09

Table 2.1: Key characteristics of the wing and tail planes of the DLR-F25.

Wing section	Dihedral [deg]	Twist [deg]
Center	0	3.00
Root	0	3.00
Kink	8.30	1.50
Mid	6.40	0.78
Tip	6.40	-1.00

Table 2.2: Key characteristics of the wing of the DLR-F25.

The lever arm refers to the distance between the wing and the horizontal/vertical tail plane aerodynamic centers and the volume coefficient of the vertical and horizontal tail plane is obtained with:

$$C_H = \frac{S_H \cdot l_H}{S_W \cdot \bar{c}} \qquad \text{and} \qquad C_V = \frac{S_V \cdot l_V}{S_W \cdot b},$$

where the indices H, V and W refer to the horizontal, vertical tail planes and wing. S is the surface, l the lever arm, $\bar{c}$ the wing mean aerodynamic chord and b the wing span.

The wing is divided in 5 sections: center, root, kink, mid and tip. Similar middle range transport aircraft like the Airbus A320 have an aspect ratio of 9-10 and a tapper ratio of 0.2 - 0.3 but the DLR-F25 baseline configuration has an aspect ratio close to 16 and a taper ratio of 0.12. The DLR F25 is an ultra high aspect ratio which means it does not generate a lot of induced drag.

The wing planform including all the control surfaces is illustrated in Figure 2.4. For the aspect ratio variation study, these control surfaces will keep the same relative coordinates in the spanwise and chordwise direction. The aircraft uses these control surfaces for both maneuver (MLA) and gust load alleviation (GLA). This reduce stresses in the wing by an optimal load distribution. The flaps are deflected to shift

the load distribution inboard, i.e towards the wing root. Thus, bending moments about the x axis are reduced, which allows to have thinner wing skin and therefore a lighter wing.
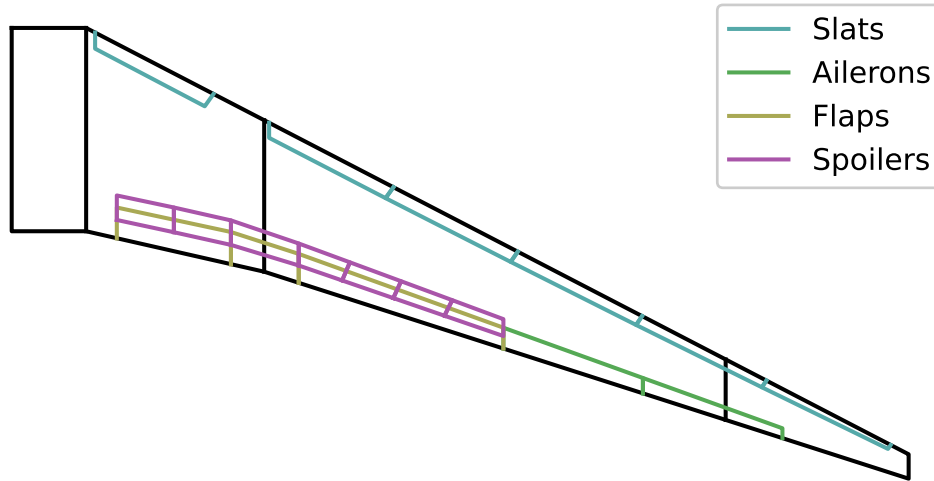
Figure 2.4: Control surfaces of the DLR-F25 right wing.

The DLR-F25 engine is a turbofan with a fan radius of 1.07 m, a bypass-ratio of 15 and an overall pressure ratio of 64.8 that can produce an equivalent static thrust (sea-level) of 114 kN. This 2630 kg engine needs a nacelle with a length of 3.53 m and diameter of 2.77 m which represent a wetted area of 27.1 m^2. The DLR-F25 has two of these engines located in the inner part of the wing, just before the kink as can be seen in Figure 2.1.

2.2   Mass and Load Cases Definition, Weight and Balance

In this work, 4 different mass cases will be analysed and for each mass case, 63 load cases will be used to optimise the structure of the aircraft. The 4 mass cases are listed in Table 2.3.

	MFOeF	MOOee	MTOAa	MZOAe
Design Mass	–	OWE	MTOW	MZFM
Total Mass [T]	69.313	50.369	85.954	75.369
Payload [%]	0	0	100	100
Payload [t]	0	0	25	25
Fuel [%]	100	0	55.89	0
Fuel [t]	18.94	0	10.59	0

Table 2.3: Mass cases definition.

The first mass case is labelled as "no payload and maximum fuel". The second one is the empty case, the third is the maximum take off weight and the last one is the maximum payload and no fuel. All these mass cases are very important to create the structural stiffness of the aircraft. Figure 2.5 shows the aircraft total mass and center of gravity related to each mass cases. It can be observed that for each mass case, the center of gravity is located between 10% and 40% of the mean aerodynamic chord position. It is very important for the center of gravity to fall within this range for maintaining longitudinal stability and control of the aircraft. A bad position of the center of gravity can also lead to structural issues or limit the aircraft's maneuverability.
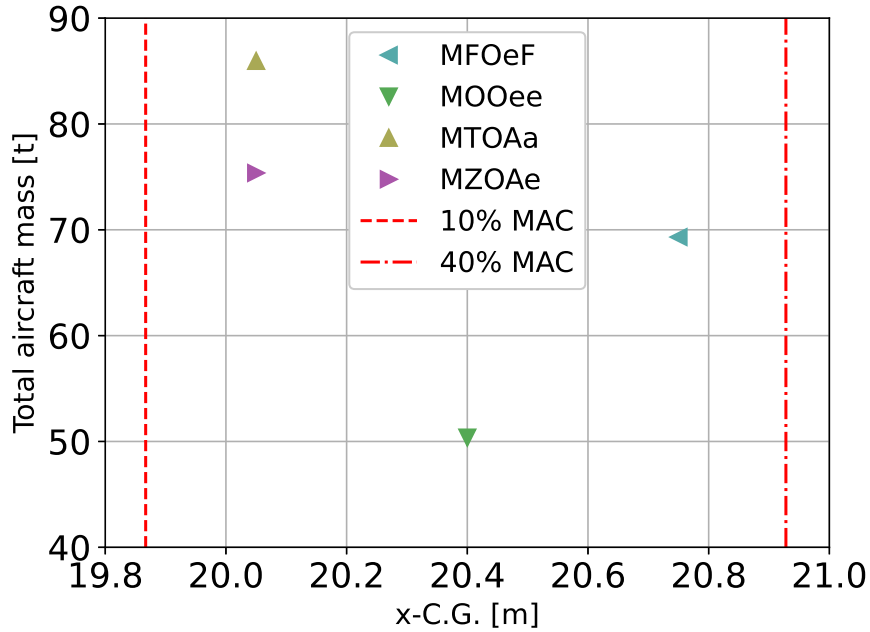
Figure 2.5: Aircraft total mass and center of gravity for the four different mass cases.

The different load cases are defined by the load case ID which is composed of four parts: C.M.O.L [17].

- C stands for the aircraft configuration. It can be clean, take off, landing, etc but in this thesis, only the clean configuration as well as maneuver load configuration are used.

- M stands for mass case as previously defined.

- O stands for the operational state. It defines the velocity and altitude (in 100 feet).

- L stands for load condition. It defines the type of maneuver. Each flight case is in stationary flight regime.

For example the load case CCD.MFOeF.OC262.LLFPU means clean aircraft with direct control law, no payload and maximum fuel, cruise velocity at 26 200 feet, limit flight stationary case, pull-up maneuver.

There are 4 important load conditions: the cruise condition (1g), pull-up maneuver (2.5g), push-down maneuver (-1g) and rolling maneuver (1.67g). All theses load conditions will be used for the cpacs-MONA simulation process but one will focus on the cruise condition for results analysis. A V-n diagram of the DLR F25 baseline configuration is represented in Figure 2.6. The velocities used for this graph are explained in detail in the next section. The normal flight envelope is in this zone between stall and cruise velocity. The zone between cruise and dive velocity is called caution zone. Aircraft can flight in the zone but only if it is necessary. The region on the left of the envelope is the stall region. In the region above, under and on the right of the envelope, structural damages or failures can happen. Indeed, the aircraft is not designed to resist to extreme load factor and velocities.
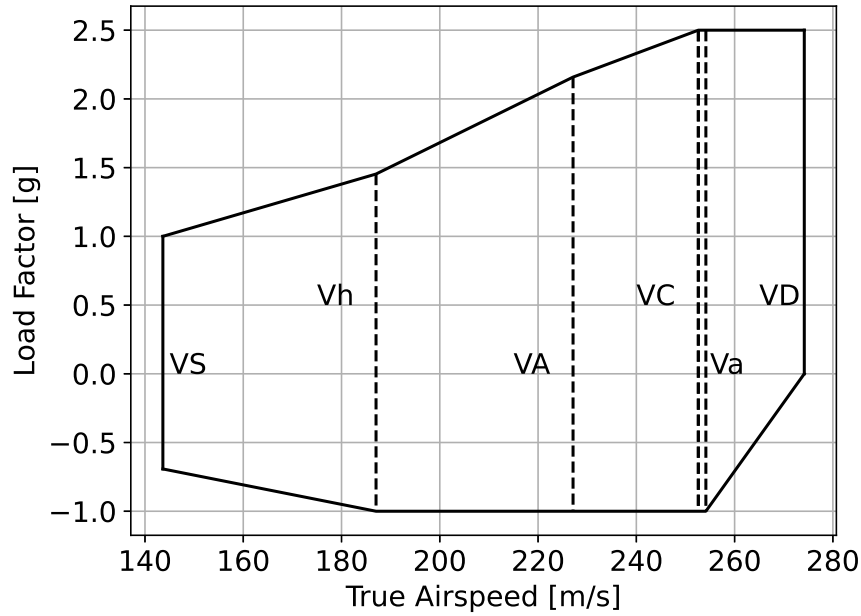
Figure 2.6: V-n diagram of the DLR-F25.

2.3 Design Speeds

The structural design speeds are defined within "LCspeed" in CPACS data-set and are required for loads calculation [18]. This tool can be used for aircraft certified under the CS25, CS23 and CS22 which are the Certification Specifications adopted by the European Union Aviation Safety Agency (EASA) to meet the essential requirements of the Basic Regulation [19]. For the DLR-F25, the CS25 is used. The design speeds are the following:

- The design cruise velocity VC is directly defined by the user through the design maximum operational velocity VMO and Mach number MMO.

- The design dive velocity VD is the highest velocity planned to be achieved. For the DLR-F25 configuration, its corresponding Mach number is defined by [18]:

$$MD = MC + 0.07,$$

with MC the Mach cruise number.

- The stall velocity is calculated by:

$$VS = \sqrt{\frac{n_z \cdot W}{\frac{1}{2} \cdot \rho \cdot S \cdot C_{L,max}}},$$

where n_z is the load factor, W the maximum take-off weight, ρ the air density, S the wing surface and $C_{L,max}$ the maximum lift coefficient. There are 3 different stall velocity computed with almost the same formula but using different load factors. VS and Va are obtained for load factors of 1 and 2.5, respectively. Vh is computed for a load factor $n_z = |-1|$ and a maximum lift coefficient $C_{L,max} = |C_{L,min}|$

- The design gust velocity VB is computed with the same formula than the stall velocity but using the gust load factor. It is expressed as follows:

$$n_g = 1 + \frac{\frac{1}{2} \cdot \rho_0 \cdot S \cdot VC^2 \cdot \Delta\alpha_g \cdot C_{L_\alpha}}{W} \qquad \text{where} \qquad \begin{cases} \Delta\alpha_g & = K_g \cdot \frac{w_{g,EAS}}{VC} \\[2mm] K_g & = \frac{0.88 \cdot \mu_g}{5.3 + \mu_g} \\[2mm] \mu_g & = \frac{W}{\frac{1}{2} \cdot \rho \cdot \bar{c} \cdot C_{L_\alpha} \cdot g} \end{cases} ,$$

with ρ_0 the air density at sea level, $\Delta\alpha_g$ the incremental gust angle of attack, C_{L_α} the lift coefficient derivative, K_g the Pratt gust alleviation factor, $w_{g,EAS}$ the gust equivalent airspeed, μ_g the aircraft density parameter for gust and g the gravity acceleration.

- The design maneuver velocity VA is defined by:

$$VA = VS \cdot \sqrt{n_1} \qquad \text{with} \quad n_1 = 2.5 \tag{2.1}$$

These design speeds are represented as a function of altitude in Figure 2.7. It can be noticed that at the cruise altiude, the gust and cruise velocities are the same.
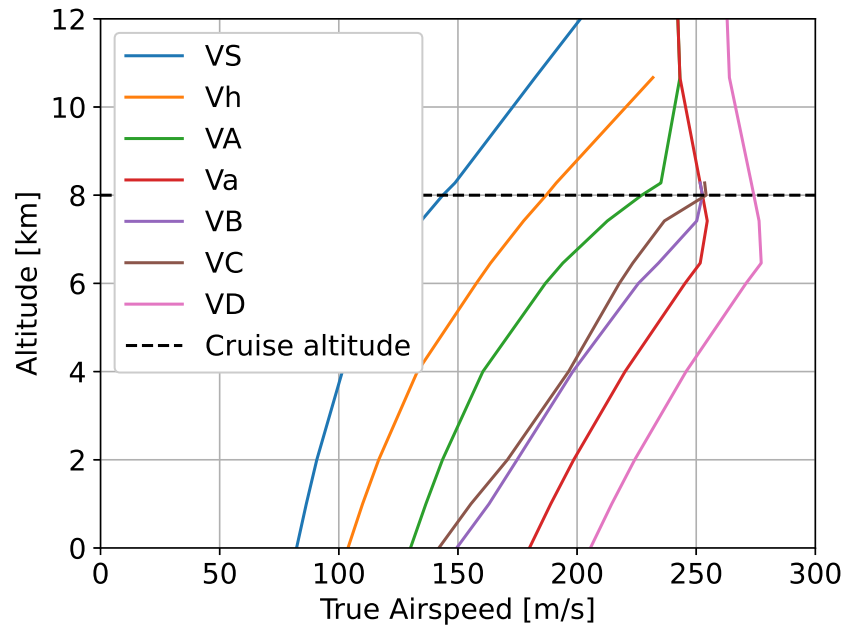
Figure 2.7: Velocity variation as a function of the altitude for the DLR-F25.

2.4 MSC Nastran Aerodynamic and Structural Models for Maneuver Loads, Gust Loads, and Flutter

As mentioned in Chapter 1.3, cpacs-MONA simulations use MSC Nastran to compute aerodynamic, aeroelastic and structural characteristics of the aircraft. The corresponding finite element models are generated by ModGen and directly used by MSC Nastran.

2.4.1   Aerodynamic Model

The first model is the aerodynamic model. It is composed of a slender body for the fuselage and an interference tube to simplify the interference between the fuselage and the other components. The wing, vertical and horizontal tailplanes, engines and pylons are simplified by 2D doublet panels. For the fuselage, source panels are used. The Aerodynamic model of the DLR-F25 baseline configuration is shown in Figure 2.8.
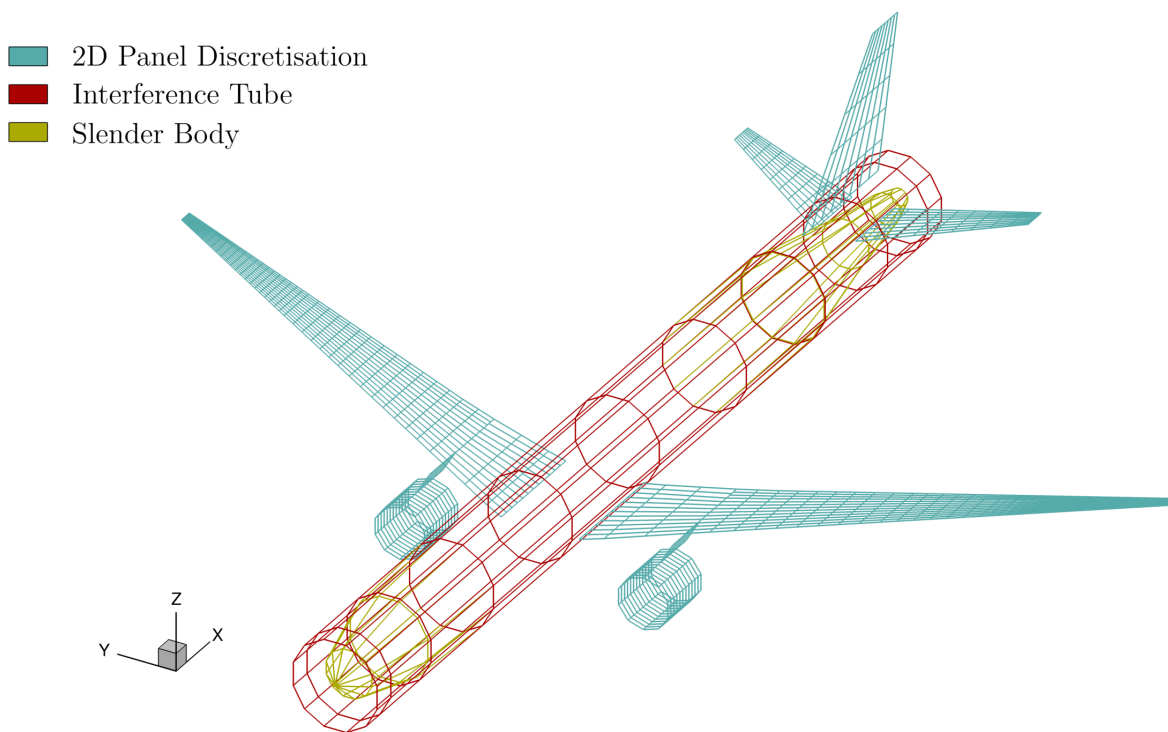
Figure 2.8: Aerodynamic model of the DLR F25 baseline configuration generated by ModGen.

The number of panels of the wing and tailplanes in the chordwise direction is an input of cpacs-MONA that can be modified into the CPACS dataset file, while the number of panels in the spanwise direction is automatically generated by ModGen. However, sometimes, due to the control surface definition, the number of panels along the chord can also be adapted by ModGen. For the wing of the DLR-F25 baseline configuration, the number of panels along the chord is 12 and in the spanwise direction is 40 (only from the root to the left/right tip). No convergence analysis regarding the aerodynamic grid is done. Indeed, even if the user can change some mesh parameters, cpacs-MONA makes sure the aerodynamic grid is fine enough to applied loads, and correctly run the simulation.

2.4.2   Structural Model and Material Definition

The structural model, also generated by ModGen, is completely different that the aerodynamic model. A more refined mesh is needed to correctly simulate the structure. As it can be seen in Figure 1.4, the wing skin, spars webs and ribs use shell elements and the pylons, stringers, spars upper and lower caps and the spars and ribs stiffeners use bar elements. Each node of the shell elements has 6 degrees of freedom (3 translations and 3 rotations) while each node of the bar element has only one degree of freedom (in the axis of the bar). One again, no convergence study is done and cpacs-MONA automatically generates the FE model in order to correctly run the simulation. Figure 2.9 shows the structural model of the whole aircraft while Figure 2.10 shows the internal structure of the wing (ribs and spars). The properties of

the composite materials and aluminium 2024 used for the wing structure are defined by MSC Nastran as represented in Tables 2.4 and 2.5.
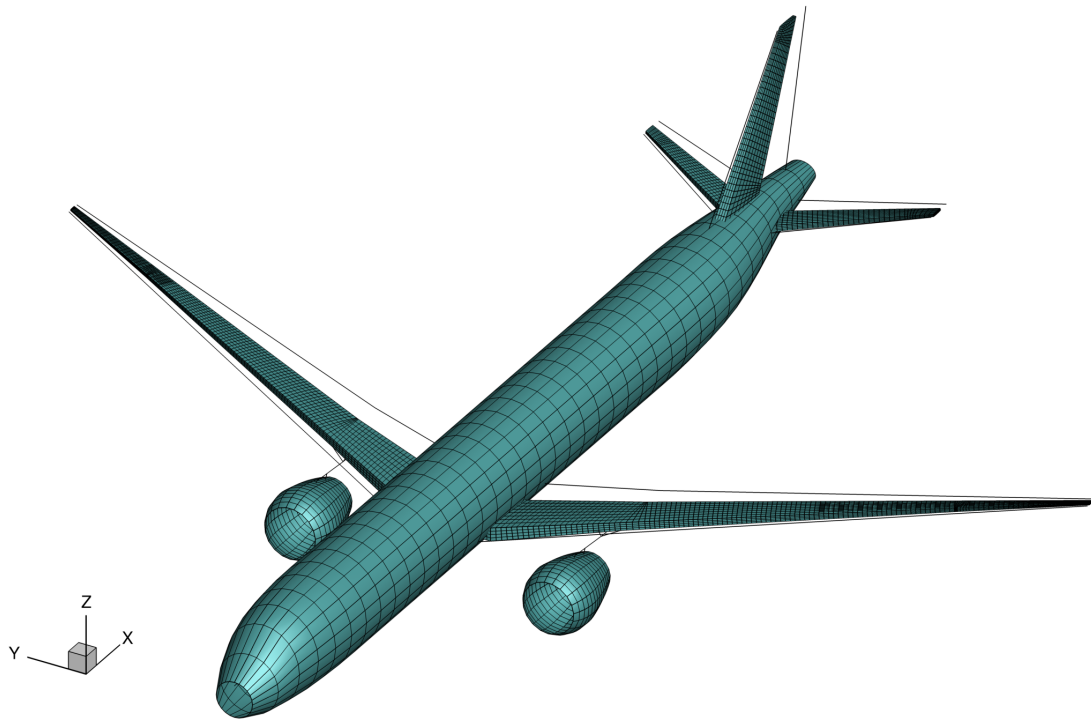
Figure 2.9: Aircraft FEM-structure generated by ModGen.
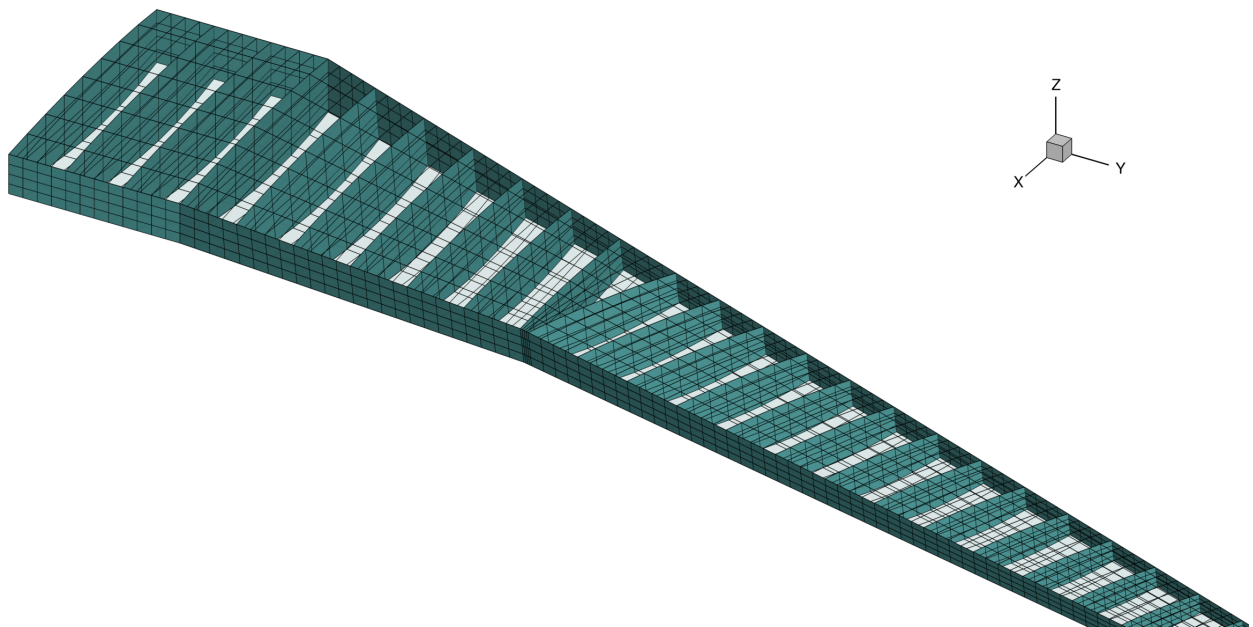
Figure 2.10: Wing FEM-structure generated by ModGen.

Material name	Properties	G_{11}	G_{12}	G_{13}	G_{22}	G_{23}	G_{33}	ρ [kg/m^3]
"60_30_10"	Membrane	1.07e11	1.35e10	1.09e10	2.44e10	1.09e10	1.47e10	1500
	Bending	8.31e10	2.60e10	2.39e10	3.35e10	2.39e10	2.72e10	1500
"20_60_20"	Membrane	6.03e10	2.40e10	2.18e10	6.03e10	2.18e10	2.52e10	1580
	Bending	5.21e10	3.57e10	3.40e10	4.51e10	3.40e10	3.69e10	1580

Table 2.4: Composite membrane and bending material properties used for the wing, G in Pa.

Material name	E	G	ν [-]	ρ [kg/m^3]	σ_t	σ_c	τ
"Aluminium 2024"	7.38e10	2.77e10	0.330011	2800	4.412e8	4.412e8	2.620e8

Table 2.5: Material properties of the aluminium 2024 used for the wing, E, G, σ_t, σ_c, and τ in Pa.

The wing skin is made of the composite material "60_30_10", the spar web and the rib cross section are made of the composite material "20_60_20" and all the bar elements are made of Aluminum 2024.

2.4.3   Optimisation Model Including Design Variables, Responses, and Constraints

For the optimisation model, design variables, responses and constraints are used. The design variables are the thicknesses of the elements of selected parts of the structure. For the wingbox and the tail planes, these include the skins, the spars, and the ribs. The constraints can be applied on the design variables and responses and are the boundaries that the optimiser must not exceed. The optimiser also needs an objective function. In general, for aircraft, this objective function is the mass and the goal of the structural optimisation is the reduction of the mass.

cpacs-MONA only uses one kind of design variable, the skin thickness. For the wing, this variable has to be between 2 mm and 30 mm. The design responses are the strain and stress. For the wing, the strain has to be between -3500 and 4000 microstrains.

First, the wing skin thickness distribution is initiate to a certain value. The stress and strain applied to the wing are computed and evaluated. If they are out of the range, another skin thickness distribution is defined until the constraints are respected. The optimiser repeats this until the minimum possible mass is reached.

2.5   Aerodynamic, Flight Mechanic, and Structural Properties of the Baseline Configuration for Different Mass Cases

cpacs-MONA has been used for the DLR-F25 baseline configuration in order to extract aerodynamic, aeroelastic and structural properties of the aircraft. First, the aerodynamic properties as the pressure or the lift distributions will be discussed. The longitudinal flight mechanic stability (static margin) of the aircraft will be determined, structural characteristics, such as the wing deformation or mode shapes will be shown and finally, it will be determined whether there is flutter within the flight envelope.

2.5.1   Lift Distributions

Figure 2.11 represents the pressure coefficient difference along the wing. The pressure coefficient is defined as follows:

$$c_p = \frac{p - p_\infty}{\frac{1}{2} \cdot \rho_\infty \cdot V_\infty^2},$$

with p the static pressure, p_∞ the free stream pressure, ρ_∞ the free stream density, and V the free stream velocity.

The pressure coefficient difference is the difference of pressure coefficients between the upper surface and the lower surface of the wing.

Obviously, for heavier mass cases like the maximum take-off weight, more lift is needed and the pressure coefficient difference is higher, especially on the leading edge. Another thing that can be noticed is that there are negative pressure coefficient difference close to the tip and it is more visible for the empty mass case in Figure 2.11b which means there is more down lift at the tip for this case. It can come from the fact that because more lift is needed for heavy mass cases, the wing bending is more important, and then there is less negative lift at the tip. Indeed, due to bending moment, the direction of the lift is not exactly in the vertical axis but also in the horizontal axis. In general, the results obtained for the pressure coefficient difference look coherent and there is no singularity observed. Δc_p is higher at the leading and trailing edge as expected.

From the pressure coefficient difference, the lift coefficient and the lift along the span can be determined as follows [20]:

$$c_l = \frac{1}{2} \sum_{i=1}^{n-1} \left(\Delta c_p(x_i) + \Delta c_p(x_{i+1}) \right) \frac{\Delta x}{c},$$

with $\Delta c_p(x_i)$ the coefficient difference at the discrete coordinate x_i of the airfoil, Δx the distance between two consecutive discrete point of the airfoil (Δx is constant), n the number of discrete point on the airfoil and c the airfoil chord length. It can be notice that only the pressure coefficient difference is computed with the Doublet Lattice Method, not the pressure coefficient of the upper and lower surface of the wing.

(a) MFOeF

(b) MOOee

(c) MTOAa

(d) MZOAe
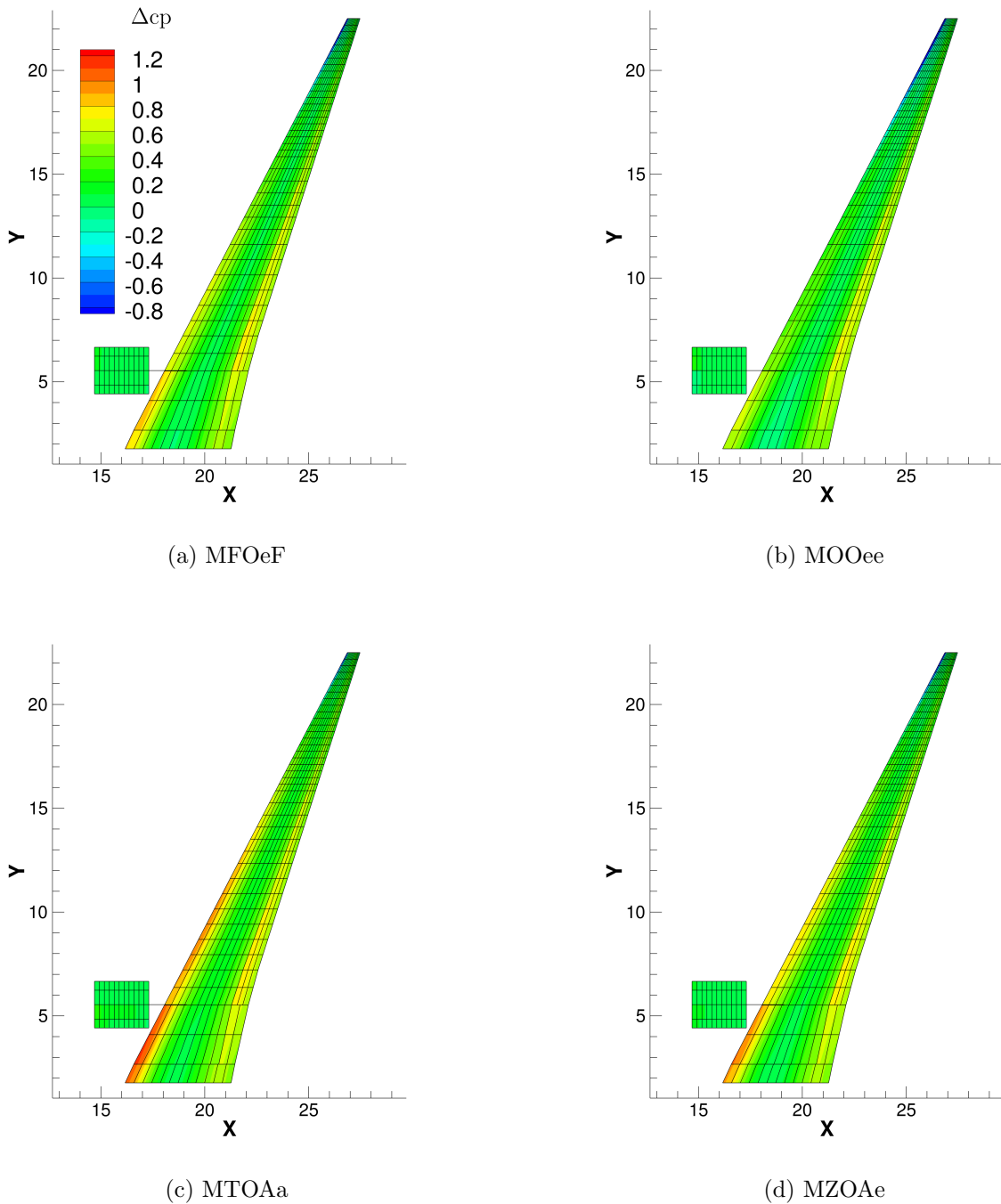
Figure 2.11: Pressure coefficient difference along the right wing for different mass cases during cruise condition.

Figure 2.12 show the lift coefficient and lift distribution along the wing span. In Figure 2.12a the wing lift coefficient distribution is very similar between each mass case. The only visible difference is that there is a shift in the values. Once again, it is obvious that the heavier the mass case, the higher the lift coefficient. It also can be seen that the lift and lift coefficients are only related to the wing. Indeed, the first monitoring point is located at the wing root and not at the center. Another part of the lift comes from the fuselage or the horizontal tail plane but only the main part that comes from the wing will be

analysed. As explained before, it can be seen in Figure 2.12b that there is a negative lift at the tip. It allows to reduce wing bending.

(a) Lift coefficient

(b) Lift
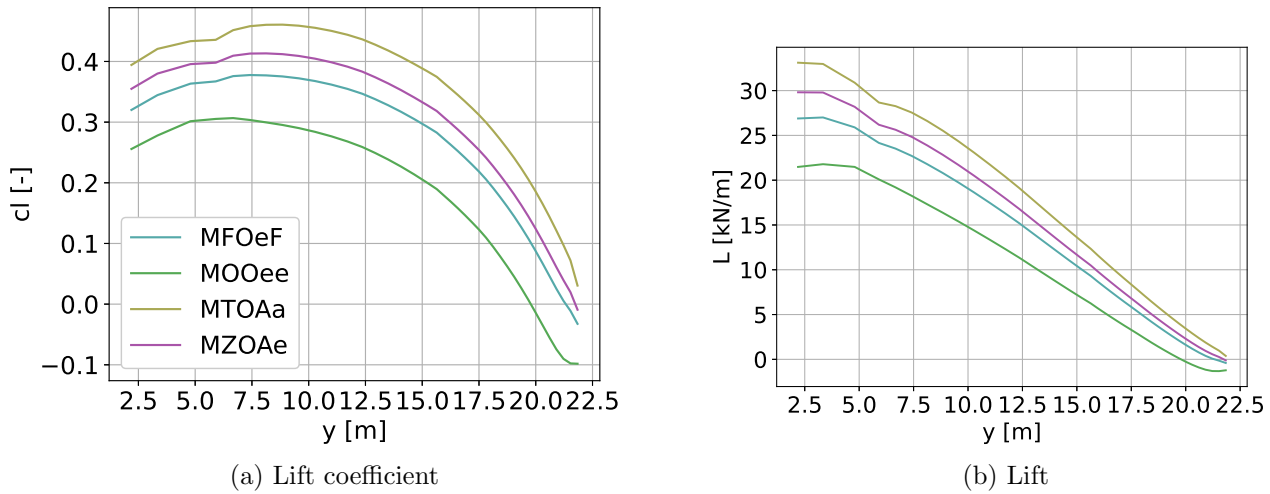
Figure 2.12: Lift coefficient and lift distribution along the wing span for the four different mass cases.

2.5.2   Stability Margin

The Stability margin is very important in order to ensure the longitudinal (or pitch) stability of the aircraft. It is expressed as follows:

$$K_n = \frac{x_{AC} - x_{CG}}{\bar{c}} = -\frac{dC_m}{dC_{L_W}},$$

with x_{AC} the x coordinate of the aircraft aerodynamic center, x_{CG} the x coordinate of the center of gravity, C_m the pitching moment, C_{L_W} the wing lift coefficient and $\bar{c}$ the mean aerodynamic chord.

This margin has to be positive for a stable aircraft and has to be higher than 5% according to certification authorities. However, this margin cannot be too high because else, the aircraft is too stable and not maneuverable anymore [21]. In general, it should not exceed 30%. A positive stability margin means that the aerodynamic center is behind the center of gravity. The stability is only considered for the cruise condition, not for maneuvers because maneuvers are not steady flight conditions. The center of gravity, aerodynamic center and stability margin of the elastic aircraft for each mass cases are in Table 2.6.

Mass case	MFOeF	MOOee	MTOAa	MZOAe
x location of center of gravity [m]	20.75	20.40	20.05	21.05
x location of aerodynamic center [m]	21.26	21.33	21.30	21.31
Stability margin [%]	14.3	26.4	35.0	35.6

Table 2.6: Aircraft stability parameters for different mass cases.

For the first two mass cases, the stability margin is good, the aircraft is stable and still maneuverable. However, for the last two mass cases, the stability margin is too high. The aircraft is very stable but not very maneuverable anymore. It is because for the baseline configuration, the center of gravity is imposed. Indeed, it depends on the payload disposition and still can move so theses cases are not relevant in term of stability.

2.5.3 Wing Thickness Distribution and Static Wing Deformation in Maneuvers

Figure 2.13 shows the wing structure made of ribs, spars, upper and lower skins, and their thickness distribution.
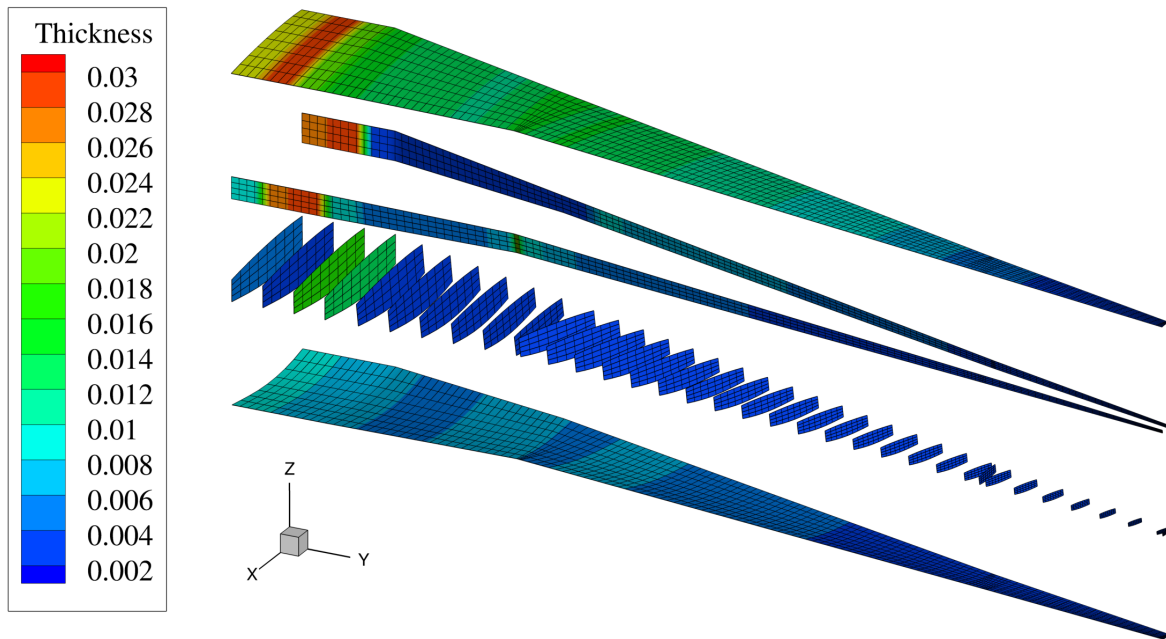
Figure 2.13: DLR F25 baseline wing elements thickness distribution, in meter.

At first, as explained in Chapter 2.4.3, the material thickness of the wing is constrained and has to be between 2 mm and 30 mm. It can be see that at the wing root, the material thickness is larger. The upper skin, and spars are 30 mm thick while the ribs are 15 mm thick. The structure has to be more resistant at the root because large shear loads and moments are produced near the wing root.

For both upper and lower skin, the thickness decreases from the root to the tip, however, the upper skin is thicker than the lower skin. It can be explained by the fact that the airfoil profile is not symmetric. The upper surface of the wing is subject to higher aerodynamic loads than the lower surface. This creates compressive forces on the upper skin. The upper surface is therefore more susceptible to buckling and need to be thicker. Except at the root location, the ribs and spars are very thin along the wing.

This is important to notice that elastic and rigid aircraft are very different. The wing bending and the twist deformation can be observed in Figures 2.14a and 2.14b for the cruise condition. Once again, knowing that the wing stiffness is the same for each mass cases, the heavier the aircraft, the higher the wing bending. Indeed, the wing need to generate more lift which means more vertical force and then, more vertical displacement. In this configuration, the maximum wing bending only represents 6% of the half span. For the twist deformation along the span, the results look very close between each mass case. The largest value of twist deformation is only -3.3°. The bending and twist deformations are coupled and have therefore an impact on each other. The twist deformation is negative because the center of pressure is behind the aerodynamic center of the airfoil.

(a) Vertical displacement
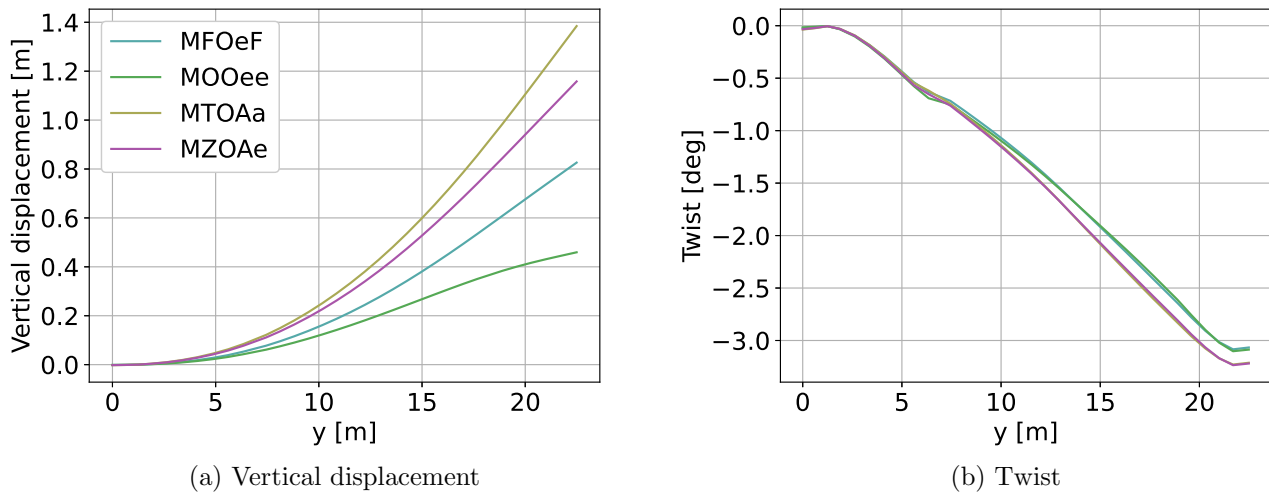
(b) Twist

Figure 2.14: Vertical displacement and twist along the wing span for the four different mass cases.

2.5.4 Modal Characteristics

As shown in Figure 2.15, each of the six rigid body mode shapes computed by MSC Nastran contains a mixture of translational and rotational degrees of freedom, i.e. they are not "aligned" with the axes of the body fixed coordinate system in which the FE model is defined. These modes are pure structural rigid modes, not dynamic or flight mechanics modes. These mode shapes look similar between each mass case, the main difference comes from the deformation factor.
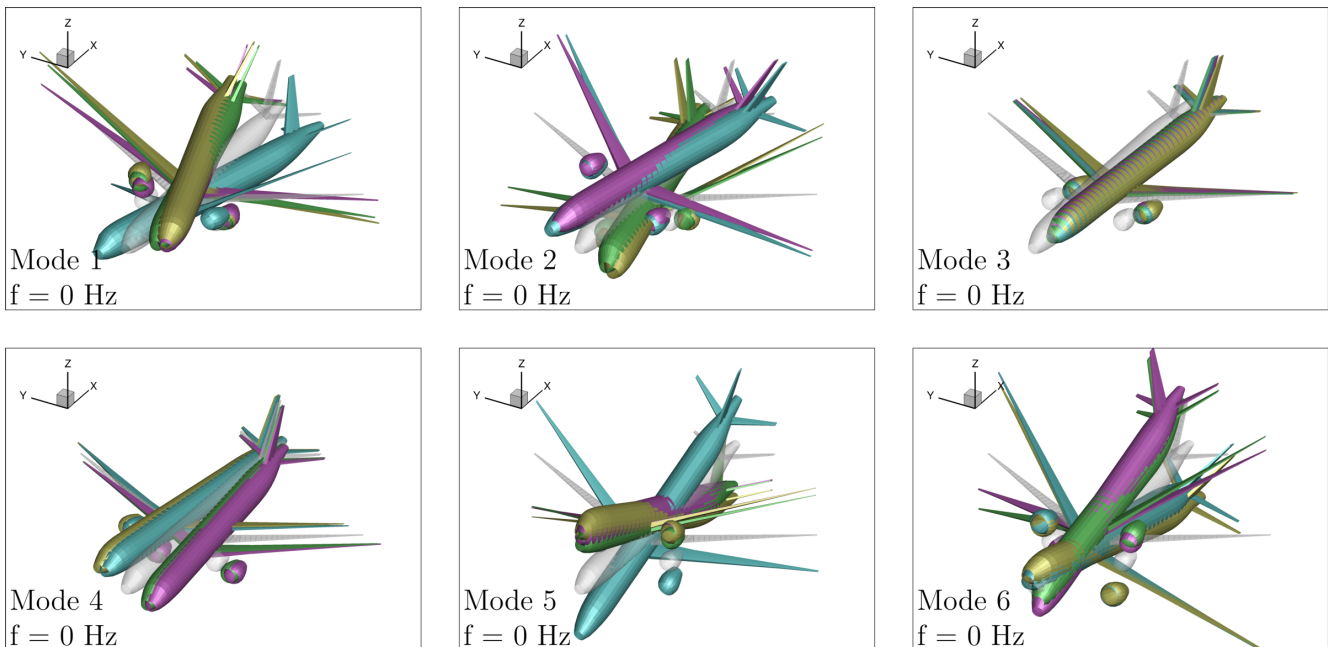
Figure 2.15: Rigid body mode shapes of the DLR F25 baseline configuration for all mass cases (MFOeF = blue, MOOee = green, MTOAa = yellow, MZOAe = purple and grey = FE model in jig-shape).

Figure 2.16 represents the first 12 elastic mode shapes for all mass cases. As expected, the first elastic mode (mode 7) is the first bending mode for each mass case. The second mode is an anti-symmetric bending mode and the third one is the first torsion mode. Indeed, as it can be seen, the wing with engines

rotate around the y axis and experience a twisting motion. It is very important to notice that the modes are sorted from the lowest to the highest frequency by MSC Nastran and the modes are not necessarily the same for each mass case. For example, modes 11 is symmetric for MOOee and MZOAe cases and anti-symmetric for MFOeF and MTOAa cases. This is the opposite for mode 12. It is essential to be careful when comparing modes. The same mode notation will be used for the rest of the thesis to be consistent.

Mode 7	Mode 8	Mode 9
f = 1.67, 2.27, 1.84, 2.23 Hz	f = 2.32, 2.66, 2.44, 2.65 Hz	f = 3.11, 3.16, 2.96, 2.99 Hz
Mode 10	Mode 11	Mode 12
f = 3.25, 3.70, 3.21, 3.37 Hz	f = 3.62, 3.86, 3.75, 3.85 Hz	f = 3.80, 4.19, 3.81, 4.08 Hz
Mode 13	Mode 14	Mode 15
f = 3.89, 4.42, 3.88, 4.10 Hz	f = 4.02, 4.55, 4.03, 4.40 Hz	f = 4.69, 5.97, 5.00, 5.67 Hz
Mode 16	Mode 17	Mode 18
f = 4.78, 6.16, 5.01, 5.75 Hz	f = 5.12, 6.33, 5.13, 6.24 Hz	f = 6.07, 6.59, 6.30, 6.52 Hz
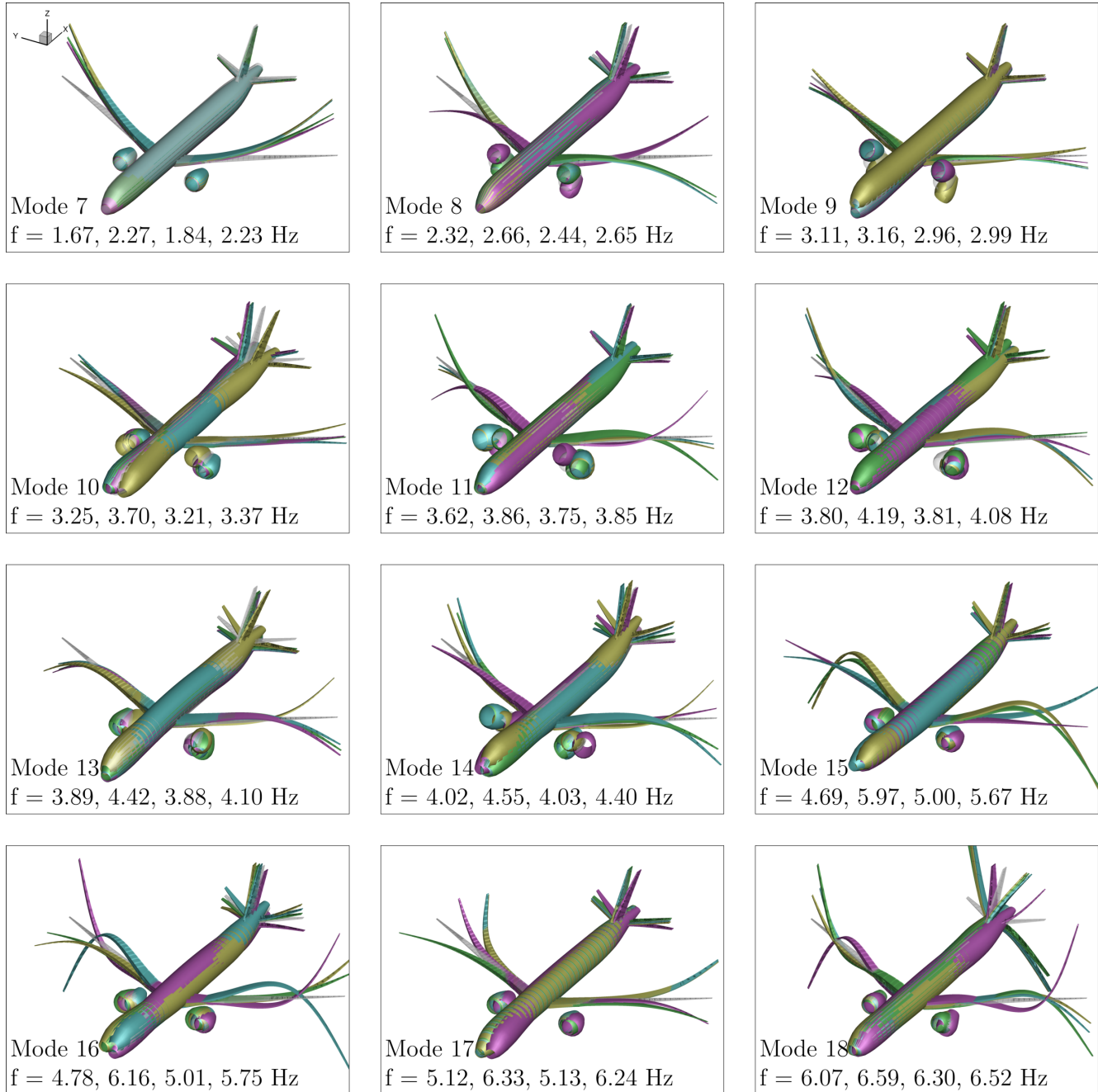
Figure 2.16: Elastic mode shapes of the baseline configuration for all mass cases (MFOeF = blue, MOOee = green, MTOAa = yellow, MZOAe = purple and grey = FE model in jig-shape).

2.5.5   Sectional Cut Loads of Maneuvers and Gust Loads

The loads applied on the aircraft like maneuver loads and gust loads allow to determine the load envelope. There are as many cut load envelopes as monitoring points on the wing. A monitoring point is used to monitor the loads in the local coordinate system. The right wing as well as the left wing are discretised by 42 monitoring points. Figures 2.17 and 2.18 show the bending moment Mx and the torsional moment My, respectively, along the wing for all mass and load cases. "W1_2" is the name of the right wing and eta is the relative coordinate along the span (eta $= 2 \cdot y/b$).
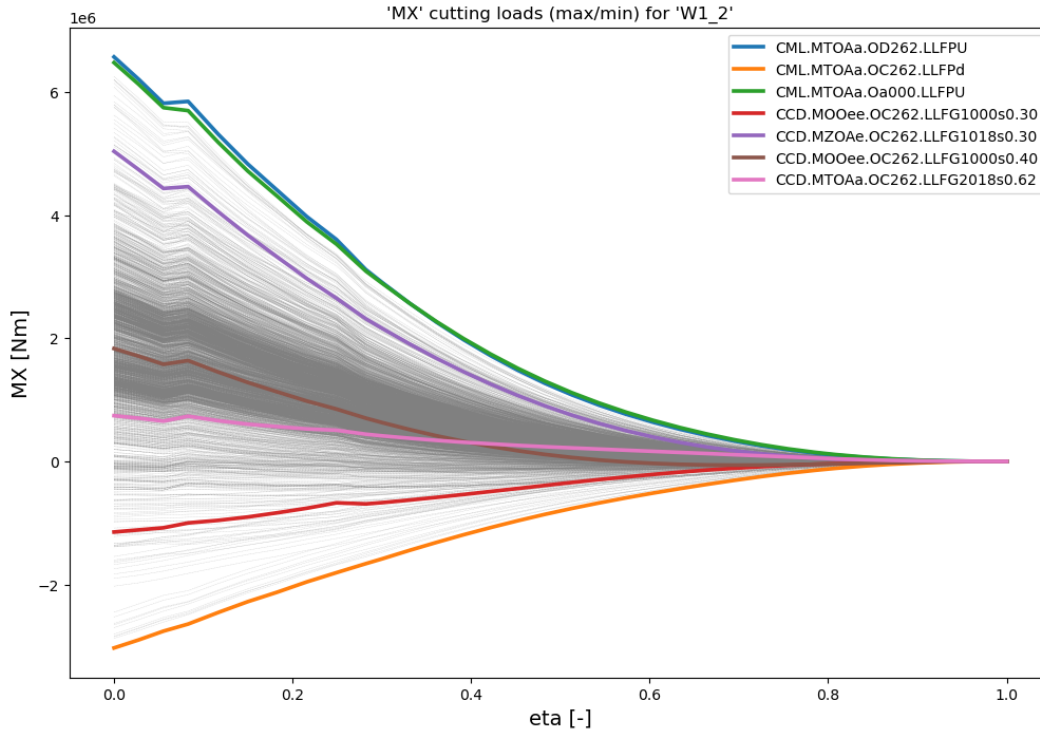

Figure 2.17: Bending envelope of the right wing over the span.

It can be seen in Figure 2.17 that the bending moment decreases in absolute value from the center to the tip which is expected. Indeed, the wing can be simplified by a beam embedded at one end (the symmetry plane xz). The upper limit of the bending moment (blue curve) is for the pull up maneuver (2.5g) at 8000m, at the dive speed and for the maximum take-off weight. The lower limit of the bending moment is for the push down maneuver (-1g) at 8000m, at the cruise speed and also for the maximum take-off weight. It is also interesting to notice the transition between the wing and the fuselage.

Figure 2.18 shows a decrease in absolute value of the torsional moment from the root to the tip. At the transition between the fuselage and the wing, the torsional moment abruptly changes. The upper limit from the wing root to the tip is for the push-up maneuver at sea level for the stall velocity at 2.5g. The lower limit is for the exact same load case as the lower limit of the bending moment.
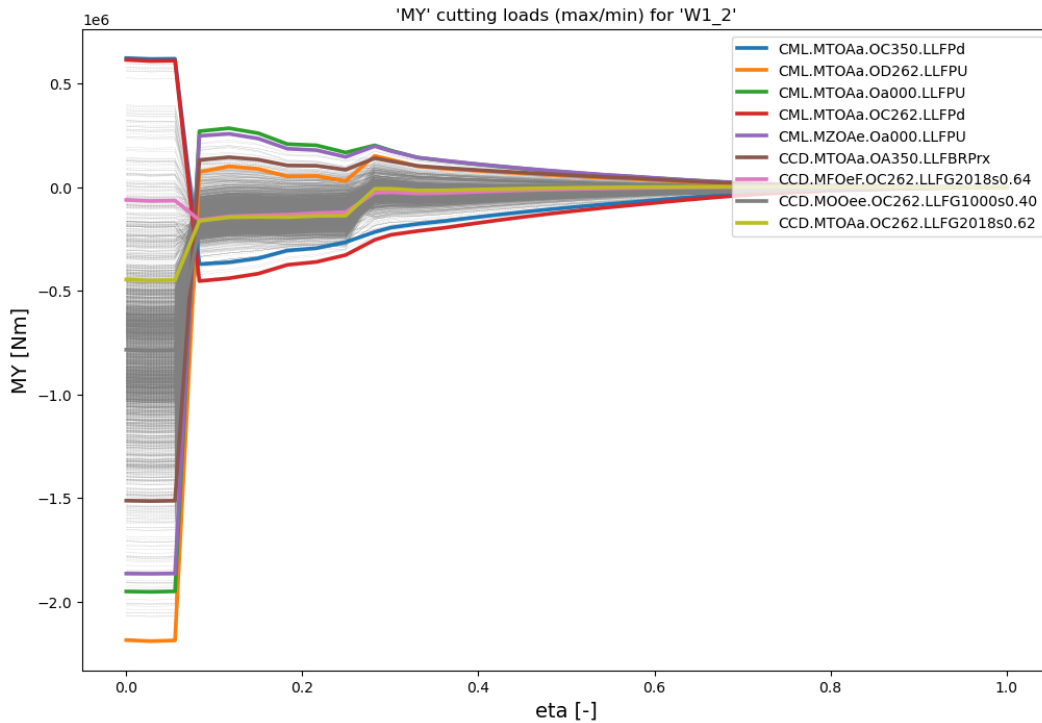
Figure 2.18: Torsional envelope of the right wing over the span.

One interesting envelope is close to the root because loads are more important there as shown in Figures 2.17 and 2.18. Indeed, the closer to the wing tip, the lower the loads. This is why the monitoring point CW64005, as shown in Figure 2.19, has been taken for the loads analyses.
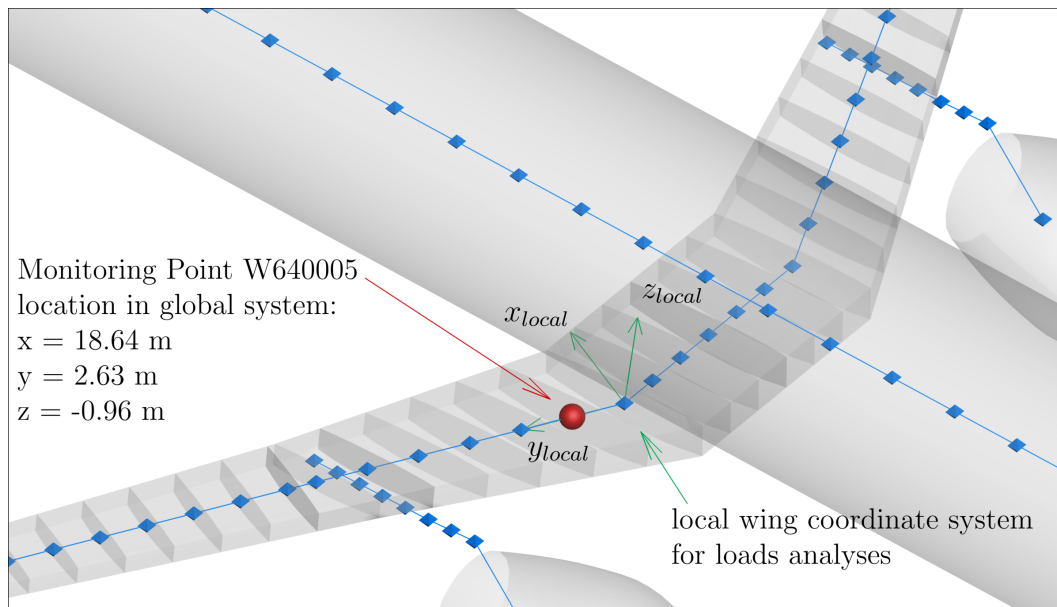
Figure 2.19: Location of the inner wing monitoring point used for the cut loads of maneuver and gust loads.

The cut load envelope is created with every maneuver loads and gust loads for every mass cases and gives a very good overview of the maximum and minimum loads applied to the aircraft. Figure 2.20 shows

the bending moment Mx about the local x axis and the torsion moment My about the local y axis as defined in Figure 2.19 for each load and mass cases.
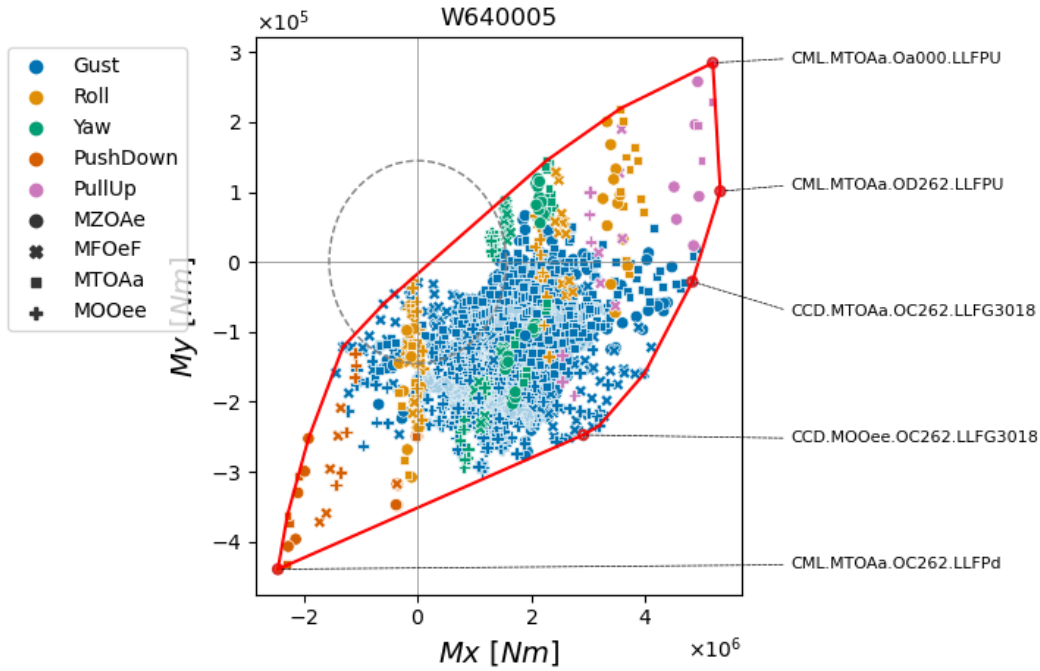
Figure 2.20: Sectional cut load envelope of the DLR-F25 baseline configuration at the monitoring point CW640005.

It is observed that there are a lot of load cases involved to define the cut load envelope and most of the loads are gust loads. As described in Figures 2.17 and 2.18, the cut load envelope at the monitoring point CW640005 has its maximum torsional moment for the pull-up maneuver at the sea level, its maximum bending moment for the pull-up maneuver at 8000m and their minimum torsional and bending moment for the same pull down maneuver at 8000m. All these limits are for the maximum take-off weight. It can also be noticed that the maximum bending moment is larger than the maximum torsional moment. It is because aircraft are more subject to bending than to torsion.

The cut loads times histories from Nastran gust loads analyses for the monitoring point CW640005 are shown in Figure 2.21. These are the results for the steady gust load case at the cruise condition (Mach 0.8 and 8000m), with a discrete 1-Cosine Gust according to the CS25. It can be seen that the most important loads applied at the sectional cut, and in general are the vertical forces and bending moments. The wing seems to be less affected by gust loads for the empty mass case. The magnitude is generally lower and it decreases faster for MOOee case than for the others.
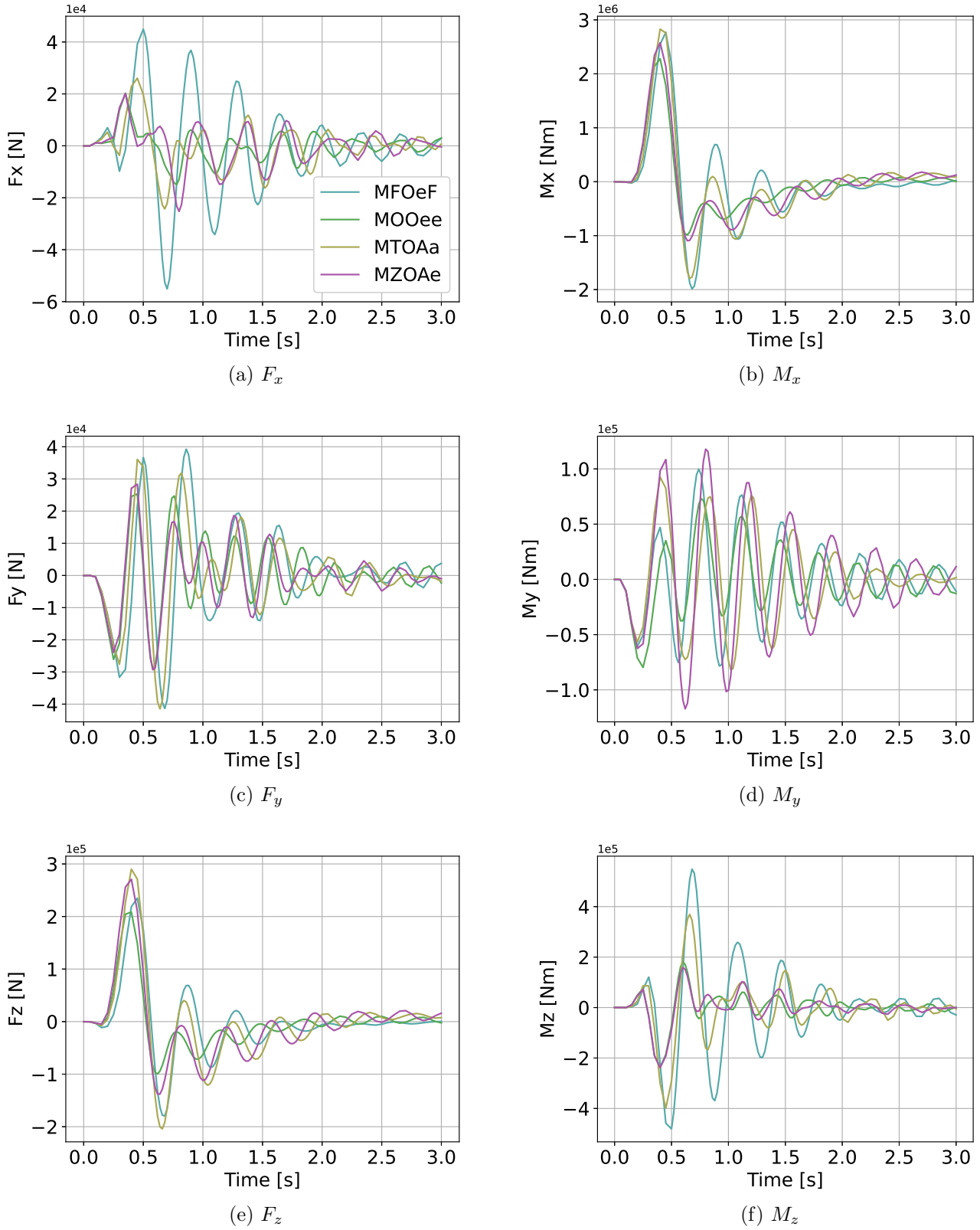
Figure 2.21: Cut loads (force and moment) times histories from Nastran gust loads analyses for the DLR-F25 baseline configuration at the monitoring point CW640005.

2.5.6 Flutter Characteristics

As said in Chapter 1.3, flutter is a self-excited vibration phenomenon caused by inertial, elastic and aerodynamic forces that can happen when the aircraft is flying. This phenomenon has to be avoid because it can cause a lot of structural damages. For low speed, the vibration is easily damped but it is very important to check if there is no flutter in the flight envelope for every mode of vibration. Figure 2.22 represents the aircraft vibratory frequencies for the first twelve elastic modes as a function of the true airspeed and Figure 2.23 represents the corresponding damping as a function of the true airspeed. Theses figures have been obtained for a Mach number of 0.6 at an altitude of 8000m and a 0° angle of attack.

(a) MFOeF

(b) MOOee

(c) MTOAa

(d) MZOAe
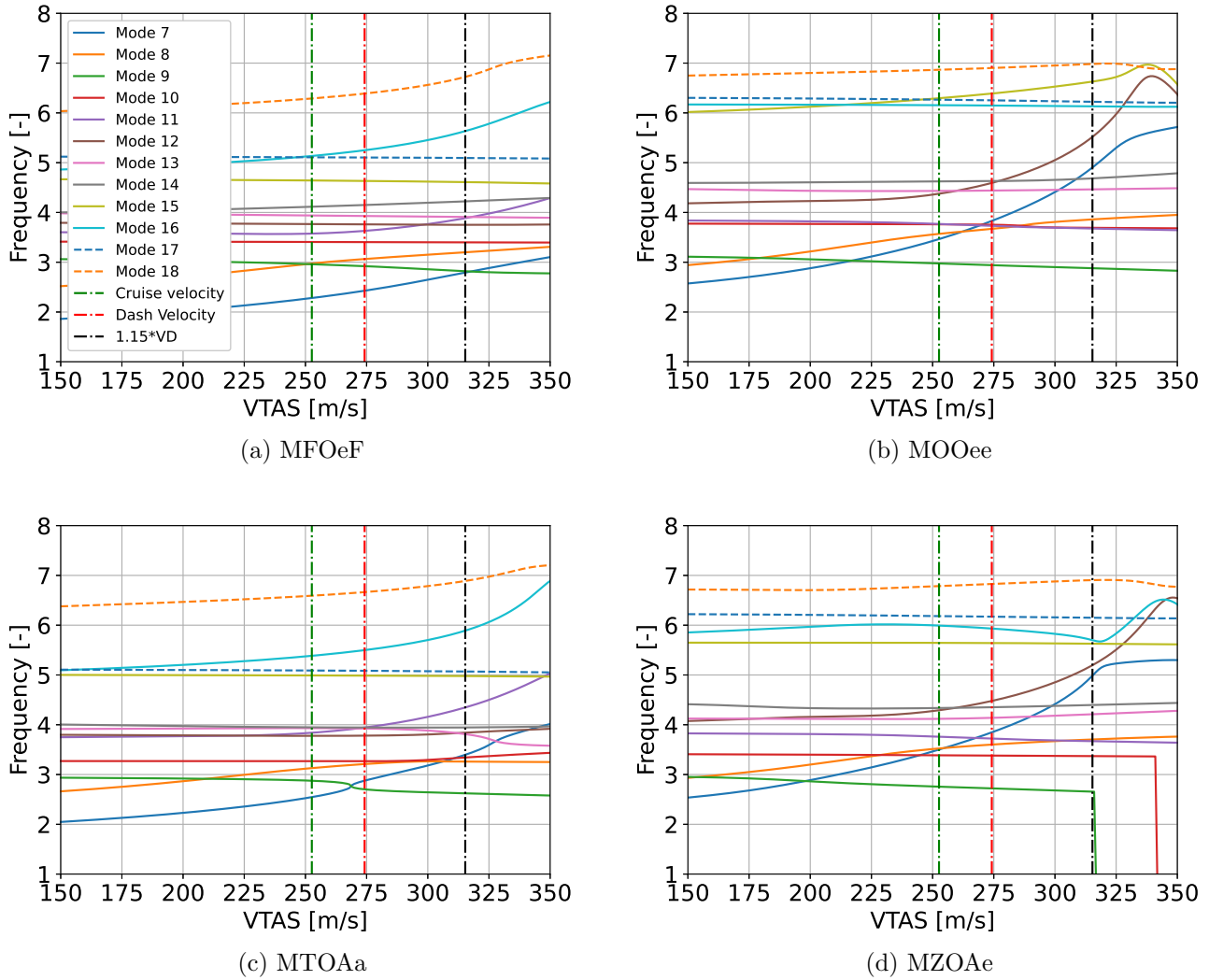
Figure 2.22: Frequency diagram as a function of the true airspeed for the DLR-F25 baseline configuration for different mass cases.
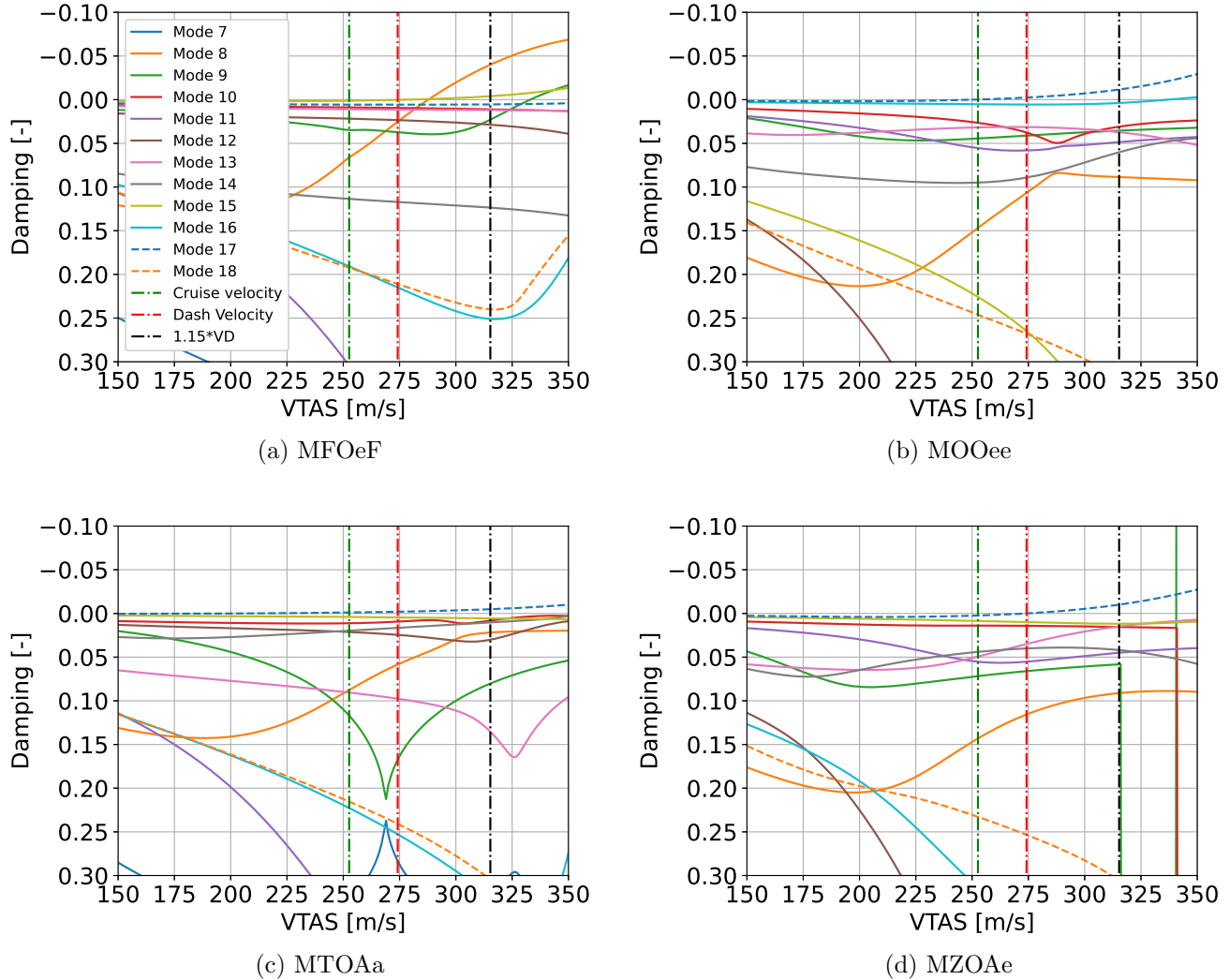
Figure 2.23: Damping diagrams a function of the true airspeed for the DLR-F25 baseline configuration for different mass cases.

To avoid flutter, the damping has to be positive. The objective is to keep a positive damping in the flight envelope. If flutter appears beyond dive speed (maximum velocity), there is no flutter issue. However, for the Certification Specifications CS25 [19], a safety margin of 15% is taken. Flutter cannot appear before a velocity of 1.15 VD.

It can be seen that for MFOeF case that the only flutter mode in the flight envelope is mode 15. For the other mass cases, there is flutter for mode 17. These modes are similar and corresponds to in-plane mode. Indeed, this mode shape can be seen in Figure 2.24. MSC Nastran is not able to generate drag. However, for in-plane mode, drag has the most important role in the structure damping. We can then consider that if flutter only appears for in-plane modes, there is no real issue and there is no flutter within flight envelope. In Figure 2.23, only the first twelve elastic modes are shown, however, flutter is checked for the first 50 modes in the flight envelope.

It can also be seen that for MFOeF case, mode 8 is a flutter mode for a velocity between VD and 1.15 VD. That is an issue for the certifications, however, because flutter is not a constraint in the cpacs-

MONA process, it is impossible to solve this issue. In the future version of cpacs-MONA, the flutter will be integrated as a constraint. One possible way to solve the problem is by adding some masses at certain points of the wing. This is not part of the work and need to be done in the future.
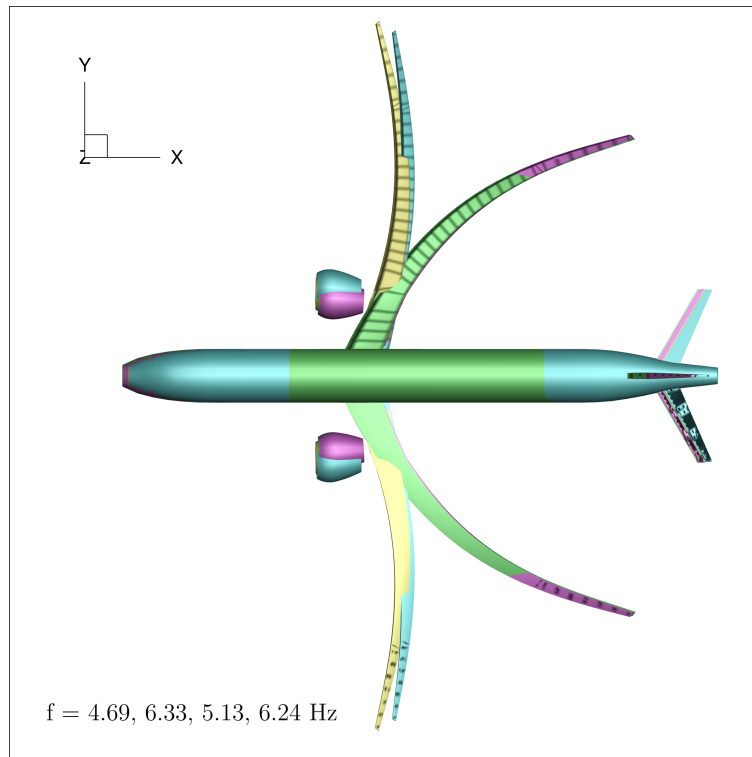
Figure 2.24: In-plane mode shape for different mass cases (MFOeF = blue, MOOee = green, MTOAa = yellow, MZOAe = purple). It corresponds to the mode 15 for MFOeF case and mode 17 for other cases.

Chapter 3

Extensions of cpacs-MONA for the Planform Modification of the DLR F25 and Improved Postprocessing

In this chapter, all the modifications implemented to extend cpacs-MONA process will be presented. First, methods to increase the aspect ratio will be described. Then, an automated process for the whole cpacs-MONA simulation, from the geometry modification to the post processing, will be explained. Some issues regarding the aerodynamic grid and the internal structure will be solved. The reliability of the results will be checked and a method to compute the Oswald factor will be implemented.

3.1 Modification of the Wing Geometry: Methods to increase the Aspect Ratio of the Wing

In this aspect ratio variation process, only the wing geometry has been modified, and only the outer part of the wing. The inner part remained the same and the engines kept their absolute location. However, it has been decided that the control surfaces will keep their relative coordinates in order to ensure the feasibility of maneuvers. Therefore, the control surfaces will be bigger.

To increase the wing aspect ratio, three different methods have been developed. For each method, the leading edge remains constant.

1. The first method consists on keeping the trailing edge lines constant and increasing the span from 44 to 49 m. The reference area will also increase but by less than 5 %. In general, increasing the wing surface by less than 5 % will not affect the flight conditions. The outer part modification is shown in Figure 3.1.
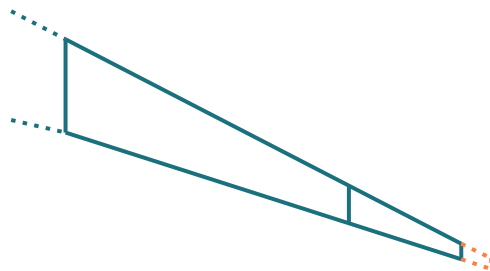
Figure 3.1: First method of aspect ratio variation - Span variation.

2. The second method consists on keeping the chord tip length constant and increasing the reference area from 0 to 5 %. The trailing edge sweep angle will increase, but very little, so it will not affect much the quarter chord sweep angle. The modification is represented in Figure 3.2.
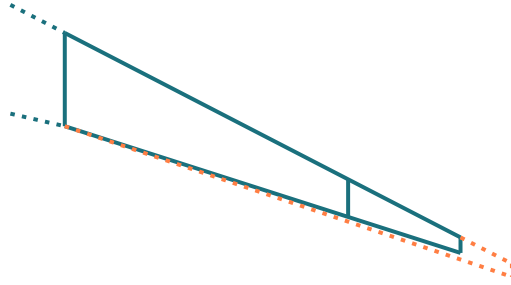
Figure 3.2: Second method of aspect ratio variation - Surface variation.

3. The third method consists of decreasing the tip chord length and keeping the reference area constant. The trailing edge sweep angle will decrease but still not sufficient to really affect quarter chord sweep angle. The modification is represented in Figure 3.3.
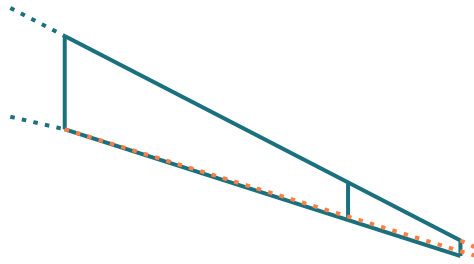
Figure 3.3: Third method of aspect ratio variation - Tip chord variation.

The modification is directly done within the CPACS file which is the only input needed by cpacs-MONA process. However, this modification is not so obvious to implement. Some coordinates, such as the coordinates of the leading edge, are absolute coordinates while others, such as the ribs, spars and control surfaces coordinates, are relative coordinates. Moreover, to modify the wing geometry, it is also required to adapt the internal structure of the wing, change the spars ending point, and also completely redefine the spacing and the location of the ribs. The DLR-F25 wing is defined on CPACS file by 5 sections (center, root, kink, mid and tip) as illustrated in Figure 2.2 and only the last two sections are modified.

3.2 A Python Framework for the Automated Execution of cpacs-MONA

A lot of different processes need to be automated, from the creation of folders and the CPACS file modification to the execution of cpacs-MONA and the post processing.

- It is important to easily find information in simulation folders, it is preferable to be consistent and precise in the folder and file names. This first step seems obvious but can really save a lot of time for the post processing. An automatising of this step is required.

- CPACS file needs a lot of different modifications on the wing, internal structure and geometry. Some references like MAC and wing surface also need to be computed and changed in the file. Doing manually the modification for each simulation is too expensive in time. A useful way to modify this

file has been implemented using TiXI package in python. This package has been developed by DLR
and is used to modify xml files [22].

- Knowing that only one complete simulation requires at least three hours and that a lot of simulation
  with different wing geometry modifications has to be done, it is too restrictive to manually launch
  the cpacs-MONA process after each simulation. A Python script to create folder, modify CPACS
  file and run simulations in a loop has been implemented to save time.

- The post processing part is the most important step of the full process. cpacs-MONA creates a lot
  of directories and files within MSC Nastran and ModGen, the main simulation folder contains more
  than 3 GB of data. A post processing routine has been implemented to extract from different files
  data about loads, aerodynamics, structure, flutter, ect. This allows to directly have a quick look at
  very important aircraft parameters, and also to determine if the simulation gives wrong results.

3.3   An improved Method for the Generation of the Aerodynamic Grid

The aerodynamic grid is automatically generated by ModGen and the only parameter that can be
modified within CPACS file is the number of panels in the chordwise direction. The panel length is
usually constant along the chord but sometimes adjusted for the control surfaces. One observed issue
is that when the pylon is not aligned with the aerodynamic grid in the chord direction, as shown in
Figure 3.4a, there is a peak in Δc_p at that aerodynamic panel in the pressure distribution. By increasing
the wing span, the aerodynamic grid automatically changes, and is not aligned anymore with the pylon.
This numerical issue proves that the generation of the grid by ModGen is not optimal and needs to be
improved. However, because it is not directly modifiable on the CPACS definition of the aerodynamic
grid, the MONA process needs to be decomposed in 3 steps:

- Run the simulation until the grid is totally generated by ModGen

- Stop the simulation and modify the ModGen definition of the grid in order to keep it aligned with
  the pylon

- Continue the simulation until the end of the whole process.

As it can be seen in Figure 3.4b, this new aerodynamic mesh really improves the results of the pressure
distribution on the wing. In the future, a new definition of the aerodynamic grid needs to be implemented
within CPACS file to be more practical and usable. Another improvement can be done on chordwise
direction. Indeed, the mesh should be more refined close to the leading and trailing edges. There is no
peaks in Δc_p anymore and the values of the distribution of Δc_p are coherent.

(a) Before adjustment

(b) After adjustment
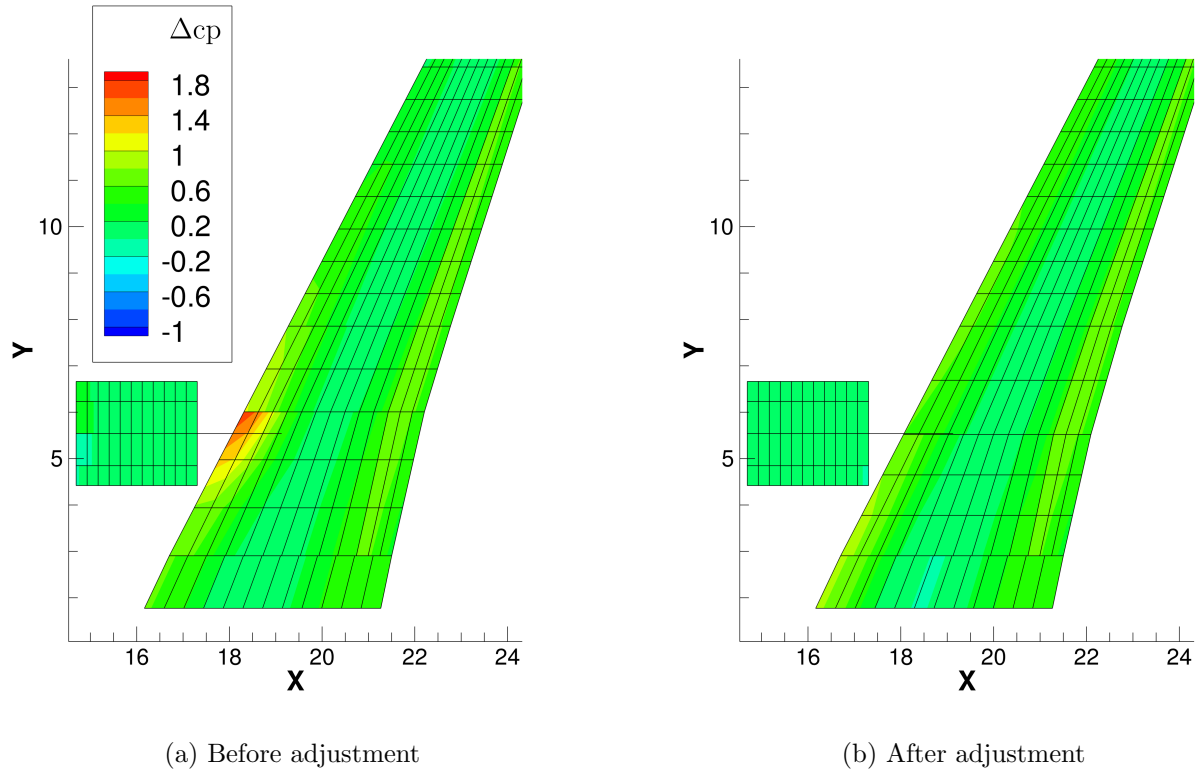
Figure 3.4: Δc_p distribution on the wing before and after mesh adjustment.

3.4 A Method for the Definition and Placement of Ribs in the Wing Structure.

For the baseline configuration, the ribs distribution was not optimal and not easy to modify. Each rib was defined one by one. To increase the wing's aspect ratio, additional ribs had to be introduced. However, other issues regarding the internal structure appeared because of the initial definition of ribs. The spacing and angle of the ribs were not consistent along the span. This disposition might cause some issues in the wing structure.

The new method of ribs has three steps and makes use of another definition for the ribs within the CPACS dataset:

- First, 5 ribs are defined parallel to the flow at the same position as the 5 sections (center, root, kink, mid, tip). It is very important because if these ribs are not defined, the cpacs-MONA simulation will fail.

- Then, ribs are defined between center and kink, still parallel to the flow.

- Finally, ribs are defined between kink and tip to be orthogonal to the front spar.

This is a typical ribs distribution for swept wings, similar to the distribution of the ribs in the wingbox of the Airbus A320 [23]. The ribs are located between front and rear spars and are approximately 70 cm apart. The objective is to keep a constant spacing between two ribs for a given wing segment (part of the wing between two sections) This ribs distribution is shown in Figure 3.5.
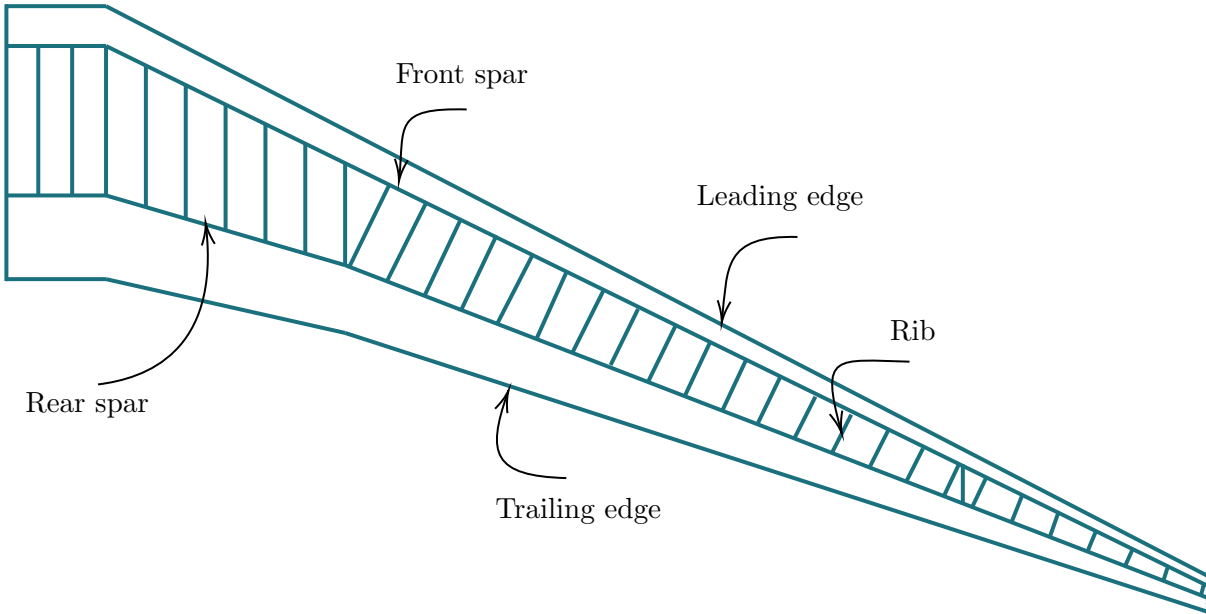
Figure 3.5: Ribs and spars definition.

3.5 A Method to Check for the Reliability of the Gust Loads Calculated by Nastran SOL 146

One of the most important parts is to check if the aerodynamic, structural and aeroelastic characteristics of the aircraft obtained with the cpacs-Mona process are reliable and can be used for detailed analyses. Three parameters can be checked: the pitch stability, the aileron efficiency and the gust loads.

Pitch stability and aileron efficiency must be positive. It is not so difficult to check because aileron efficiency is set as a constraint within the structural optimisation in cpacs-MONA and longitudinal stability can be determined by the stability margin equation already given in Chapter 2.5.2. A Python script has been implemented in the post processing routine to check both conditions. Fortunately, every aspect ratio variation simulation respects these two conditions.

The gust loads reliability must also be checked. The approach is based on empirical study done at DLR according to experience with MSC Nastran and requires the following condition:

$$\frac{G(0)}{max(|G(t)|)} < 1\%,$$

with $G(t)$ the gust loads response at time t. This condition has been applied for each gust force (F_x, F_y, F_z) and each gust moment (M_x, M_y, M_z). These gust loads are similar to those shown in Figure 2.21. The same kind of automatic process has been implemented and the condition is respected for every simulation. Each result obtained with cpacs-MONA can then be considered as reliable.

3.6 A Method for the Aerodynamic Performance Evaluation of the Wing

The goal of increasing the wing's aspect ratio is to reduce the vortices that leads to a reduction of the induced drag. The induced drag coefficient can be computed by the following equation:

$$C_{D,i} = \frac{C_L^2}{\pi \cdot e \cdot AR},$$

with CL the total wing lift coefficient, AR the aspect ratio and e the Oswald (or efficiency) factor. One of the MSC Nastran outputs is the lift coefficient along the span but the overall wing lift coefficient is not part of the results of the Nastran SOL 144 and has to be computed. C_L is the integral of the lift coefficient along the span by also taking into account the local chord length. It is expressed as:

$$C_L = \frac{1}{S} \int_{-b/2}^{b/2} cl(y) \cdot c(y) dy,$$

where S denotes the surface area of the wing, b the wing span, $cl(y)$ the local profile lift distribution and $c(y)$ the local chord length. To compute the Oswald factor, several methods can be used, like empirical approximations based on wing geometry. This approach is well explained by Nita and Scholz [24] from Hamburg University of Applied Sciences. However, the method used for this estimation is a numerical approximation directly based on the lift distribution as described by Anderson [25]. This method uses a Fourier sine series applied to the Prandtl's lifting line theory. Knowing the exact lift distribution along the span, the objective of this method is to approximate this distribution and determine the Oswald factor in order to compute the induced drag coefficient. Strating with the equation of the general circulation distribution as follows:

$$\Gamma(\theta) = 2 \cdot b \cdot V_\infty \cdot \sum_1^N A_n \sin n\theta,$$

where the A_n coefficients are unknowns. The circulation can also be expressed as:

$$\Gamma(\theta) = \frac{L'(\theta)}{\rho_\infty \cdot V_\infty}, \qquad \text{with} \quad y = \frac{b}{2} \cdot \cos \theta.$$

The first coefficient A_1 can be determined from the total wing lift coefficient and it represents the elliptical lift distribution:

$$A_1 = \frac{C_L}{\pi \cdot AR}.$$

Then, the following system of equations needs to be solved in order to find the other A_n coefficients:

$$L'(\theta) - A_1 \sin \theta = 2 \cdot b \cdot \rho_\infty \cdot V_\infty^2 \cdot \sum_2^N A_n \sin n\theta$$

In order to have good results with this method, the lift distribution obtained from the DLM need to be extend into the plane of symmetry of the aircraft. Indeed, the first point of measurement is at the root and need to be at the center. A good lift distribution approximation can be obtained by taking only three values of the lift coming from different monitoring points: one at the root (becoming the center), one in the middle of the wing and one at the tip. If the number of points used is the same as the number of monitoring points or just too large, the solution of the system will be too precise. As a consequence, the A_n coefficients will be too high and the Oswald coefficient will be too low. The results are not consistent with a large sample of monitoring points. To have a good approximation of the lift distribution, the real wing lift distribution needs to be extrapolated to the symmetry plane because there is no lift (pressure) output for the region between the symmetry plane and the beginning of the wing at the fuselage. Indeed, the MSC Nastran output of the lift distribution starts at the wing root which is a the fuselage and not at the symmetry plane. The real, approximated and elliptical lift distributions are shown in Figure 3.6 for the MOFeF case of the DLR-F25 baseline configuration.
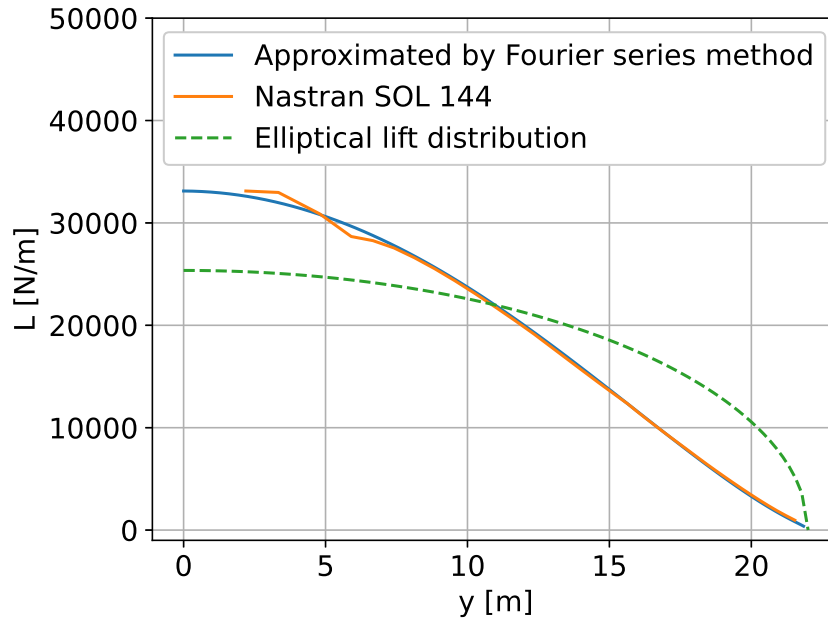
Figure 3.6: Lift distribution along the wing span for MFOeF case during cruise condition.

One can see that the approximated distribution with Fourier series gives very good results with only three A_n coefficients. The Oswald factor is obtained with [25]:

$$e = \frac{1}{1+\delta}, \qquad \text{with} \quad \delta = \sum_{n=2}^{N} n \left(\frac{A_n}{A_1}\right)^2.$$

The evolution of this factor with the aspect ratio is shown for each mass case and method in Figure 3.7. Because the twist distribution is not well adapted for the aspect ratio variation, for each mass case and each method, the Oswald factor decreases with the wing aspect ratio. Moreover, the trend is quite the same for all mass cases. It can also be noticed that the heavier the aircraft, the higher the Oswald factor. Indeed, the Oswald factor for the empty mass case is 6.5% lower than the one of the maximum take-off weight. Because the aspect ratio increases faster than the Oswald factor decreases, the induced drag coefficient decreases.

(a) MFOeF

(b) MOOee

(c) MTOAa

(d) MZOAe
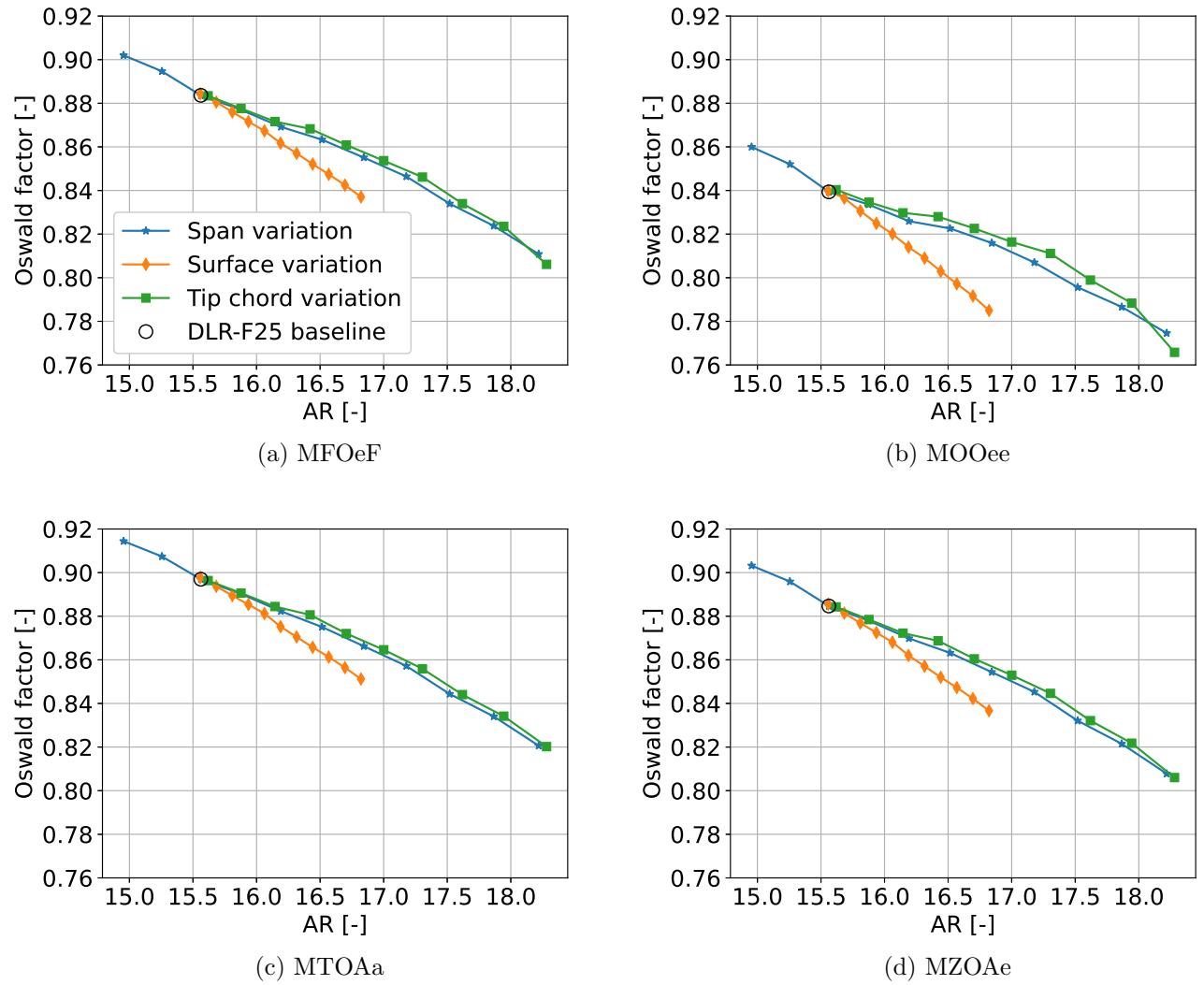
Figure 3.7: Evolution of Oswald factor for each mass case and aspect ratio variation method.

Chapter 4

Aspect Ratio Variations of the DLR F25

The objective of this chapter is the aspect ratio variation investigation on different aircraft characteristic. The complete process including the wing geometry modification, the simulation with cpacs-Mona and the post processing is described. The evolution of aerodynamic, structural and aeroelastic characteristics of the aircraft with the aspect ratio is presented and discussed. Finally, a discussion regarding the relevancy of the different methods is done.

4.1 Description of the Complete Process

The complete process of aspect ratio variation is composed of 3 main steps: the wing geometry modification within the CPACS dataset, the complete cpacs-MONA simulation and the post processing of the results. The first and last steps are already explained in Chapter 3.

The second step is also composed of 3 steps: the initialisation based on conceptual design results, the convergence of the results based on numerical simulations and the computation of aircraft's aerodynamic, aeroelastic and structural characteristics

- At first, a fast estimation of conceptual design loads of the rigid aircraft is done. Theses loads are defined as Nastran cards containing forces and moments for wing, tail planes, fuselage and all the other aircraft components. Then, the stiffness of the generic fuselage is calculated and the loads are used for the sizing (wing mass, skin, stringer, ...). After that, ModGen is used to create the parametric model, aerodynamic and structural mesh. Finally, the mass model is estimated and the load cases are set up.

- In the second part of the cpacs-MONA process, the iterative process starts with the extraction of the stiffness model and the analysis of loads for flexible aircraft with MSC Nastran. Then, the gust loads are computed and the load cases are selected and evaluated. When all these steps are finished, the mass model is updated and this loop is repeated until the convergence of the masses and loads. In general, it takes 3 to 4 iterations to converge.

- The last steps of the process is composed of 3 steps: the sensitivity analysis, the extraction of modal parameters and the flutter check. The sensitivity analysis is used to find out how changes in variables and parameters affect the performance and feasibility of the aircraft concept. Modal parameters are useful to know the vibration frequencies as well as the corresponding mode shapes, and check if everything looks fine. It is also very important to check if there is a flutter phenomenon in the flight envelope.

The whole simulation process is repeated for many different wing geometry and different aspect ratios. Simulations without gust and with Pratt gust computation have also been done to compare the impact of the gust loads on the results.

4.1.1 Aspect Ratio limits

The aspect ratio of the DLR-F25 baseline configuration is 15.6 that is around 50% more than similar commercial aircraft like the Airbus A320. The initial objective was to increase the aspect ratio until 20, that means increasing by 33%. This was a very high increase and was only feasible with the initial wing by modifying the outer part of the wing. To reach this aspect ratio, a completely new wing has to be designed and this is not the objective of the thesis. The highest possible aspect ratio for this study is 18.3 which is 17.5% higher than the baseline aspect ratio.

Sometimes, even if numerical analysis gives interesting results and seems to be feasible, there are physical and manufacture constraints. For the baseline configuration, the tip chord is already very thin and narrow, a lot more than usual transport aircraft. The DLR-F25 has a tip chord of 0.6 meter while the Airbus A320 tip chord is 1.5 meter. The taper ratio is also half the Airbus one. It is quite difficult to manufacture such a narrow wingbox.

For the aspect ratio of 18.3, the tip chord is 0.15. cpacs-MONA was not able to complete simulations with a smaller wing tip chord, this is the numerical limit. Moreover, the wingbox at the tip cannot be defined as a monocoque wingbox within the CPACS dataset which probably could have solved this issue. A monocoque wingbox is wing structure where the skin provides strength and support, therefore, no other internal structure is needed. This wingbox reduces the wing weight and improve its structural integrity. Another issue of having such a narrow tip chord is for the aileron mechanism. It is why there is a manufacturing limit of the tip chord length.

Results are obtained for aspect ratios from 15 to 18.3, however, the physical and manufacturing limits still exist and the results have to be analysed from a critical point of view.

4.1.2 Pratt and Nastran Gust Loads

Three different approaches can be used to estimate the gust loads: quasi-static, transient or continuous approach. The Pratt gust method is based on a quasi-static approach and is usually used for aircraft preliminary design [26]. This method developed by Pratt and Walker gives a lower fidelity and cost than other ones because gust is a transient phenomenon. The normalized gust profile equation is given by:

$$\frac{U}{U_0} = \frac{1}{2}\left(1 - \cos\frac{2\cdot\pi\cdot s}{25}\right) \qquad \text{with} \quad s = \frac{t\cdot V_\infty}{\bar{c}},$$

where $\frac{U}{U_0}$ is the gust intensity, s is the dimensionless time, t is the time, V_∞ is the airspeed and $\bar{c}$ is the mean aerodynamic chord. The gust length is based on empirical data and is assumed to be 25 chords which corresponds to the critical response of an aircraft [27].

The second method to compute the gust loads is with Nastran SOL146, the dynamic aeroelastic solution sequence designed for the dynamic aeroelastic analysis in the frequency domain. This solution is already defined in Chapter 1.4

In order to compare the results obtained by using Pratt gust loads constraints, Nastran SOL146 gust loads constraints and no gust loads constraint, all the aspect ratio variation simulations have been completed for each cases. The results obtained with Pratt gust loads and Nastran SOL146 can be compared as shown in Figure 4.1. The results show in Figure 4.1 are obtained for the span variation method and the MFOeF case. However, simulations have been done for each method and mass case. The difference between both approaches (with Pratt and Nastran gust) are similar for each simulation. The results will be analysed later but what is interesting here is the difference between gust loads definition. All the results plotted in Figure 4.1 are obtained for a fully optimised model but with different methods to take

gust loads into account. Figure 4.1a shows the x coordinate of the aircraft's center of gravity as a function of the aspect ratio and the results without gust loads constraint, with Pratt gust and Nastran gust loads constraints are exactly the same. This is why only one curve can be seen. This is not the case for the x coordinate of the aircraft's aerodynamic center and for the aircraft stability margin as a function of the aspect ratio as shown in Figures 4.1b and 4.1c, respectively. The stability margin is a little lower with Pratt and the aerodynamic center is more forward. Regarding the evolution of the mass of the aircraft shown in Figure 4.1d, the results obtained using Pratt gust definition are much larger.
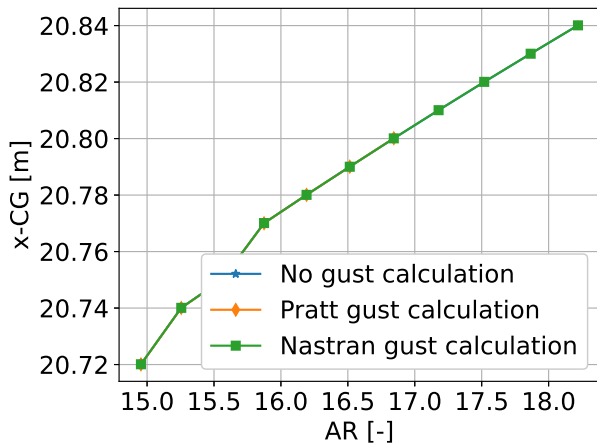
(a) x-coordinate of the center of gravity
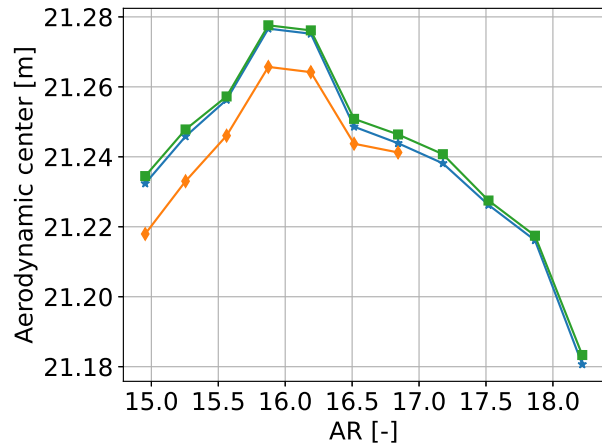
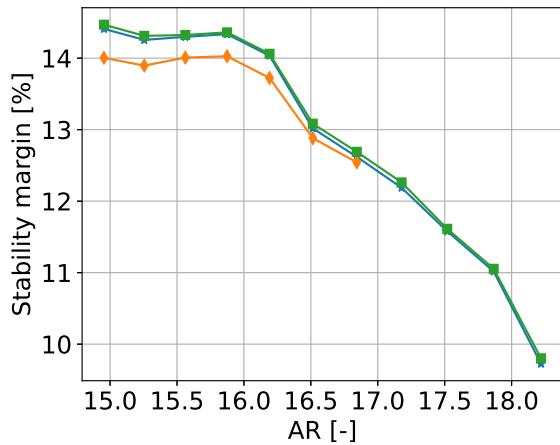(b) x-coordinate of the aerodynamic center

(c) Aircraft stability margin
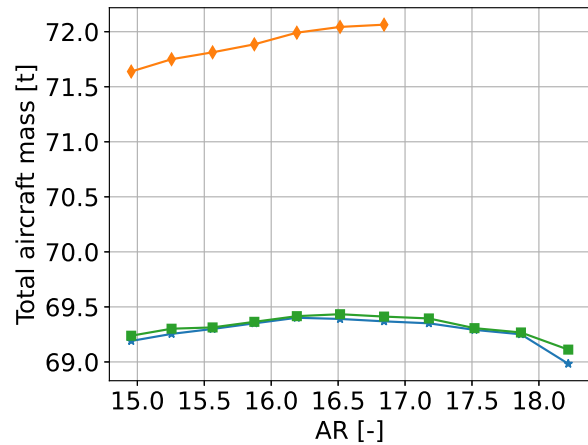
(d) Total aircraft mass

Figure 4.1: Variation of different quantities of interest as a function of the aspect ratio for simulations without gust loads constraint (blue), with Pratt gust (orange) and Nastran SOL146 gust loads constraints (green). The method shown is the span variation and the mass case is MFOeF.

One important thing to notice is that for the last four simulations using Pratt gust loads, cpacs-MONA did not converge at all, this is why there are less results. For this configuration, even if simulations are faster with Pratt gust than with Nastran SOL146, results are not consistent. This difference between Pratt and Nastran gust methods also appears for other mass cases and aspect ratio variation methods. The case without any gust loads constraint gives results very close to the ones obtained with dynamic gust and are even faster than simulations using Pratt gust loads. However, gust is an important phenomenon that needs to be taken into account. Nastran solution 146 will be used for the rest of the aspect variation

computations.

4.2   Impact of the modified Aspect Ratio of the Wing

Various different quantities of interest are discussed in this section. Aspect ratio variations impact aircraft stability, aerodynamic and structural properties as well as aeroelasticity. Each aspect ratio variation is done for the 4 different mass cases and 3 aspect ratio variation methods.

4.2.1   Impact on the Aircraft Center of Gravity and Mass

For each aspect ratio variation method, the span is extended. Because the wing is swept, it is expected for the aircraft's center of gravity to move backward but only by a small amount because the wing is not the heaviest part of the aircraft and also, engines do not move. Figure 4.2 shows the x coordinate of the center of gravity as a function of the aspect ratio for each mass cases and method.

(a) MFOeF

(b) MOOee

(c) MTOAa

(d) MZOAe
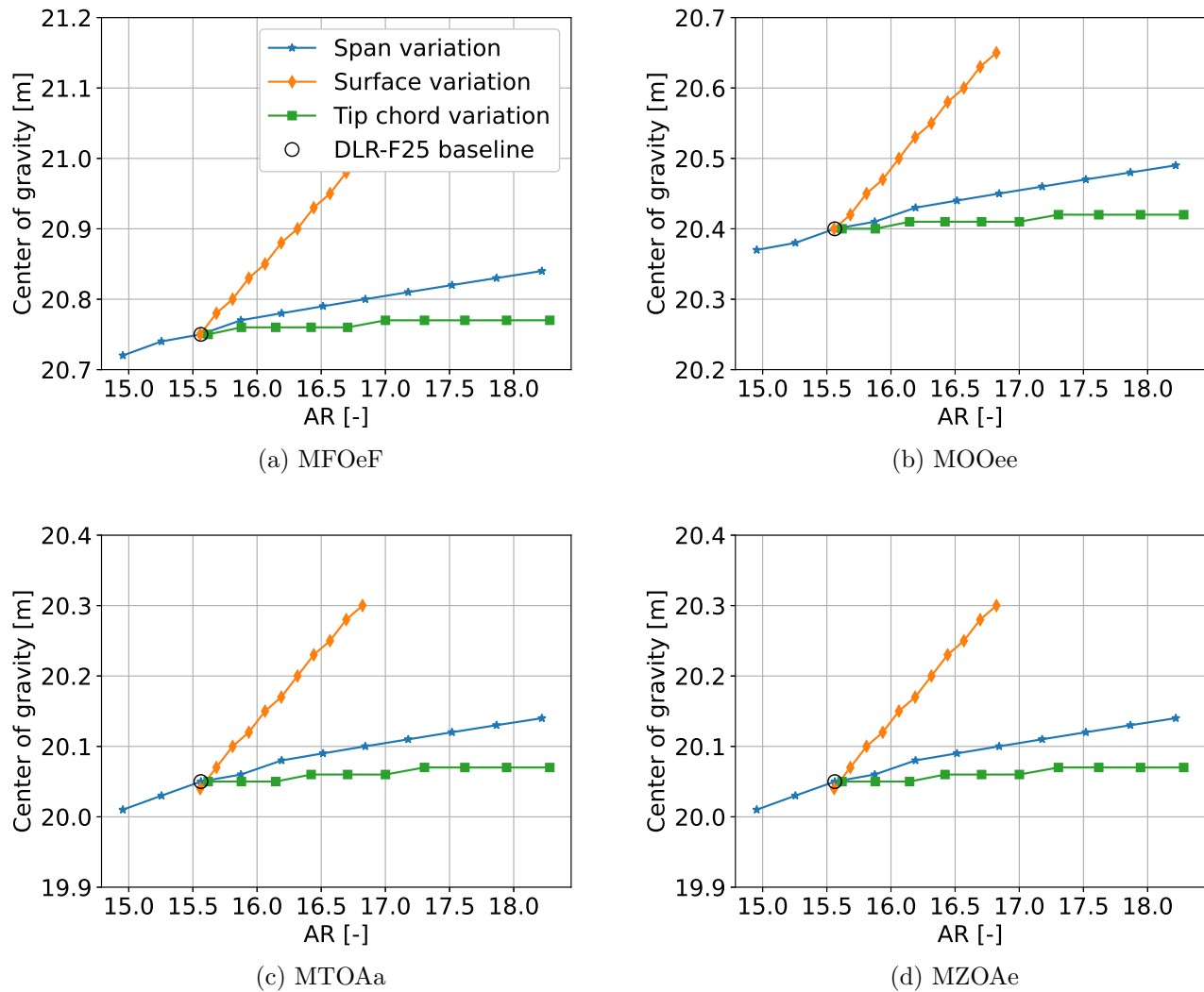
Figure 4.2: Variation of the aircraft's center of gravity as a function of the aspect ratio for different mass cases and methods.

As expected, the center of gravity moves backward for each mass case and method. This center is more in the front of the aircraft for the mass cases with the maximum payload, i.e. for MTOAa and MZOAe. It can also be noticed that the results are exactly the same for these mass cases. This comes from the fact that the target center of gravity defined in CPACS data set is the same for both cases and during the simulation, payload moves in order to keep the same fuselage center of gravity. The variation of the aircraft's center of gravity comes from the wing geometry modification.

The trend is the same for each mass case and even the value of the variation is the same. This proves that only the wing center of gravity has an impact on this variation. It can also be observed that the center of gravity displacement is higher for surface variation than for span and tip chord variation methods. This is not very surprising. Indeed, for the surface variation method, the tip chord is constant and the reference area increases by 5% which means that the trailing edge sweep angle has to increase that causes the center of gravity to move even more backward. The span variation method keeps the same sweep angle and the reference area only increases by 2%. For the tip chord variation, the reference area is constant and the center of gravity does not move that much. The main source of this variation is the surface increase.
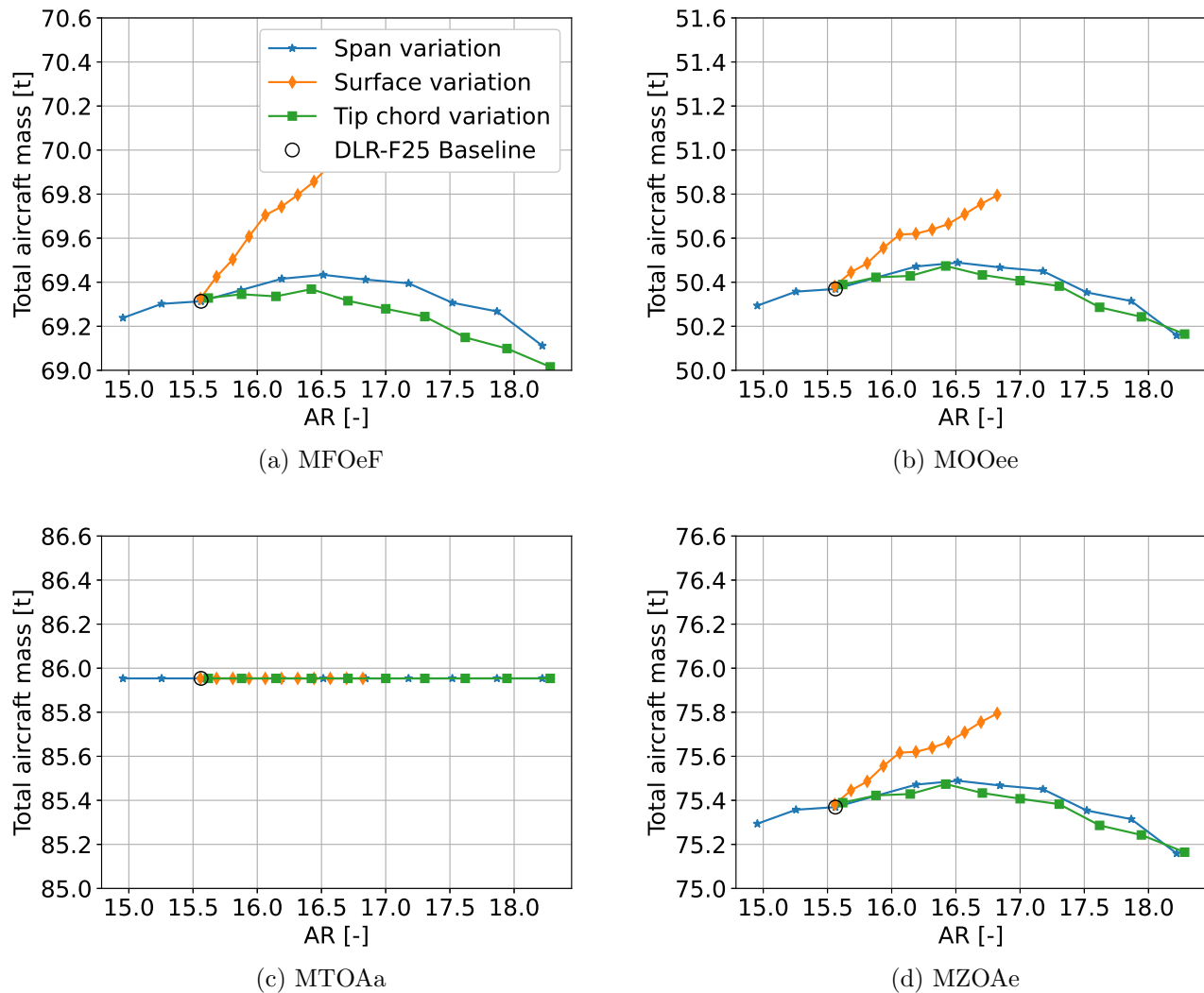

(a) MFOeF

(b) MOOee

(c) MTOAa

(d) MZOAe

Figure 4.3: Total aircraft mass as a function of the aspect ratio for different mass cases and methods.

Another interesting point is to know how much does the aspect ratio impact the total aircraft mass. Normally, the mass should increase with the aspect ratio because the longer the wing, the larger the bending deformation. This also means that a thicker wing skin is required which increases the mass. This mass variation is represented in Figure 4.3.

Starting with Figure 4.3c that shows the mass variation for the maximum take-off weight, the mass is constant with the aspect ratio. Indeed, this is a target mass and cannot be exceeded, this is a particular case that does not need analysis.

For the other mass cases, the trend is similar. For the surface variation method, as expected, the aircraft mass increases with the aspect ratio. Obviously, the larger the surface, the more material needed and the heavier the wing.

The other curves are quite interesting and not easy to understand and interpret. First, the behaviour of both methods is similar: the mass starts by increasing and beyond an aspect ratio around 16.5, the mass decreases. This can be explained by the fact that load alleviations are used by the optimiser to create a negative lift at the outboard section of the wing which significantly reduces bending loads. This reduction allows to reduce the wing stiffness and then save material and mass. It can be compared to Prandtl wing [28] which is a classical example of optimal wing design if the span is not a constraint. It has both good aerodynamic performance and low weight because the bending moment at the wing tip is reduced. However, to generate the same total lift, more lift will be on the inboard of the wing and the lift distribution will be further to the elliptical lift distribution.

One other thing that can be observed is that for both no fuel mass cases, the blue and green curves are very close and for the maximum fuel case, there is a certain gap between these curves. A higher wing reference area also means more space to put fuel. This is why the span variation method has a higher mass for MFOeF case.

The last interesting point regarding these figures (excepted the MTOAa case that keep the exact same mass) is that the mass variation is very low in general. The maximum max variation is around 600 kg for the surface variation method and 400 kg for the tip chord variation. This represents 0.6 - 0.9 % of the total aircraft mass. The impact of the aspect ratio variation on the aircraft mass is very little and can almost be neglected.

4.2.2   Impact on the Structural Properties

The wing is not a rigid but a flexible structure. Indeed, by generating some lift all along the span, it is subject to bending and torsion deformations. These deformations modify the aerodynamic properties of the aircraft. The direction of the lift is not only vertical because of the bending. A rigid wing will naturally generate more lift than an elastic wing during flight but unfortunately, the wing is not rigid. Figure 4.4 shows the maximum wing bending deformation (at the tip) as a function of the aspect ratio for different mass cases and different methods.

Figure 4.4: Wing maximum bending deformation as a function of the aspect ratio for different mass cases and methods.

These results are obtained on cruise condition which is an interesting flight condition to analysis the aircraft aerodynamic and structural characteristics. It can be seen that the heavier the aircraft, the more bending deformation and also the larger the slope. For the surface variation method and the empty mass case as well as the MFOeF case, the slope is negative which means the displacement at the tip becomes smaller. By increasing the wing area, the wing becomes heavier that increases the stiffness and reduces the displacement. Even if the wing becomes longer, it does not balance the stiffness increase. For the heaviest case, more lift is required and the gain in stiffness is balanced by the gain in span length. The slope of the curve becomes zero and the tip displacement stays constant with the aspect ratio increase.

The same reasoning can be used for the two other aspect ratio variation methods. For the lightest case, the wing tip displacement stays almost constant for both methods. The tip chord variation method gives results a little higher because the wing surface is constant in comparison with the span variation method. The stiffness is then more important for the last method mentioned and the tip bending is reduced.

The largest bending deformation is observed for the tip chord variation method for the maximum take-off weight and its value is 1.8 m. It only represents 7% of the half span. In general, if the deflection at the wing tip is higher than 10-15% of the half span, it is considered as large deformation [29]. This is not the case here, it is considered as reasonable.

The twist deformation can also affect the lift distribution along the wing. It changes the airfoil angle of attack and the lift generated by the wing. It is important to check if the maximum value of the torsional deformation is still reasonable. Figure 4.5 shows the maximum negative value of the torsional deformation as a function of the wing aspect ratio for each mass cases and method.
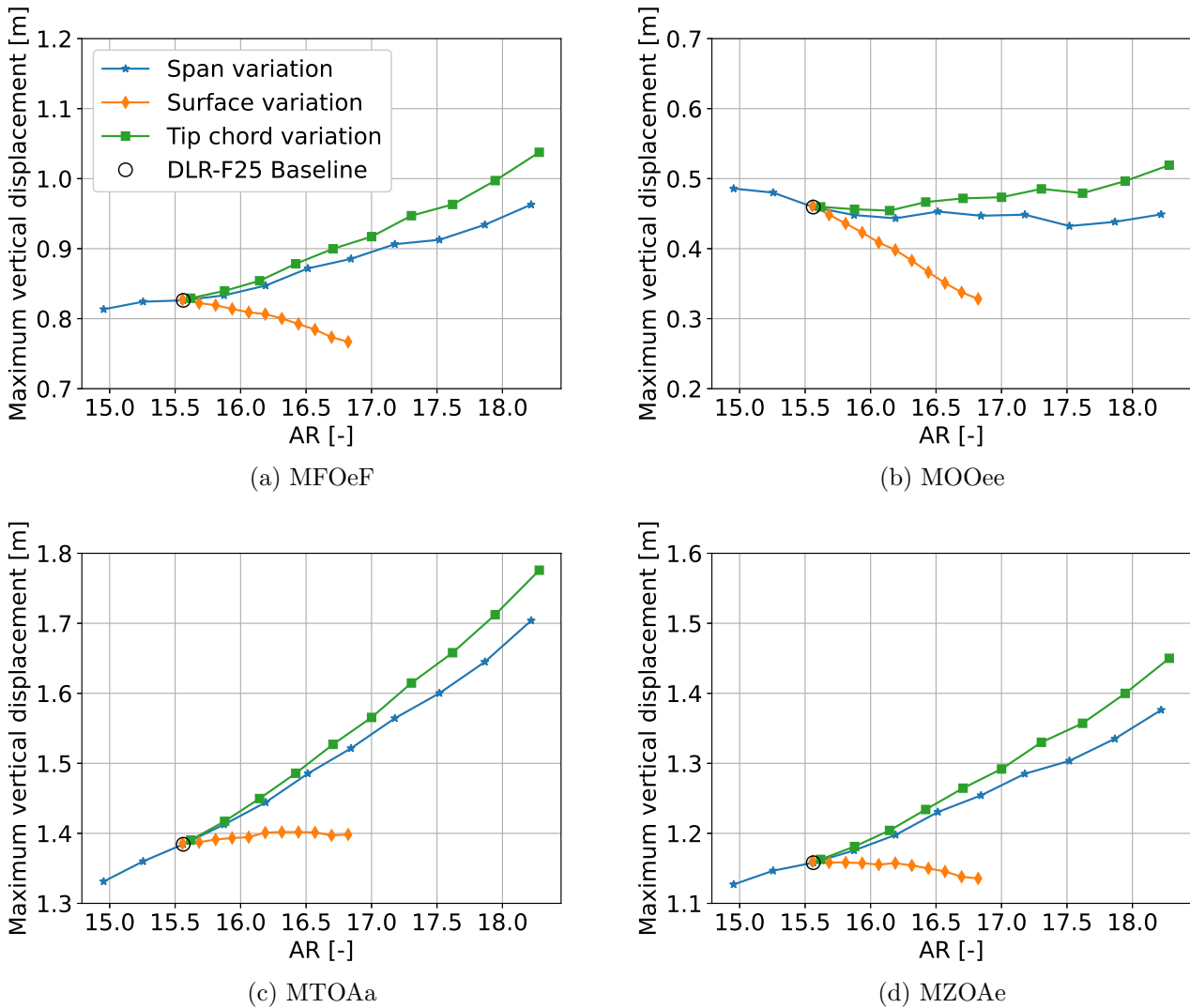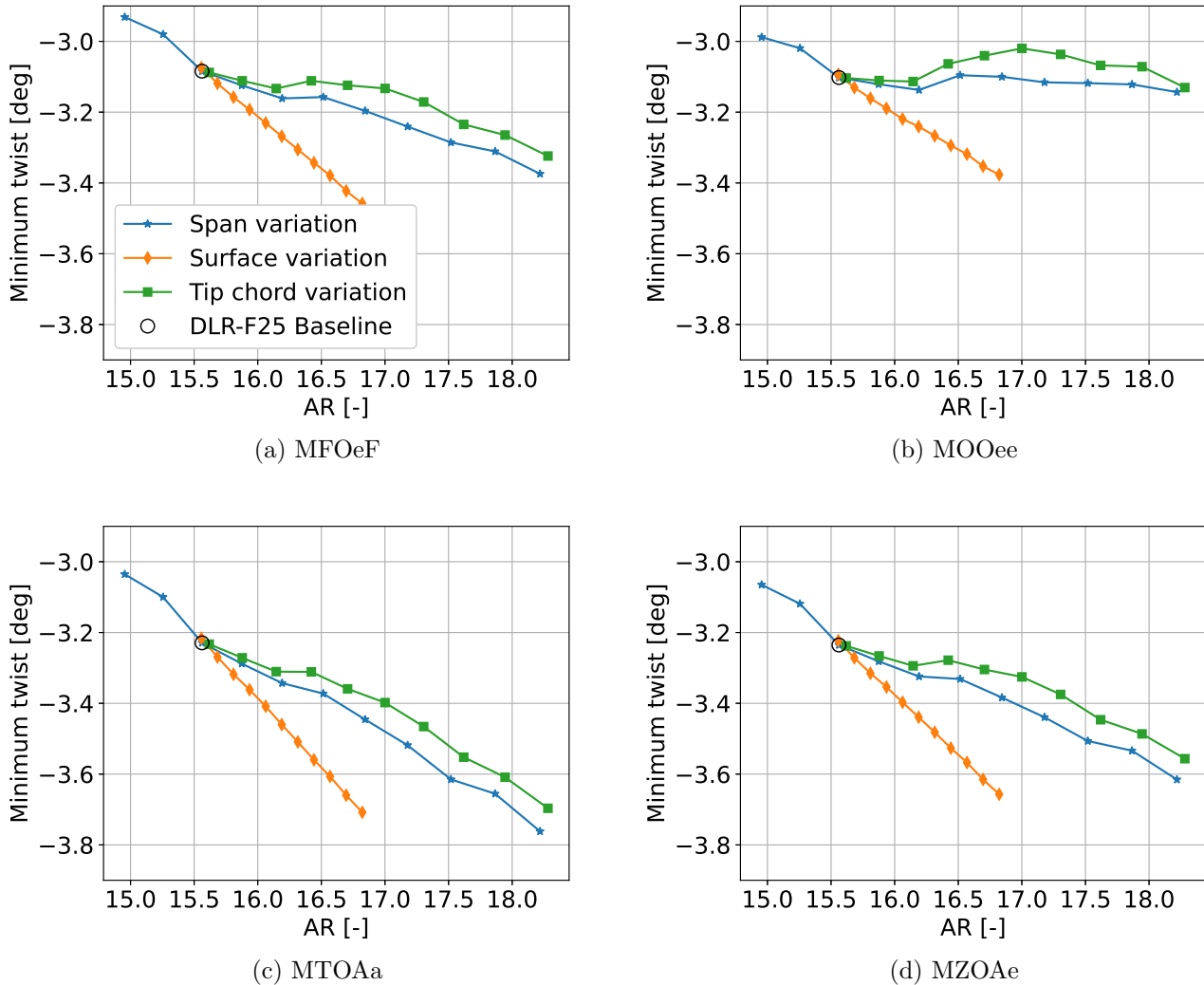

Figure 4.5: Wing maximum twist deformation as a function of the aspect ratio for different mass cases and methods.

First, the same observation than for the bending deformation can be done: the heavier the aircraft, the larger the negative slope of the twist. There are two reason that can explain this negative twist deformation. The first reason is that the geometric bending-twist are coupled which means that for a swept wing subject to bending, negative twist is created. The second reason is that the airfoil aerodynamic center is in front of the center of pressure. This induces a pitching moment that gives a negative angle to the airfoil. The more lift, the more pitching moment.

It can also be seen that the slope is larger for the surface variation method. It can be explained by the fact that for this method, the tip chord is constant while for other methods, it decreases. The relative distance between the airfoil aerodynamic center and the center of pressure is almost constant for each method, however, the absolute distance is higher for the surface variation method. So the lever arm is also higher. Once again, this induces a larger pitching moment, this is why the slope is larger for the surface variation.

Some results regarding the torsional deformation distribution are very surprising close to the tip but only for span and tip chord variations. Figure 4.6 shows the twist distributions near the wing tip for both aspect ratio variation methods, different aspect ratios and for the empty mass case.

(a) Span variation   (b) Tip chord variation
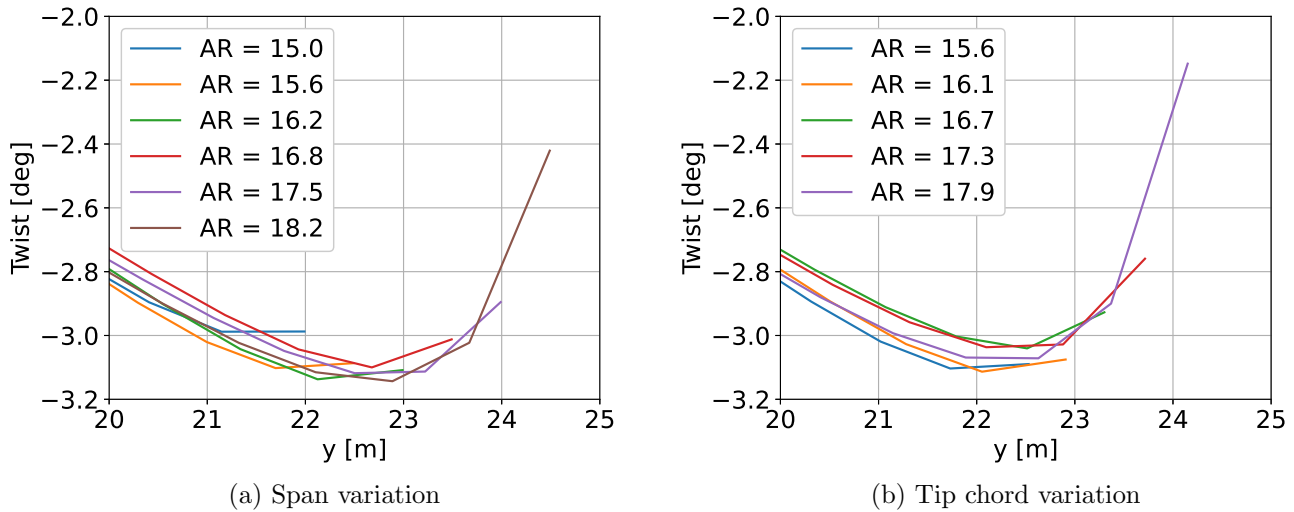
Figure 4.6: Twist deformation along the wing span for the first and third methods and the empty mass case.

It can be seen in both figures that for aspect ratio beyond 16.5, the maximum absolute value of the twist deformation is not located at the wing tip. Figure 4.7 shows the loads applied on the wing near the tip for the highest aspect ratio of the span variation method. Both the vertical forces and bending moments look good, there is no discontinuities and the loads are correctly applied on the simulation model. The torsional deformation obtained at the tip is a surprising behaviour that cannot be explained by simulation issues but more by physics of the material. For aspect ratio beyond 16.5, the wing tip chord is less than 40 centimeters and the thickness is less than 4 centimeters. This is very narrow and thin, the torsional stiffness at this location is very low and because there is a negative lift at the wing tip, the pitching moment direction is inverted. This causes such behaviour.

(a) Vertical Force   (b) Rolling moment

Figure 4.7: Vertical force and rolling moment applied along the wing near the tip for the span variation, aspect ratio = 18.2.

One solution would be to use a monocoque wingbox at the tip to increase the stiffness and avoid this issue. However, this kind of monocoque is not implemented yet in cpacs -MONA and the problem cannot be solved at the moment.
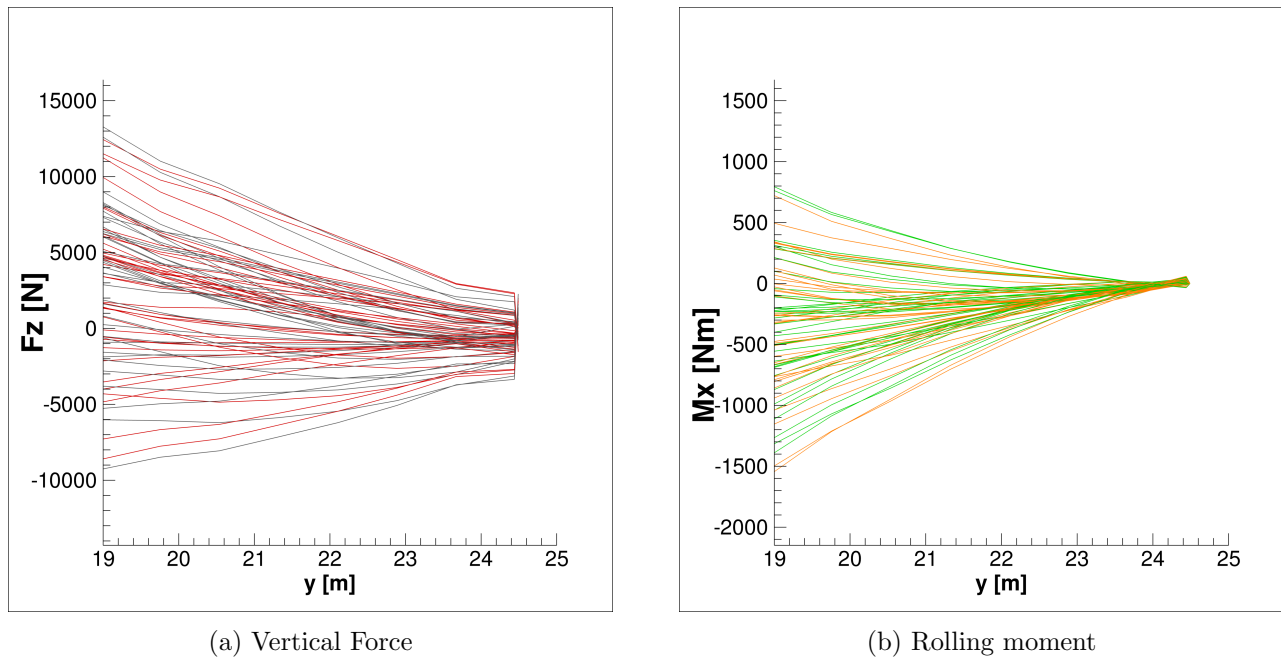
4.2.3   Impact on the Modal Properties

Increasing the wing aspect ratio should affect the aircraft stiffness. This could cause changes in the modal properties like eigenfrequencies or mode shapes. The most basic formulation of the natural frequency is the following:

$$\omega_n = \sqrt{\frac{k}{m}},$$

where k is the stiffness and m is the mass of the system. For the same wing area and lift distribution, increasing the aspect ratio will reduce the cross section and then probably reduce the stiffness. However, the stiffness distribution of the wing along the span is an outcome of the structural optimisation, it is therefore not that trivial. On the other hand, the mass is also supposed to increase. It is expected for the natural frequencies to decrease with aspect ratio. This formula is only used to understand how natural frequencies change with stiffness and mass, to have a global idea. This formula concerns a simple system of 1 mass and 1 spring. For a real aircraft, there is a large amount of nodes, so the structural stiffness and mass matrices are used and the behaviour of the frequency variation becomes more difficult to predict. Figure 4.8 shows the natural aircraft frequencies as a function of the aspect ratio for each mass case and the span variation method.

(a) MFOeF

(b) MOOee

(c) MTOAa

(d) MZOAe
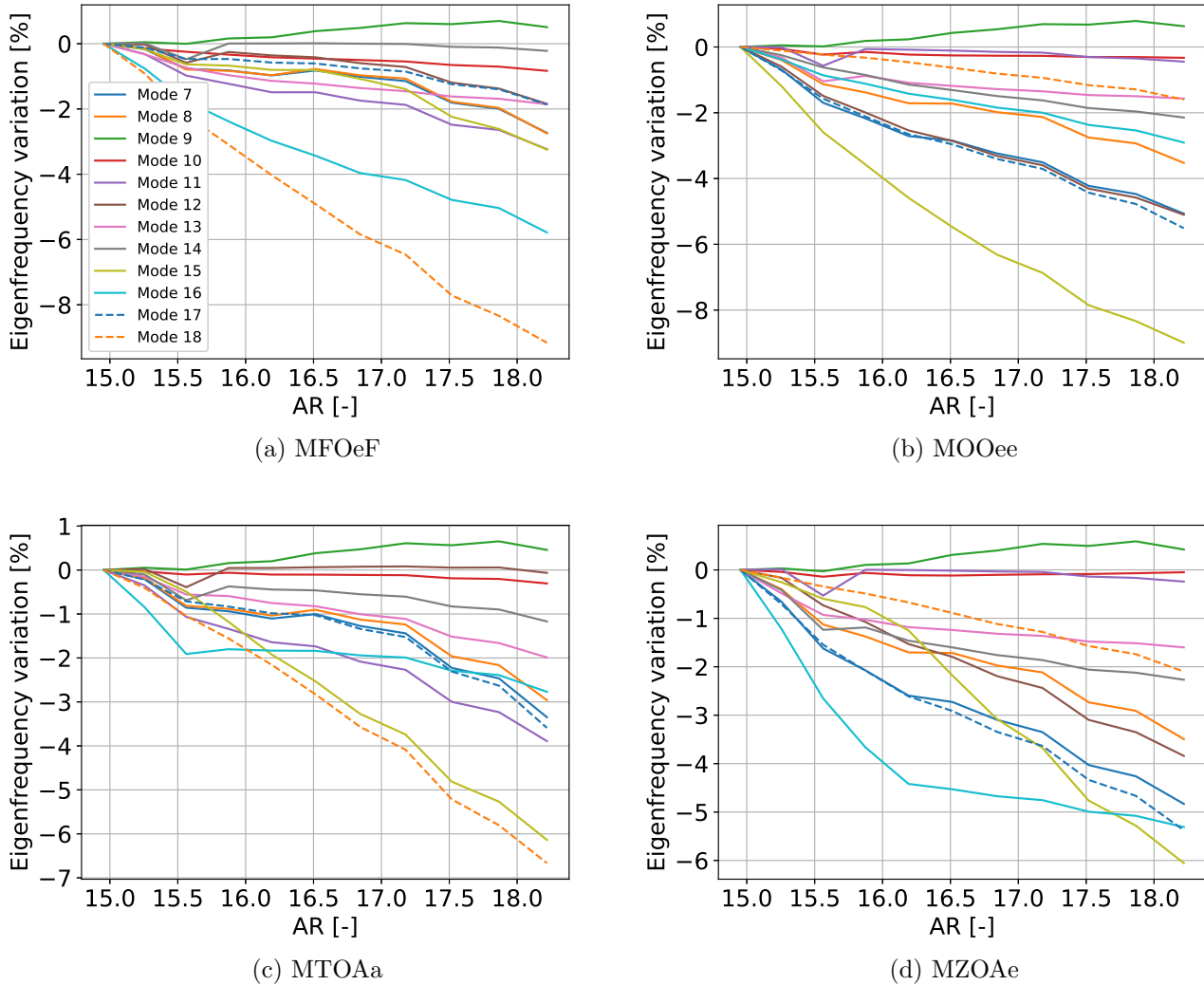
Figure 4.8: Variation of the aircraft modal frequencies as a function of the aspect ratio for different mass cases and for the span variation method.

As expected, the global behaviour of the eigenfrequency variation is decreasing. This is the case for every mode excepted mode 9. Frequency increases with aspect ratio but not that much. However, for the whole aircraft, stiffness and mass matrices are very large and it is difficult to precisely quantify how much does the evolution of stiffness matrix and mass matrix influences the natural frequencies. It can also be seen that the variation of frequency is larger for lighter mass cases.

4.2.4 Impact on the Aircraft Longitudinal Stability

It is essential to check if the aircraft is still stable even with an aspect ratio increasing. As explained in Chapter 2.5.2, an aircraft is longitudinally stable if its stability margin is positive. Figure 4.9 shows the evolution of the aerodynamic center with the aspect ratio for different mass cases and methods. It is expected that the aerodynamic center moves backward like the center of gravity because the wing is swept and extending the span will also move the mean aerodynamic chord to the tip which means backward.
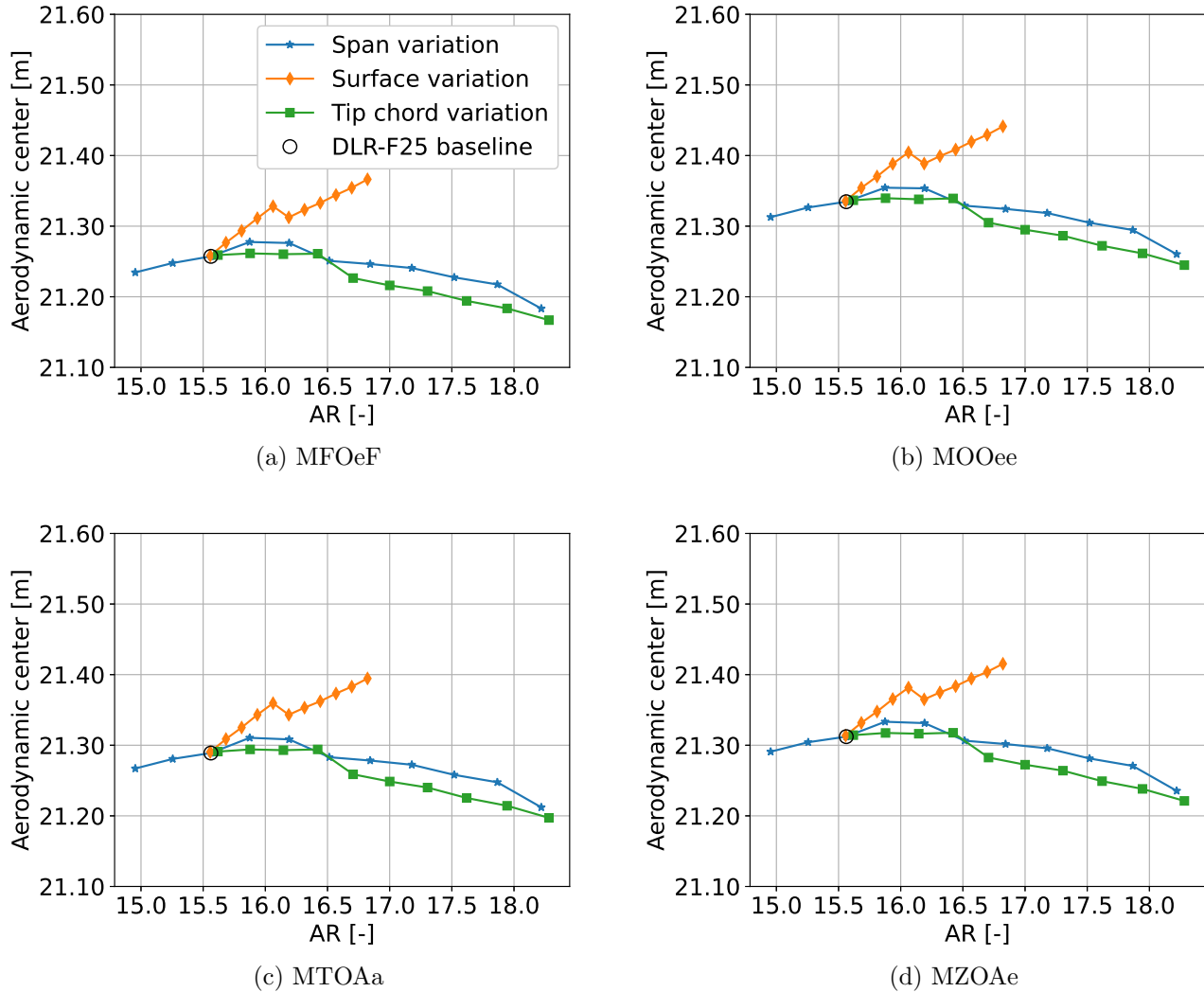
(a) MFOeF

(b) MOOee

(c) MTOAa

(d) MZOAe

Figure 4.9: Variation of the x-coordinate of the aircraft's aerodynamic center as a function of the aspect ratio for different mass cases and methods.

First it can be seen that the aerodynamic center is more backward in the empty mass case and more forward in the maximum fuel mass case. As expected, for the surface variation method, the aerodynamic center moves backward with the aspect ratio. However, there is a jump in the results between the aspect ratio of 16.05 and 16.2. The only explanation is a modification in the aerodynamic grid as it can be seen in figure 4.10. The pressure coefficient difference distributions are very similar between both figures. However, the aerodynamic grids are a little different especially at the trailing edge as shown by the red circles. The number of meshes in the chordwise direction is higher in Figure 4.10b. This mesh distribution is automatically generated by ModGen and cannot be easily changed. Some deeper investigations on the ModGen definition of the grid need to be done in the future.

Regarding the green and blue curves, the trend is very similar to the one obtained for the mass variation. At first, the aerodynamic center moves backward and then, beyond an aspect ratio of 16.2, moves forward.

(a) AR = 16.05

(b) AR = 16.2
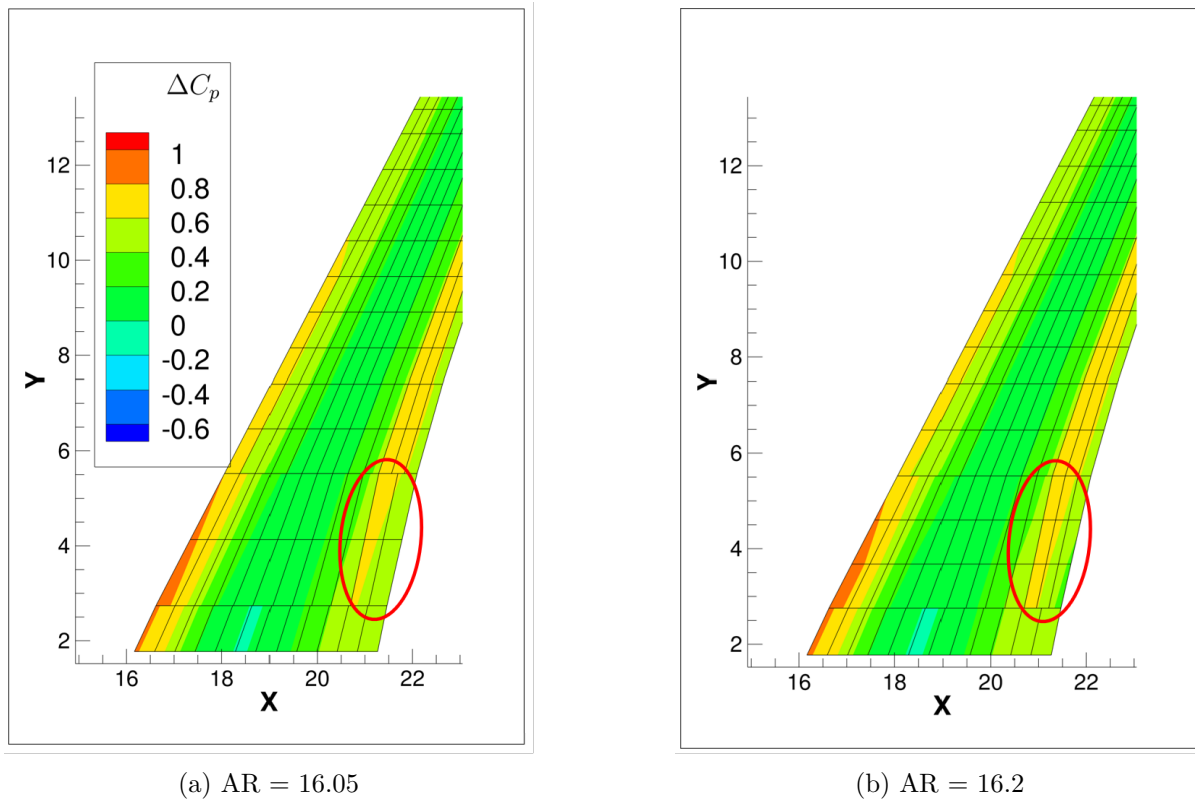
Figure 4.10: Aerodynamic grid for different aspect ratio for the surface variation method.

As already explained in Chapter 2.5.2, the stability margin is the difference between location of the aerodynamic center and the center of gravity in the x direction normalized with the mean aerodynamic chord. It has to be positive, and the larger the margin, the more stable but the less maneuverable the aircraft. The center of gravity moves backward with aspect ratio increasing for any mass case and method. It can be noticed that the aircraft's center of gravity displacement is larger than the aerodynamic center displacement for the same aspect ratio. It is then expected that the stability margin will decrease with aspect ratio. Figure 4.11 shows the evolution of the stability margin as a function of the aspect ratio for different mass cases and methods.
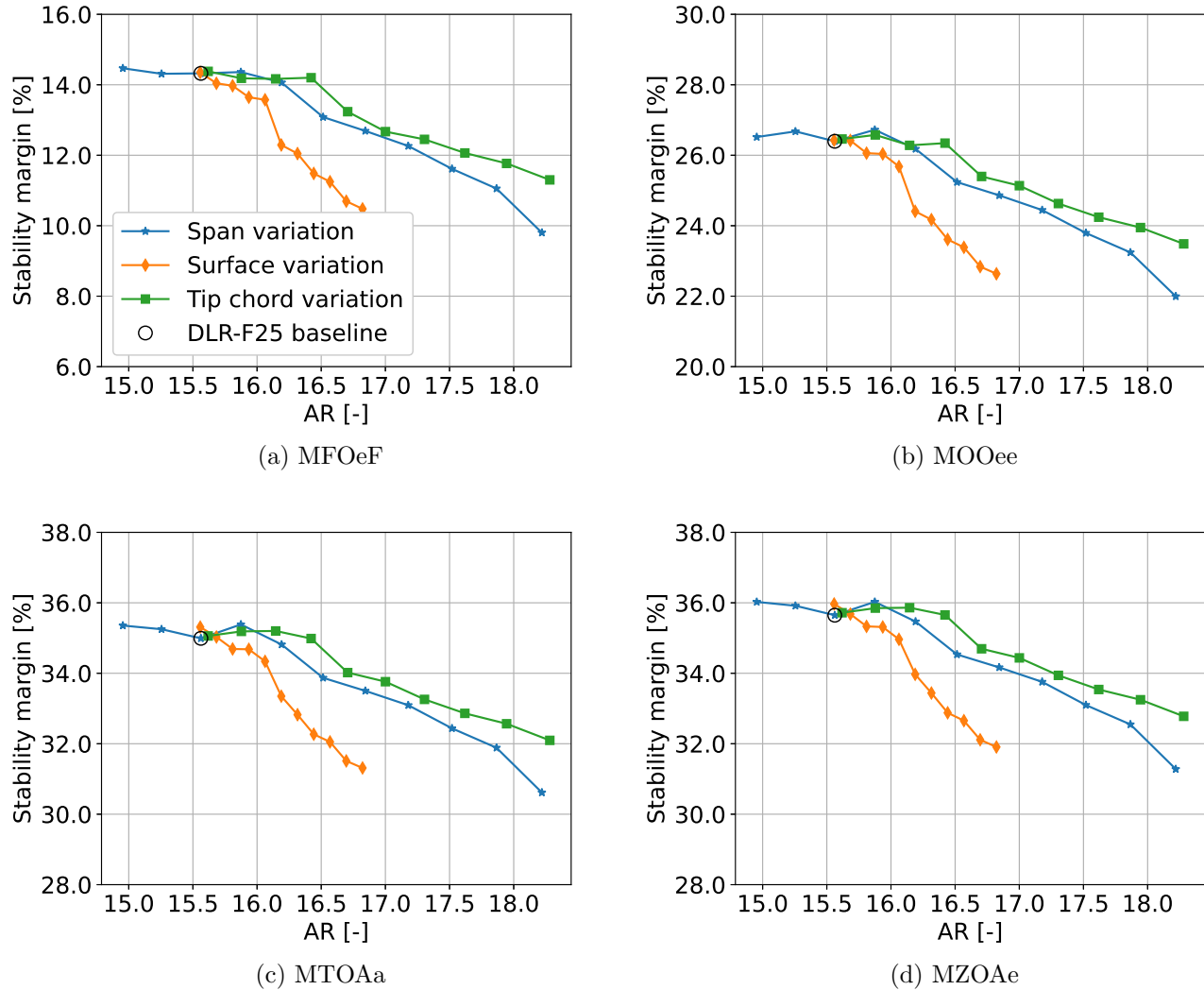
Figure 4.11: Variation of the aircraft stability margin as a function of the aspect ratio for different mass cases and methods.

As expected, the stability margin decreases for each mass case and method but never becomes negative, the aircraft is always stable. The most stable case is MZOAe and the most maneuverable case is MFOeF. Two opposite mass cases. This means that for the first case, CG and AC are very far from each other while for the last case, they are very close. However, the maneuverability of an aircraft does not only depend on its stability margin but also on the size of the control surfaces, the pitch damping, the flight control system, etc. The stability margin decreases faster for the surface variation method than for the other ones. Once again, the variation of the reference area plays an important role in the results, this is why the only case with constant surface has the smallest slope.

4.2.5 Impact on the Aerodynamic Characteristics

The lift generated by the wing is given by:

$$L = \frac{1}{2} \cdot \rho \cdot V_\infty^2 \cdot C_L \cdot S,$$

with ρ the air density, V_∞ the airspeed, C_L the wing lift coefficient and S the wing reference area. This represents the main part of the total lift that balance the aircraft mass. Because the mass only increases by less than 1% for any mass case, the main influence of the lift coefficient variation is the surface of the wing. If the surface increases, the lift coefficient has to decrease in order to keep the same force balance.

The impact of the aspect ratio on the wing lift coefficient is represented in Figure 4.12 for each mass cases and method at cruise condition. It is expected that the coefficient decreases when the wing surface increases. The lift coefficient is thus expected to be constant for the chord tip variation.

(a) MFOeF

(b) MOOee

(c) MTOAa

(d) MZOAe

Figure 4.12: Variation of wing lift coefficient as a function of the aspect ratio for different mass cases and methods.

First, it can be observed that the trend is the same for each mass case. As expected, the lift coefficient is almost constant for the tip chord variation method, decreases a little for the span variation and decreases more for the surface variation. As already explained, the lift coefficient depends on the wing surface variation. The main reason to compute the lift coefficient is to determine the induced drag coefficient by:

$$C_{D_i} = \frac{C_L^2}{e \cdot \pi \cdot AR},$$

with e the Oswald or efficiency factor and AR the aspect ratio. This induced drag coefficient will be used to compute the value of the induced drag and see the impact of the aspect ratio variation on aircraft performance. One can notice that the Oswald factor is directly computed with the lift distribution. It is obtained with a Fourier series approximation as explained in Chapter 3.6.

The main objective of this thesis is to determine if the aspect ratio increasing has a positive impact on the induced drag. The induced drag coefficient is therefore expected to decrease. Figure 4.13 represents this drag coefficient as a function of the aspect ratio for each mass case and method.
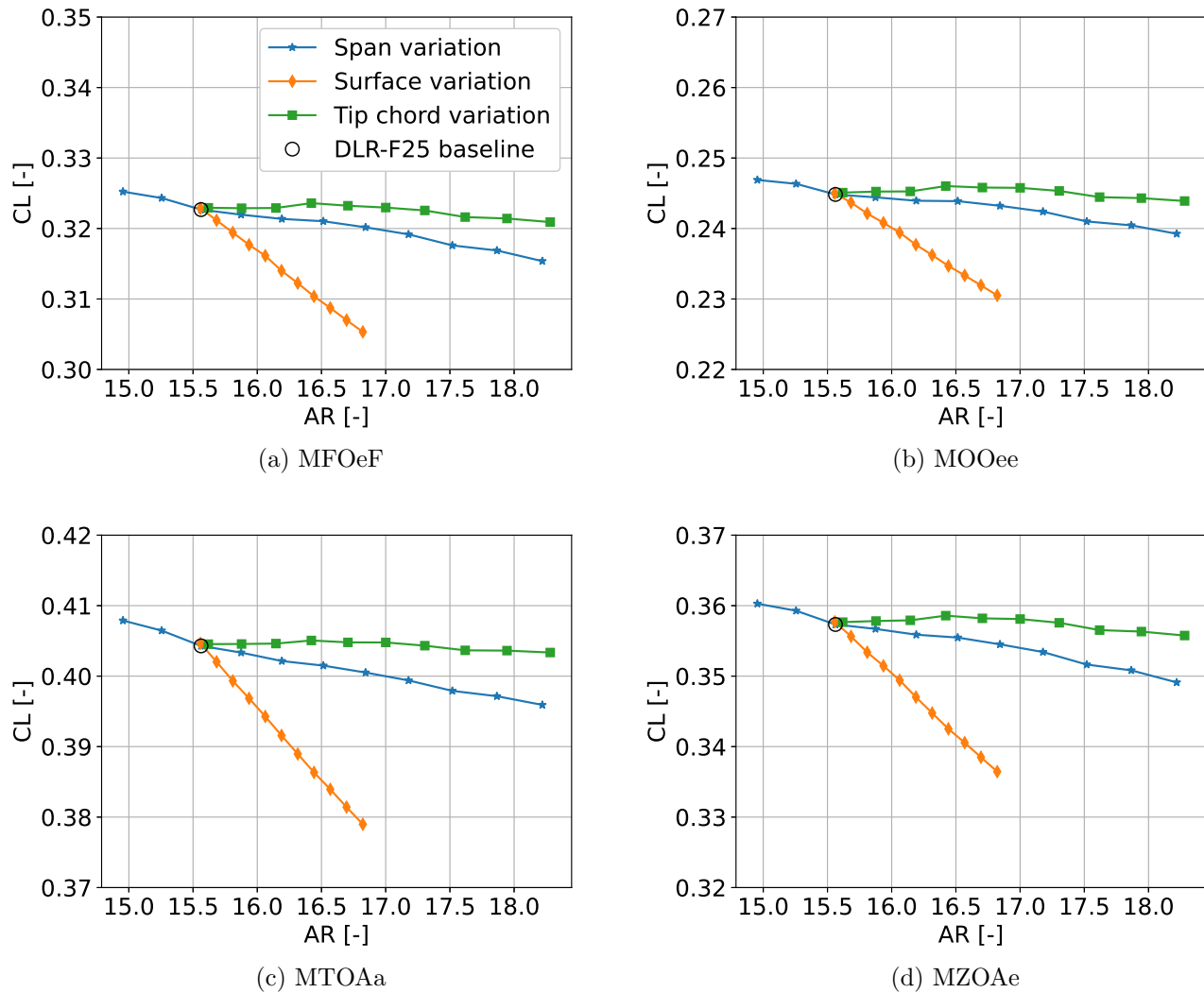

(a) MFOeF

(b) MOOee

(c) MTOAa

(d) MZOAe
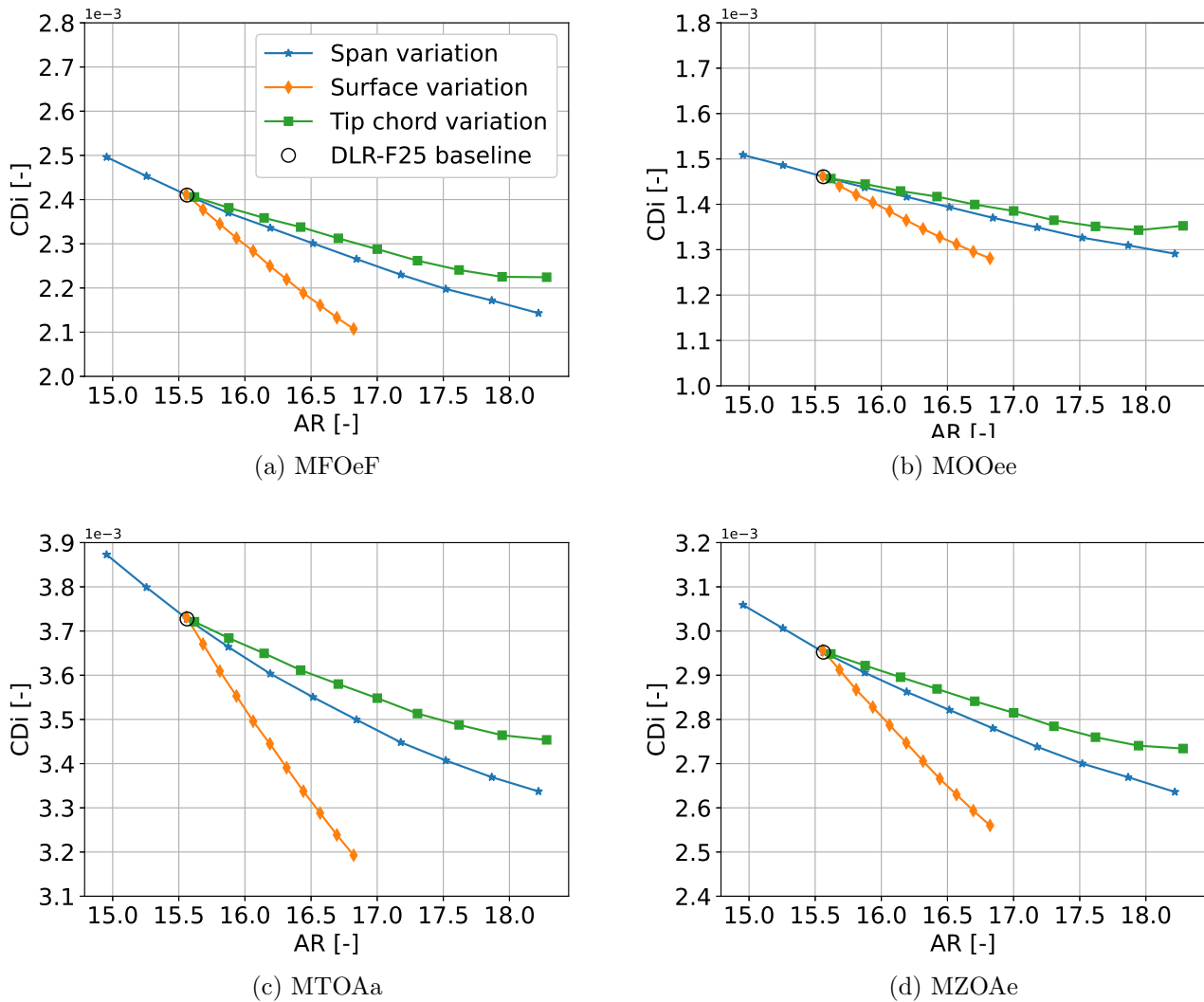
Figure 4.13: Variation of wing lift coefficient as a function of the aspect ratio for different mass cases and methods.

The trend is very similar to the lift coefficient variation. Because the induced drag is proportional to the square of the lift coefficient, the difference of results between mass cases is even larger. The induced drag coefficient of the maximum take-off case for the baseline configuration is more than 2.5 times the one of the empty mass case. Obviously, the induced drag coefficient decreases with aspect ratio for each mass case and method and decreases more for high surface variation. However, total drag is composed of profile (friction + pressure) and induced drag:

$$D = D_f + D_p + D_i = \frac{1}{2} \cdot \rho V_\infty^2 \cdot c_d \cdot S + \frac{1}{2} \cdot \rho \cdot V_\infty^2 \cdot C_{D_i} \cdot S$$

The induced drag can be quantified with the obtained induced drag coefficient results, but the profile drag will not be quantified in this study. In some cases, the induced drag can represent more than 60% of the total drag [5]. However, for the DLR-F25 configuration, this proportion is not computed and we have to be careful with this information. The induced drag as a function of the aspect ratio is shown in Figure 4.14 for each mass case and method.

(a) MFOeF

(b) MOOee

(c) MTOAa

(d) MZOAe
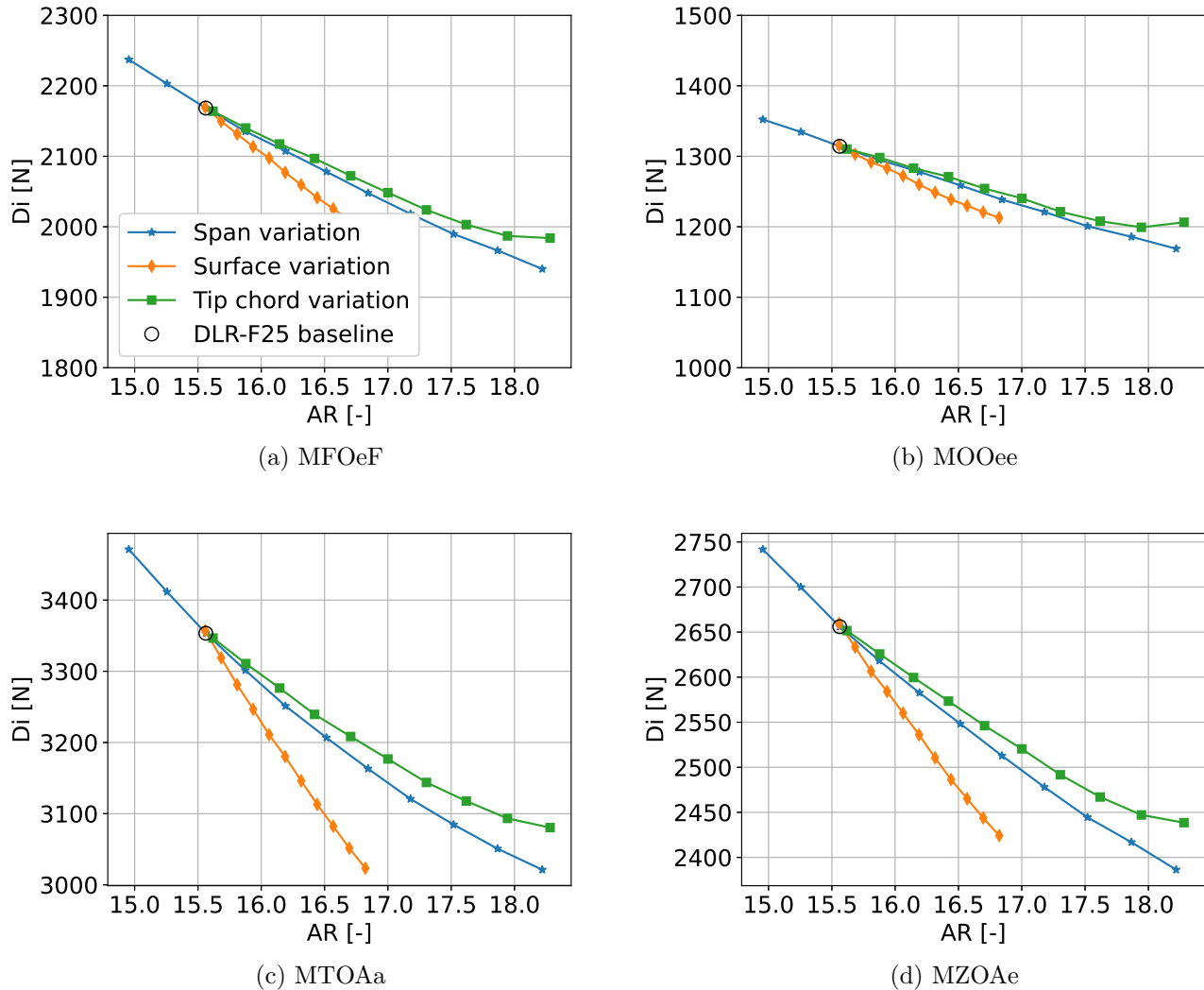
Figure 4.14: Induced drag as a function of the aspect ratio for different mass cases and methods.

It can be seen that there is a real positive impact on the induced drag. The drag reduction is larger in term of absolute value for heavier cases. The negative slope is larger for surface variation method. However, as said before, the profile drag will also increase. This has to be taken into account. The only case where the profile drag will almost not increase is the tip chord variation method. The gain in induced drag can be considered as a gain in total drag. Table 4.1 shows the relative gain in induced drag for aspect ratio variation from 15.6 until 16.8. It corresponds to the total variation of aspect ratio for the surface variation method and allows to have comparable results. The reduction of induced drag is obviously higher for surface variation method because the lift coefficient is also lower compared to the

other methods. However, the profile drag will also increase, more than for the other methods. At the moment, is is not possible to know which method is the best without knowing the contribution of the profile drag. However, the induced drag is quite significant.

Method	MFOeF	MOOee	MTOAa	MZOAe	Surface [m^2]	Surface variation [%]
Span variation	-5.8	-5.5	-5.7	-5.4	131.2	0.85
Surface variation	-8.5	-7.5	-9.9	-8.7	136.8	5.0
Tip chord variation	5.4	-5.1	-4.9	-4.7	130.1	0.0

Table 4.1: Variation of induced drag (in %) between aspect ratio of 15.6 and 16.8 (+7.7%) for each mass case and method and variation of reference area.

Even if it is not possible to exactly know the impact of the aspect ratio variation on the aircraft fuel consumption, some approximation can be done in order to estimate the impact on the Breguet range expressed as follows:

$$R = \frac{V}{SFC} \frac{L}{D} \ln\left(\frac{W_i}{W_f}\right),$$

with V the true airspeed, SFC the specific fuel consumption, L and D the lift and drag of the aircraft, Wi and Wf the initial and final weights of the aircraft. By assuming the mass does not change with AR (or not enough to have a real impact on the equation), the lift, velocity and specific fuel consumption also stay constant, the drag is the only parameter that changes. Assuming that the induced drag initially represents 50% of the total drag, the impact of the aspect ratio can be estimate. The total drag for new wing configuration can be expressed as follows:

$$D^f = D_p^f + D_i^f \qquad \text{with} \quad \begin{cases} D_p^f = D_p^i \cdot \left(\frac{S^f}{S^i}\right) \\ D_i^f = D_i^i \cdot (1 + \Delta D_i), \end{cases}$$

with the exponent f and i meaning the new wing configuration (after AR variation) and baseline wing configuration, D_p and D_i the pressure and induced drag, ΔD_i the variation of the induced drag, S^i and S^f the wing surface for the baseline configuration and for the new configuration, respectively. The assumption that only the surface variation impacts the pressure pressure drag variation has been made. The total drag for the new wing configuration can then be rewritten as follows:

$$D^f = 0.5 \cdot \left(\frac{S^f}{S^i} \cdot + (1 + \Delta D_i)\right) \cdot D^i$$

The variation of the Breguet range can be expressed by:

$$\Delta R = \frac{1}{0.5 \cdot \left(\frac{S^f}{S^i} \cdot + (1 + \Delta D_i)\right)} - 1$$

Table 4.2 shows the maximum variation of the Breguet range for each mass case and each aspect ratio variation method between aspect ratio of 15.6 to 16.8.

Method	MFOeF	MOOee	MTOAa	MZOAe
Span variation	+2.5	+2.4	+2.5	+2.3
Surface variation	+1.7	+1.2	+2.4	+1.8
Tip chord variation	+2.8	+2.6	+2.5	+2.4

Table 4.2: Variation of the Breguet range (in %) between aspect ratio of 15.6 and 16.8 (+7.7%) for each mass case and method and variation of reference area.

It can be observed that the methods that increase the more the Breguet range are the tip chord variation and the span variation. This increase is about 2.5%, that is not negligible. However, the method used to compute this range variation is an approximation based on some assumptions and need the exact profile drag to have a more precise result.

4.2.6   Impact on the Gust Loads

The maximum vertical force as well as the maximum bending moment due to gust as a function of the aspect ratio are shown in Figure 4.15 and 4.16, respectively.
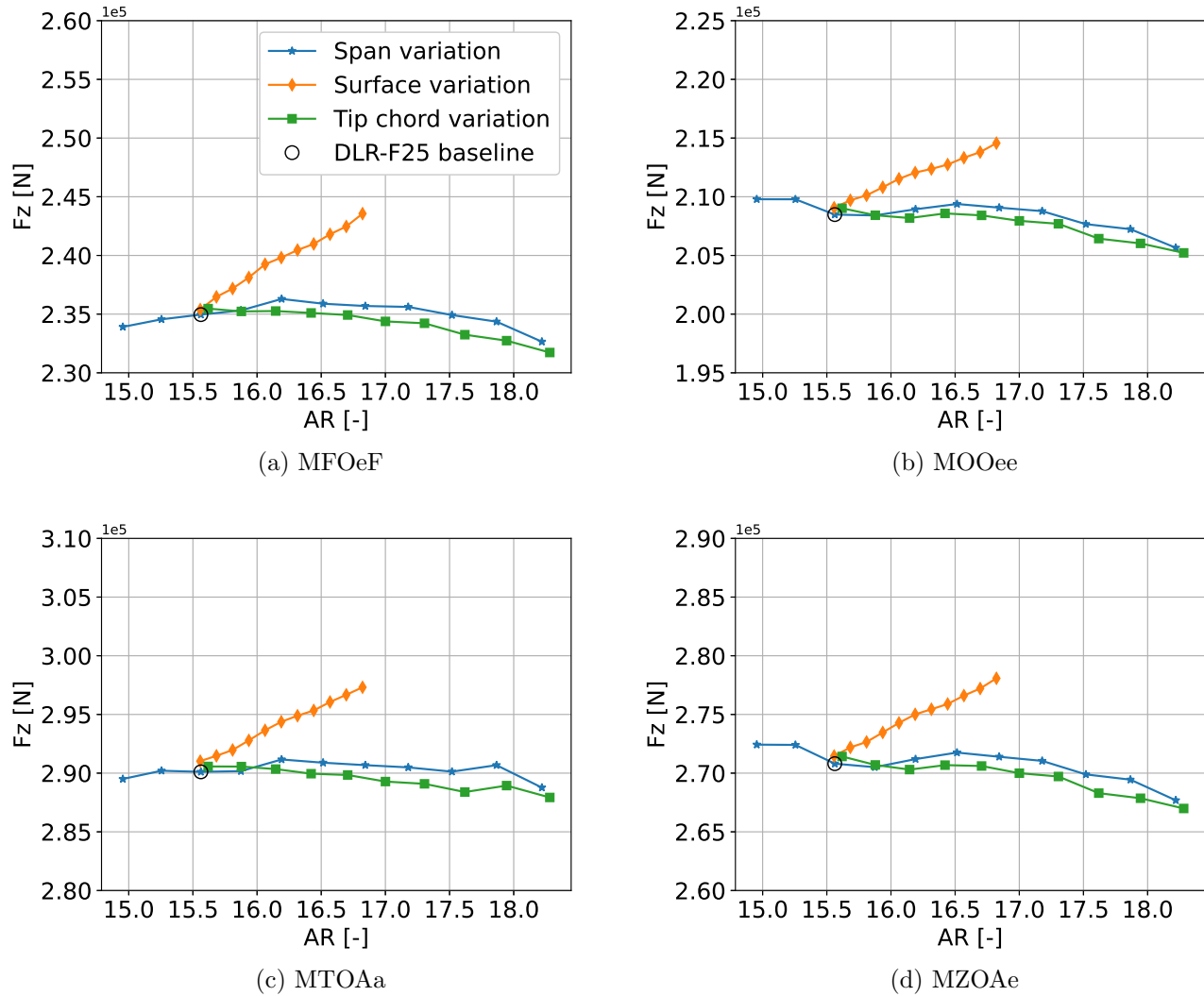

Figure 4.15: Maximum vertical force due to gust as a function of the aspect ratio for different mass cases and methods.
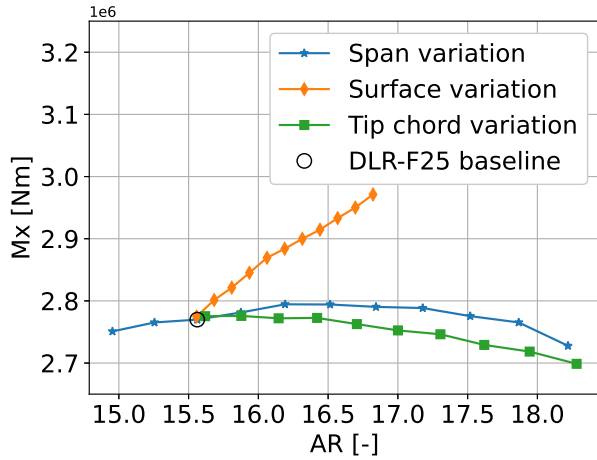
(a) MFOeF
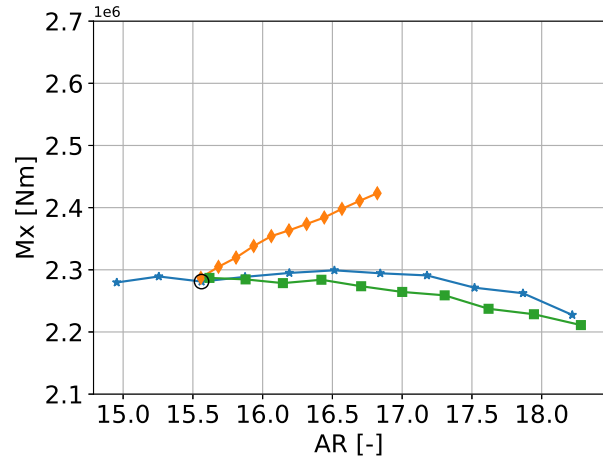
(b) MOOee
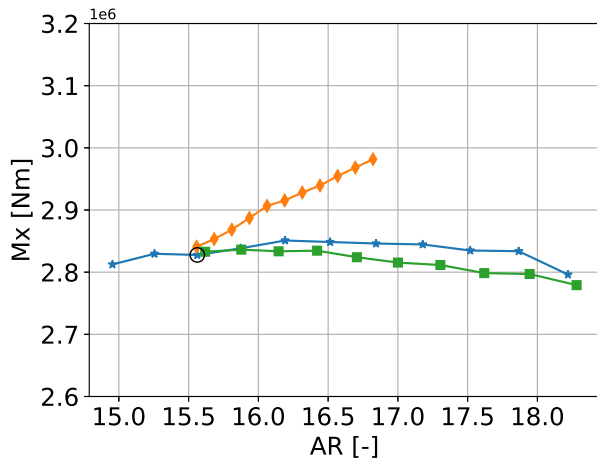
(c) MTOAa
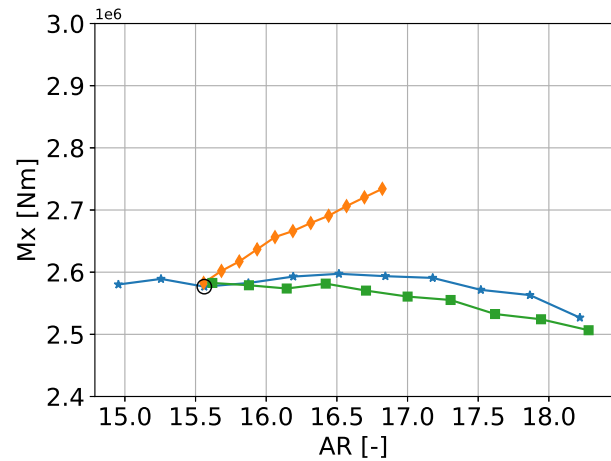
(d) MZOAe

Figure 4.16: Maximum bending moment due to gust as a function of the aspect ratio for different mass cases and methods.

As in Chapter 2.5.5 the results are obtained for the monitoring point CW640005, close to the wing root. For both Figures 4.15 and 4.16, the trend is exactly the same. It can also be noticed that the force and moment are larger for maximum take-off weight case and lighter for empty case. Regarding the curves, once again, the trend is similar to the mass variation.

4.2.7 Impact on the Flutter Speed

It is very important to check if the flutter speed is always out of the flight envelope. All the flutter speed in the flight envelope, which means lower than the dive speed are represented in Figure 4.17.
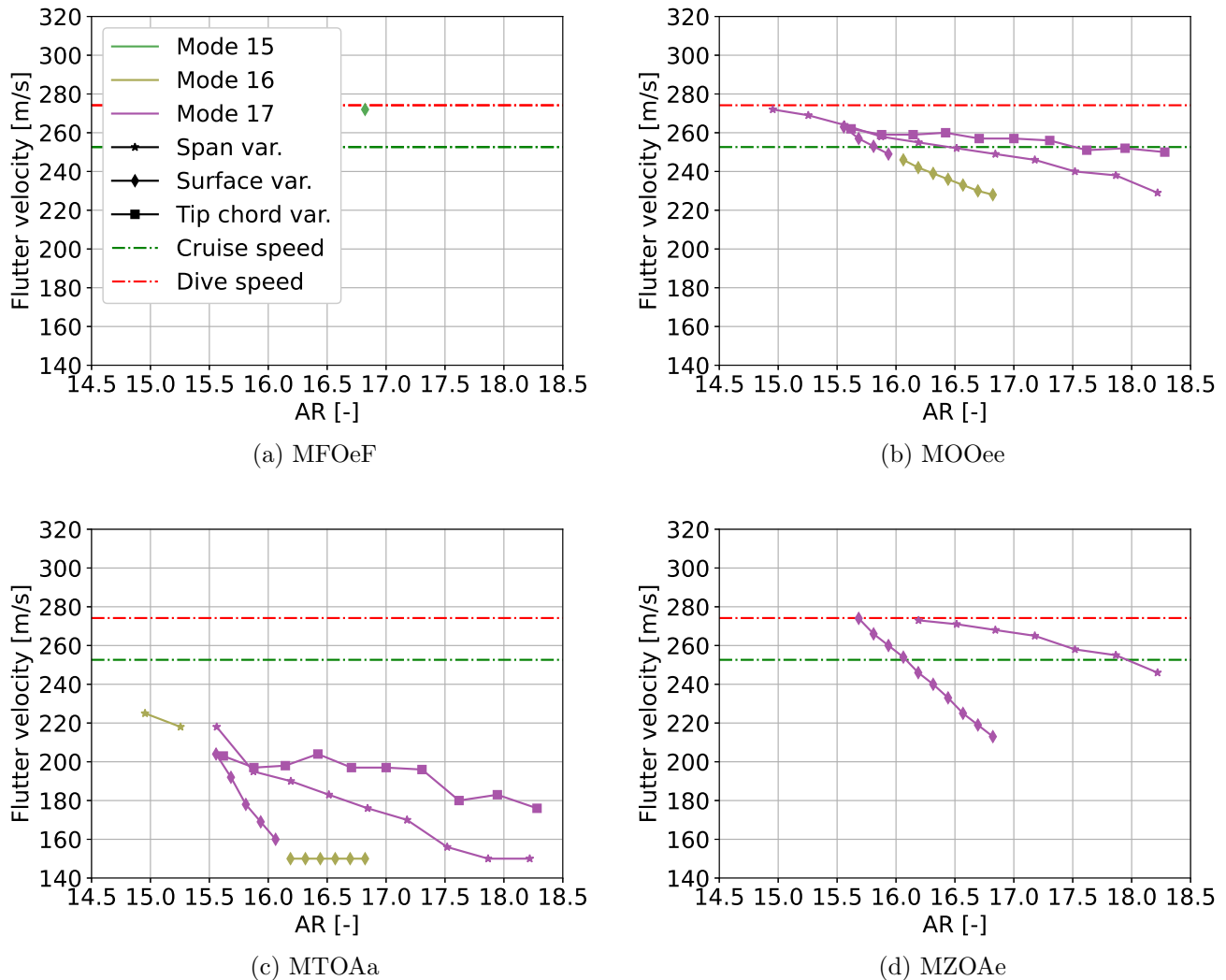
Figure 4.17: Flutter velocity as a function of the aspect ratio for different mass cases and methods.

It can be noticed that there are a lot of cases where the flutter happens in the flight envelope. However, as explained in Chapter 2.5.6, if there are in-plane modes, this is not an issue anymore. Indeed, MSC Nastran does not compute drag and for in-plane modes, the main part of the damping comes from the drag. If the drag has been calculated by MSC Nastran, there will be no problem with the flutter.

For the MFOeF case, only mode 15 for the surface variation has a flutter velocity below the dive speed. It can be seen in Figure 4.18b that this is an in-plane mode.

Regarding the MOOee case, 3 curves can be identified, one for each method. All curves decrease which mean the flutter appears sooner by increasing the aspect ratio. Mode 17 is checked and is also an in-plane mode. Another thing that can be noticed is that for the surface variation method, the purple and yellow curves seem to be continuous but with different modes. It looks like this is the same mode shape but not

the same number. It is probably due to the fact that by increasing aspect ratio, a new mode shape with lower frequency than mode 16 appears, this mode becomes mode 17. It can be verified in Figure 4.18a that modes shapes at the transition zone are both in-plane modes.
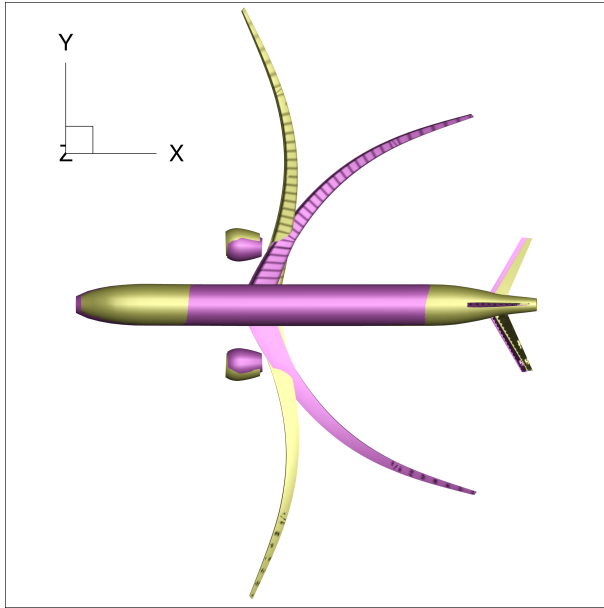
(a) Mode shapes 16 (yellow) and 17 (purple) of MOOee case, surface variation method and aspect ratio of 16.05 (yellow) and 15.95 (purple).
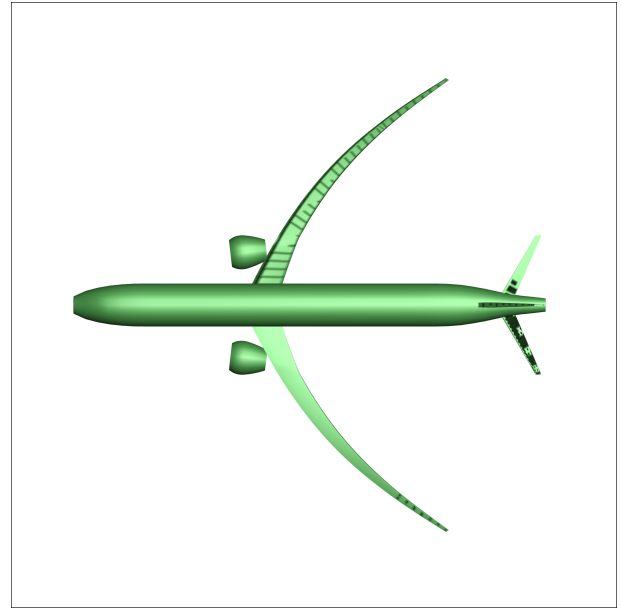
(b) Mode shapes 15 of MFOeF case, surface variation method and aspect ratio of 16.8.

Figure 4.18: Mode shapes of the flutter cases for MFOeF and MOOee cases.

The same observation can be done for the maximum take-off weight. There are also 2 transition zones: one for the surface variation and another for the span variation method. Once again, mode shapes are respectively represented in Figure 4.19a and 4.19b for the surface and span variation methods. These modes are in-planes modes which means that there are no flutter issues.

Every result for every mass case and method has been checked regarding flutter speed and it has been shown that by increasing the aspect ratio, flutter is still out of the flight envelope and will not appear during flight.
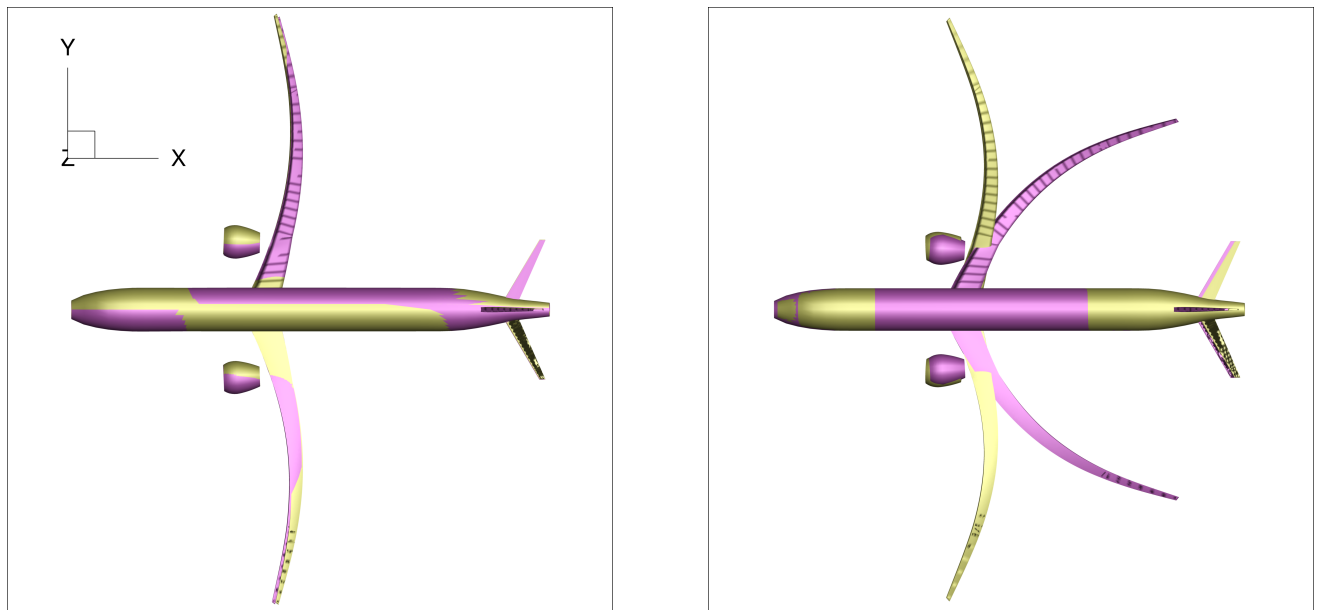
(a) Surface variation method, aspect ratio of 16.2 (yellow) and 16.05 (purple)

(b) Span variation method, aspect ratio of 15.25 (yellow) and 15.55 (purple)

Figure 4.19: Mode shapes 16 (yellow) and 17 (purple) of MTOAa case.

4.3 Discussion of the Results

In this chapter, the limitations of the aspect ratio variation methods have been explained. The baseline aspect ratio being already very large, it is quite difficult to increase it without compromising the structure. Moreover, the tip chord is very small and will be smaller by increasing the aspect ratio, which will probably cause some manufacturing issues. It will also cause a weak stiffness. One possible solution would be a wingbox monocoque at the tip which could increase the stiffness.

Different gust loads have been used for the cpacs-Mona simulation process: no gust, Pratt gust and Nastran SOL 146. The simulations without gust load computation give results very close to the ones obtained with Nastran SOL 146. The simulations with Pratt gust give very different results, especially for the mass variation with respect to the aspect ratio. Pratt gust is a low fidelity method using a quasi-steady approach while Nastran SOL 146 is a high fidelity method using 1-cos gusts. This solution is based on dynamic aeroelasticity and calculate the RMS responses of the PSD function. This last gust loads method is preferred. Moreover, the Pratt gust simulations have more difficulties to reach the convergence of the optimiser. For aspect ratios beyond 16.8, the simulations using Pratt gust do not converge anymore.

The impact of the aspect ratio on the structural, aerodynamic and aeroelastic characteristics has been analysed. There are some trends in the results. Certain parameters, such as the aircraft's center of gravity and the aerodynamic coefficients, have an expected trend while others, such as the aircraft's aerodynamic center and the total mass of the aircraft, have a surprising trend.

It is expected that for a swept wing aircraft whose the span increases to have its center of gravity that moves backward and even more if the reference area also increases. This expectation is well confirmed. Because the increase of the wing mass does not influence that much the aircraft's total mass, the lift coefficient is expected to be constant if the reference area is constant and to decrease if the reference area increase. Indeed, the lift that the wing needs to generate is almost the same so the lift coefficient can

be considered directly proportional to the wing surface. This trend is also verified. The induced drag also decreases with the aspect ratio increase which is the main objective of the aspect ratio variation investigation. The bending and torsional deformation are also expected to increase (in term of absolute value for the negative torsional deformation). Both behaviours are also observed in the results.

Other parameters do not follow the expected trend and need to be deeply analysed. The mass for example, is expected to increase, however for the span variation and tip chord variation methods, this is not the case. The mass increases until an aspect ratio of 16.5 and beyond this aspect ratio, the mass decreases. For very high aspect ratio and very narrow tip chord, load alleviation is used by the optimiser to reduce the bending deformation by creating negative lift near the tip. This bending reduction allows the reduction of the material used and then, the mass also decreases. For the surface variation method, the behaviour is the one expected because the surface increase automatically increases the mass. Moreover, a smaller aspect ratio is reached and the tip chord does not decrease which avoid some physical issues.

Conclusion and Future Work

Summary and Conclusion

Through this section, the main discussions and results obtained in each chapter of this thesis are summarised.

In the first chapter, cpacs-MONA, the structural optimisation tool developed by the German Aerospace Center (DLR), have been described and its capabilities has been discussed. This optimisation tool uses a very complete process to generate finite element structural and aerodynamic models of an aircraft with ModGen. These models are used by MSC Nastran with the aims of finding the structural, aerodynamic and aeroelastic characteristics of the aircraft. Each solution used by MSC Nastran for this work has been described (SOL 144 for the maneuver loads, SOL 145 for the flutter analysis and SOL 146 for the gust loads) and the structural optimisation loop has been defined.

In the second chapter, one of the aircraft concept designed by DLR, the DLR-F25 has been described in terms of its mission requirement, wing planform, geometry and engine capabilities. The DLR-F25 is a high aspect ratio mid-range jet transport aircraft similar to the Airbus A32O in term of range, mass cases and flight conditions with the difference of aspect ratio. The mass and load cases as well as the design speeds have been defined and used for the simulation process with cpacs-MONA. The aerodynamic characteristics, such as the lift distribution, and the structural characteristics, such as the bending and torsional distribution along the span, have been computed by using Nastran SOL 144. The load envelope of the DLR-F25 has been computed with all loads applied on the aircraft, such as the maneuver and gust loads. The flutter has also been checked for each mode, however, in-plane modes are subject to flutter in the flight envelope. MSC Nastran is not able to damp this kind of mode because it does not compute drag which is the main source of damping for in-plane modes. In reality, there is drag to damp this mode so this flutter mode was not consider as an issue anymore.

The third chapter was dedicated to the modifications made to the whole simulation process. From the modification of the wing geometry to the post processing. Three methods of wing geometry modification have been developed: one based on the span extension by keeping the leading and trailing edges, another based on the wing surface variation, from 0 to 5%, by only keeping the leading edge line as well as the tip chord length constant, and the last based on the tip chord variation, from 60 to 15 cm, by keeping the same wing surface and leading edge line. Only the outer part of the wing (after the kink) is modified. The ribs and spars definitions as well as the aerodynamic grid have been modified in order to avoid structural and aerodynamic discontinuities. A post processing routine including the extraction of the quantities of interest and a method to verify the reliability of aircraft characteristics has been implemented. The results were obtained with a script with the aims of automatically modifying the wing geometry, running the cpacs-MONA process and doing the post processing routine. Finally, a method based on a Fourier series has been used to compute the Oswald factor, useful for the computation of the induced drag coefficient.

In the last chapter, the limits of the aspect ratio variation are shown. The simulation process can handle aspect ratios until 18.3 while physics and manufacturing have probably more difficulties to deal with such a higher aspect ratio for a mid-range jet transport aircraft such as the DLR-F25. Two different gust loads calculation methods are compared: Prat gust, based on a quasi-steady approach and Nastran Solution 146, based on discrete 1-cos gusts. The Nastran SOL 146 gives better results than Pratt gusts so this first method is preferred for the rest of the analyses. It has been determined that the aircraft's center of gravity and aerodynamic center move backward with the aspect ratio and because the CG moves faster, the distance between AC and CG decrease. This means that the stability margin also decreases with the aspect ratio. As expected, the wing bending and torsional deformation also increase. The mass is expected to increase, however for the span variation and tip chord variation methods, this is not the case. The mass increases until an aspect ratio of 16.5 and then, beyond this aspect ratio, decreases. For aspect ratios beyond 16.5, the optimiser creates a large amount of negative lift near the tip which reduces the bending moment, the wing skin thickness and therefore, the mass of the wing. This is an optimal wing but not really reliable. The main objective of the thesis is the induced drag reduction through an aspect ratio increase. This has been shown that with an aspect ratio from 15.6 to 16.8, the induced drag is reduced from 5 to 10% depending on the method. However, because the profile drag is not computed in this study, and some methods have an increase in wing surface, it is not possible to know which is the best method. More investigations need to be realised in the future.

Ideas for Future Work

cpacs-MONA is a very complete computational framework that can design highly parameterised aeroelastic aircraft structures and evaluate the aerodynamic, aeroelastic and structural behaviour of these structures. It is already well improved, however, it still needs some modifications in order to be more usable. One aspect of cpacs-Mona that probably needs to be modified is the aerodynamic grid generation. It is not convenient for the user to change this grid because there is no option in the CPACS dataset to choose the mesh distribution along the span and the chord. The only parameter that can be modified is the number of panels on the chordwise direction, but not the distribution. Another aspect of cpacs-MONA that could be implemented in the future is a definition of a monocoque wingbox at the tip. This could increase the stiffness and decrease the bending moment. By this, the aspect ratio can even be higher.

Bibliography

[1] Statista Research Department. *Global Air Traffic - Number of Flights 2004-2023*. URL: `https://www.statista.com/statistics/564769/airline-industry-number-of-flights/` (visited on 01/05/2024).

[2] Statista Research Department. *Commercial Airlines Worldwide - Fuel Consumption 2005-2023*. URL: `https://www.statista.com/statistics/655057/fuel-consumption-of-airlines-worldwide/` (visited on 01/05/2024).

[3] V. Padilla. *Le Paradoxe de Jevons en Aviation*. URL: `https://aertecsolutions.com/fr/2014/09/15/le-paradoxe-de-jevons-en-aviation/` (visited on 01/05/2024).

[4] J. Anderson. "WINGS: From the Wright Brothers to the Present". In: *National Air and Space museum* (Dec. 2011). URL: `https://airandspace.si.edu/stories/editorial/wings-wright-brothers-present`.

[5] T. Andrianne and V.E. Terrapon. *Lecture : Aerodynamics*. University of Liège, 2021-2022.

[6] A. Benaouali and S. Kachel. "Multidisciplinary Design Optimization of Aircraft Wing Using Commercial Software Integration". In: *Aerospace Science and Technology* 92 (Sept. 2019), pp. 766–776.

[7] D. Raymer. *Aircraft design : a conceptual approach*. 6th ed. American Institute Of Aeronautics and Astronautics, Inc, Sept. 2018.

[8] D. E. Calderon et al. "Sizing High-Aspect-Ratio Wings with a Geometrically Nonlinear Beam Model". In: *Journal of Aircraft* 54.4 (July 2019).

[9] G. Dimitriadis and T. Andrianne. *Lecture : Aeroelasticity and Experimental Aerodynamics*. University of Liège, 2022-2023.

[10] T. Klimmek et al. "cpacs-MONA - an Independent and in High-fidelity Based MDO Tasks Integrated Process for the Structural and Aeroelastic Design of Aircraft Configurations". In: International Forum of Aeroelasticity and Structural Dynamics. Savannah, Georgia, USA, June 2019.

[11] German Aerospace Center (DLR) - Institute of System Architectures in Aeronautics. *cpacs, A Common Language for Aircraft Design*. URL: `https://dlr-sl.github.io/cpacs-website/` (visited on 01/04/2024).

[12] M. Schulze. *cpacs-MONA - User's Manual*. German Aerospace Center (DLR) - Institute of Aeroelasticity, 2023.

[13] MSC Nastran. *Aeroelastic Analysis User's Guide*. June 2018.

[14] M. Patil, R. Yurkovich, and D. Hodges. "Incorrectness of the k method forFlutter Calculations". In: *Journal of Aircraft* 41 (Mar. 2004), pp. 402–405.

[15] T. Klimmek. *Parameterization of Topology and Geometry for the Multidisciplinary Optimization of Wing Structures*. Jan. 2009.

[16] Horizon Europe. *Ultra Performance Wing*. URL: `https://cordis.europa.eu/project/id/101101974` (visited on 01/07/2024).

[17]   T. Klimmek G. P. Chiozzotto S. Cumnuantip. *Kriterien für die Erstellung eines Lastenkatalogs.* DLR Institute of Aeroelasticity, Feb. 2014.

[18]   G. P. Chiozzotto. *LCspeed v1.0.0 - Structural Design Speed Calculation.* German Aerospace Center (DLR) - Institute of Aeroelasticity, Mar. 2014.

[19]   European Union Aviation Safety Agency (EASA). *Certification Specifications (CSs).* URL: `https://www.easa.europa.eu/en/document-library/certification-specifications` (visited on 01/04/2024).

[20]   E. Torenbeek and H. Wittenberg. *Flight Physics - Essentials of Aeronautical Disciplines and Technology, with Historical Notes.* 1st ed. Springer Dordrecht, July 2009.

[21]   G. Dimitriadis. *Lecture : Flight Dynamics and Control.* University of Liège, 2021-2022.

[22]   M. Siggel et al. *TiXI XML-library.* Version 3.3.0. Mar. 2022. URL: `https://github.com/DLR-SC/tixi`.

[23]   Muhammad Amir Mirza Bin Mohd Zakuan, Adul Aabid, and Sher Afghan Khan. "Modelling and Structural Analysis of Three-Dimensional Wing". In: *International Journal of Engineering and Advanced Technology* 9 (Oct. 2019).

[24]   M. Niţă and D. Scholz. "Estimating the Oswald Factor from Basic Aircraft Geometrical Parameters". In: *Hamburg University of Appled Sciences* (2012).

[25]   J. D. Anderson Jr. *Fundamentals of Aerodynamics.* 6th ed. McGraw-Hill Education, 2017.

[26]   A. P. Ricciardi et al. "Evaluation of Quasi-Static Gust Loads Certification Methods for High-Altitude Long-Endurance Aircraft". In: *Journal of Aircrafts* 50 (Mar. 2013), pp. 457–468.

[27]   Z. Wu, Y. Cao, and M.Ismail. "Gust loads on aircraft". In: *The Aeronautical Journal* 123 (June 2019), pp. 1216–1274.

[28]   M. Drela. *Flight Vehicles Aerodynamics.* Massachusetts Institute of Technology, 2014.

[29]   C. Unger. "Bending Instead of Snapping". In: *DLR Magazine* (Dec. 2020), pp. 38–41.